Title	Study of 4ΣHe production via 4He(K-, π-)X reaction at pK- = 1.5 GeV/c
Author(s)	中川, 真菜美
Citation	大阪大学, 2020, 博士論文
Version Type	VoR
URL	https://doi.org/10.18910/77464
rights	
Note	

Ph.D Thesis

Study of $_\Sigma^4$He production via ^{4}He(K^-, π^-)X reaction at $p_{K^-} = 1.5$ GeV/c

Manami Nakagawa

Department of Physics, Osaka University

Abstract

To investigate the ΣN interaction, it is necessary to examine Σ hypernuclei. $^{4}_{\Sigma}$He is the only Σ hypernucleus ever discovered. Only the ground state of $^{4}_{\Sigma}$He has been observed using beam momenta of 0 and 0.6 GeV/c. The current theoretical calculations cannot reproduce the measured missing-mass spectra unless the Σ-nucleus potential for the excited state is scaled by a normalization factor. However, the potential for the excited state is uncertain since no excited state has been observed. Therefore, the excited state of $^{4}_{\Sigma}$He should be searched for to investigate the Σ-nucleus interaction in more detail.

The missing-mass spectrum for the ^{4}He$(K^-, \pi^-)X$ reaction at $p_{K^-} = 1.5$ GeV/c was measured in the J-PARC E13 experiment. The measured spectrum was analyzed by taking into account the ground and excited states in $^{4}_{\Sigma}$He and the Λ and Σ quasi-free production processes. It was found that the measured binding energy and the width of the ground state were consistent with both of the past experimental resluts and the theoretical prediction. To estimate the significance of the existence of the excited state, the null and alternative hypotheses were tested. As the results, the reduced χ^2 value of the alternative hypothesis was 1.08, whereas the probability of null hypothesis was 2×10^{-9}. Thus, the exsistence of the excited state was strongly suggested.

The measured binding energy of the excited state was within the expected range when the real part of the Σ-nucleus potential was scaled by a factor of $N_R = 0.6$–1.0. The measured cross section for the excited state was smaller than that of the ground state although the theoretical cross section for the excited state was larger than that for the ground state. This fact suggests that the imaginary part of the Σ-nucleus potential for the excited state might be much larger than that for the ground state.

The measured missing-mass spectrum for the ^{4}He$(K^-, \pi^-)X$ reaction was divided into the six angular ranges, and the angular distributions of the differential cross sections for the ground and excited states were obtained for the first time. There is almost no difference in the slopes of the angular distributions between the ground and excited states. It is therefore difficult to distinguish their spins from slopes. The slopes of the measured angular distributions are steeper than the theoretical prediction. It implies that the size of the hypernucleus is possibly larger than expected.

The theoretical calculation does not satisfactorily describe the angular distributions of the cross sections for the ground and excited states and their relative strength. The present result should provide an important insight into the Σ-nucleus interaction, and further theoretical studies are strongly desired to clarify the Σ-nucleus interaction.

i

Contents

Chapter 1

Introduction

1.1 Nuclei and hypernuclei

Matter in our surroundings is composed of atoms. Each atom is composed of a nucleus and electrons. It is theoretically expected that about ten thousand nuclei exist [1]. Among them, about three thousands have been observed experimentally [2]. Each nucleus is composed of protons and neutrons which are called nucleons. Nucleons are bound by the nuclear force in a nucleus. The nuclear force has been systematically studied by investigating nuclear structures and nucleon-nucleon scatterings [3, 4, 5, 6].

The nucleon is a member of the baryon family which is composed of three constituent quarks. Each quark has one of six flavors: up, down, charm, strange, top, and bottom. The two lightest quarks are up and down quarks. The nucleon, the lightest baryon, consists of the up and down quarks only. The next lightest quark is the strange quark. The baryon configuration with the up, down, and strange quarks is expressed by the flavor SU(3) symmetry. The nucleon belongs to the baryon octet in the flavor SU(3) symmetry with spin of 1/2 (see Fig. 1.1). Several hyperons also belong to the same baryon octet having at least one strange quark and a non-zero strangeness quantum number $S = -1$ or -2. The lightest hyperon is the Λ hyperon, and the second lightest is the Σ hyperon. The Σ hyperon has isospin $I = 1$ while the Λ hyperon has a zero isospin ($I = 0$).
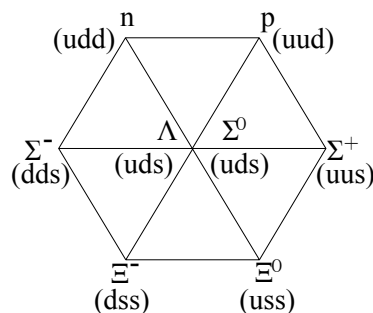

Figure 1.1: Baryon octet in the flavor SU(3) symmetry with spin of 1/2.

As for the understanding of the hyperon-nucleon interaction, in principle, the hyperon-nucleon scattering data provides information. However, it is difficult to measure the scattering cross sections because hyperon has a short lifetime ($c\tau$ is roughly a few cm [7]). Therefore, the hyperon-nucleon interaction has been mainly studied in the nuclear medium *i.e.*, hyper nuclei composed of nucleons and hyperons. Regardless of the short lifetimes of the hyperons, hypernuclear structures can be understood by investigating production reactions and decay processes. A Λ hypernucleus has a Λ hyperon in a nucleus. In case of the Σ hyperon, it is called the Σ hypernucleus. So far, about forty species of Λ hypernuclei have been observed and studied by spectroscopy and emulsion experiments [8]. The Λ-nucleus interaction has been examined by measuring the Λ hypernuclear structures and is known to be attractive. As for the Σ-nucleus interaction, it has not been examine well because the Σ hypernucleus was scarecely ever observed.

The total isospin T of the ΛN system is $T = 1/2$ only and the ΛN interaction is attractive. T of the ΣN system is either $T = 3/2$ or $T = 1/2$. The ΣN interaction in the $T = 1/2$ channel is suggested to be attractive. On the other hand, several experiments and theoretical works have indicated that the ΣN interaction in the $T = 3/2$ channel, such as the $\Sigma^+ p$ and $\Sigma^- n$ pairs, is strongly repulsive [9, 10, 11]. The Σ-nucleus potential has been obtained by folding the ΣN interaction.

In Σ hypernuclei with isospin satureted cores, the isospin dependence of the ΣN interaction is averaged out and becomes small. For heavy nuclei, the isospin independent component becomes dominant. Experiments and theories indicated that the isospin independent component of the Σ-nucleus interaction is repulsive. This seems to be the reason that most of Σ hypernuclei are unbound. Only light Σ hypernuclei might be possible to be bound due to the isospin dependent component of the ΣN interaction.

In addition, natural widths of Σ hypernuclei are also different from those of Λ hypernuclei. In free space, both of Λ and $\Sigma^\pm$ decay into the $\Lambda(\Sigma^\pm) \to N\pi$ channel by the weak interaction. However, in the nuclear medium, the decay mode of Σ is different from that of Λ. The Λ hyperon in the nuclear medium decay into the $\Lambda \to N\pi$ (or $\Lambda N \to NN$) channel by the weak interaction as in the free space. On the other hand, the ΣN pair with $T = 1/2$ can convert into the ΛN pair in the nuclear medium through the strong interaction. Even if bound states in Σ hypernuclei exist, a natural width of a state of Σ hypernuclei is too broad to be observed due to the fast $\Sigma N \to \Lambda N$ conversion process.

1.2 Experimental studies on ΣN interaction

1.2.1 ΣN scattering

A direct way to study the ΣN interaction is to measure the Σ-nucleon scattering. In 1965, the $\Sigma^\pm p$ scattering was measured using the hydrogen bubble chamber at CERN [12]. A K^- beam was injected to the hydrogen bubble chamber to produce $\Sigma^\pm$ beams at the momentum range of 135–175 MeV/c via the $K^- p \to \Sigma^\pm \pi^\mp$ reactions. This measurement gave the Sigma-p s-wave scattering length and the effective range, but the uncertainties were quite large. The statistics for the ΣN-scattering events was very low

because the Σ hyperon immediately decayed after the ΣN scattering due to the short lifetime of the Σ hyperon.

The $\Sigma^{\pm}p$ scattering was measured with a scintillating fiber active target in the KEK-PS E251 and E289 experiments which were conducted since 1999 [13, 14, 15]. $\Sigma^{\pm}$ beams were produced via the $\pi^{\pm}p \rightarrow \Sigma^{\pm}K^{+}$ reactions. The Σ^{+} and Σ^{-} beam momentum ranges were 300–750 MeV/c and 400–700 MeV/c, respectively. The differential cross sections of the $\Sigma^{+}p$ scattering were obtained. However, the statistical errors were too large to constrain theoretical models.

1.3 Experimental studies on Σ-nucleus interaction

Since it is difficult to directly study the ΣN interaction via the scattering experiment, the ΣN interaction in the nuclear medium (the Σ-nucleus interaction) has been studied by investigating the structure of a Σ-nucleus bound system.

1.3.1 X-ray measurement of Σ^{-} atom

An exotic atom is formed when a negatively charged hadron is trapped in an atomic level instead of an electron. The energies of the atomic levels which are mainly determined by the Coulomb interaction are shifted due to the strong interaction between the trapped hadron and the nucleus. By measuring the energy shifts of the characteristic X-rays, the strong interaction between the hadron and the nucleus can be studied.

Experiments on the Σ^{-} atom were conducted using the Σ^{-} hyperon produced via the $K^{-}p \rightarrow \Sigma^{-}\pi^{+}$ and the $K^{-}n \rightarrow \Sigma^{-}\pi^{0}$ reactions [16, 17, 18]. Currently, X-rays from Σ^{-} atoms at A = 12–208 have been measured. From a theoretical analysis on the experimental data, the Σ-nucleus potential was suggested to be attractive at the nuclear surface [19, 20]. However, the Σ-nucleus potential inside the nucleus was poorly determined.

1.3.2 Search for Σ hypernuclei

From the fact that Λ hypernuclei exist, the Λ-nucleus interaction is considered to be attractive. If the Σ-nucleus interaction is also attractive enough to bound the Σ hyperon inside the nucleus, Σ hypernuclei should exist. Therefore, Σ hypernuclei were experimentally searched for in the mass number region of $A \leq 16$ until 2000.

As mentioned in Sec. 1.1, the natural width of Σ hypernuclei should be broad. However, two narrow structures ($\Gamma \leq 8$ MeV) were suggested in the $^{9}\text{Be}(K^{-}, \pi^{-})X$ reaction in 1980 [21]. Similar structures were reported using targets such as ^{6}Li and ^{16}O for the $(K^{-}, \pi^{\pm})$ reaction [22, 23, 24]. On the other hand, as for ^{2}H, ^{3}He, and ^{7}Li targets, such a narrow structure was not observed [25, 22, 26]. In addition, as for ^{12}C targets, such a narrow structure was observed at CERN [27] but was not observed at KEK [28]. To clarify whether Σ hypernuclei exist or not, the $^{9}\text{Be}(K^{-}, \pi^{-})X$ reaction was measured again with high statistics in 1995 [29]. The suggested two narrow structures

of the Σ hypernucleus were not observed in this experiment. Then this result denied the old report claiming the existence of Σ hypernuclei with narrow widths.

1.3.3   Observation of ground state of $^4_\Sigma$He

The first clue to the Σ hypernucleus was found from an experimental search for $^4_\Sigma$He. The KEK-PS E167 collaboration reported a bump structure in a missing-mass spectrum of the ^{4}He(stopped $K^-, \pi^-)X$ reaction in 1989 [25]. This structure was considered to be a bound state of $^4_\Sigma$He. The binding energy and the width were reported to be $B_{\Sigma^+} = 3.2 \pm 0.3^{+0.1}_{-1.1}$ MeV and $\Gamma = 4.6 \pm 0.5^{+1.6}_{-1.3}$ MeV, respectively, with the missing-mass resolution of 2.1 ± 0.2 MeV at the full width at half maximum (FWHM). After the first report, they updated the result to be $B_{\Sigma^+} = 2.8 \pm 0.7$ MeV and $\Gamma = 12.1 \pm 1.2$ MeV by subtracting the background from the in-flight $\Lambda \to p\pi^-$ and $\Sigma^- \to n\pi^-$ decays [30]. However, it was theoretically suggested that the observed structure might be a threshold cusp at the $3N\Sigma$ threshold, and thus it was not regarded as the evidence of the $^4_\Sigma$He nucleus [31].

After the KEK-PS E167 experiment, the $^4_\Sigma$He hypernucleus was searched for again at AGS in BNL using in-flight reactions. The BNL-AGS E774 collaboration measured the ^{4}He(in-flight $K^-, \pi^\pm)X$ reaction at $p_{K^-} = 600$ MeV/c by tagging Λ from the $^4_\Sigma$He hypernucleus. However, the statistics was not high enough for the confirmation. Finally, the BNL-AGS E905 collaboration measured the missing-mass spectra of the ^{4}He(in-flight $K^-, \pi^\pm)X$ reactions at $p_{K^-} = 600$ MeV/c in 1992 [32]. Only events in the scattering angle around $4°$ were selected by using the Moby Dick spectrometer to avoid a huge number of background events from the beam kaon decay. The open and hatched spectra in Fig. 1.2 show the missing-mass spectra in the (K^-, π^-) and (K^-, π^+) reactions, respectively. In the (K^-, π^+) reaction, only the Σ quasi-free production process was observed. On the other hand, in the (K^-, π^-) reaction, a peak due to the ground state of $^4_\Sigma$He was clearly observed below the ^{3}H $+ \Sigma^+$ mass threshold. The binding energy and the natural width were estimated to be $B_{\Sigma^+} = 4.4 \pm 0.3 \pm 1$ MeV and $\Gamma = 7.0 \pm 0.7$ $^{+1.2}_{-0.0}$ MeV, respectively.

The Σ hypernucleus has been observed in the ^{4}He$(K^-, \pi^-)X$ reaction while no bound state has been observed in the ^{4}He$(K^-, \pi^+)X$ reaction. The ^{4}He$(K^-, \pi^+)X$ reaction populates the $T = 3/2$ state only, whereas the ^{4}He$(K^-, \pi^-)X$ reaction populates both the $T = 1/2$ and $3/2$ states. This result indicates the isospin of $^4_\Sigma$He is $T = 1/2$ and agrees with the theoretical analysis suggesting that $T = 1/2$ is dominant in $^4_\Sigma$He.

1.3.4   Studies of Σ nucleus interaction in heavy nuclei

The missing-mass distribution of the quasi-free Σ production process also gives the information of the Σ-nucleus interaction. The missing-mass spectrum of the (stopped K^-, π^+) reaction on ^{12}C was analyzed in 1988 [33] by assuming the following Woods-Saxon type Σ-nucleus potential

$$U = (V + iW)/[1 + \exp((r - R)/a)]. \tag{1.1}$$
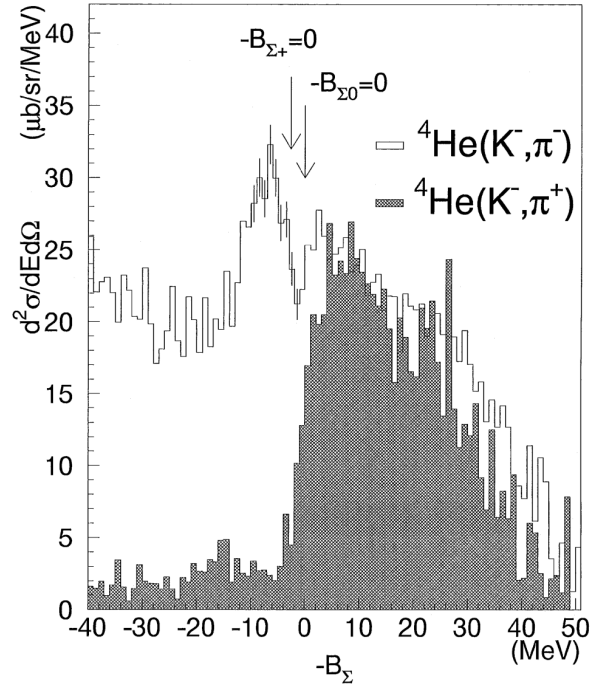
Figure 1.2: Missing-mass spectra of the ^{4}He(in-flight $K^-, \pi^\pm)X$ reaction reported by the BNL E905 collaboration in 1992 [32].

The analysis suggested $V > -12$ MeV and $W < -7$ MeV. In 2002, the missing-mass spectra of the $A(\pi^-, K^+)X$ reaction on heavy nuclear targets (^{28}Si, ^{58}Ni, ^{115}In, and ^{209}Bi) were systematically measured in the KEK-PS E438 experiment [34, 35]. The theoretical analysis of the missing-mass spectrum of the ^{28}Si$(\pi^-, K^+)X$ reaction indicated $V = 30$ MeV and $W = -40$ MeV [36]. Therefore, the Σ-nucleus interaction in heavy nuclei was found to be repulsive.

1.4 Theoretical studies of Σ-nucleus interaction

The Σ-nucleus potential U_Σ is generally written as

$$U_\Sigma = U_\Sigma^0 + U_\Sigma^\tau (T_{core} \cdot t_\Sigma)/A_{core}, \qquad (1.2)$$

where U_Σ^0 is the isospin independent or isospin averaged term, and the second term is isospin dependent term called Lane's term. A_{core} is a mass number of the core nucleus, whereas T_{core} and t_Σ are isospin operators of a core nucleus and Σ, respectively. The isospin of Σ is $t_\Sigma = 1$. The value of $T_{core} \cdot t_\Sigma$ is determined by the total isospin $T = T_{core} + t_\Sigma$. Thus, depending on the total isospin, the Lane's term can appear as either repulsive or attractive. Since the Lane's term is relatively small with large A_{core}, U_Σ^0 is dominant for heavy nuclei. From the experimental results on heavy nuclei mentioned in Sec. 1.3.4, U_Σ^0 is believed to be repulsive.

For the $^4\text{He}(K^-, \pi^\pm)X$ reactions, since A_{core} is small, contribution from the Lane's term is not negligible. In the $^4\text{He}(K^-, \pi^+)X$ reaction, the isospin of the final state is $(T, T_3) = (3/2, -3/2)$. This means only Σ hypernucleus with $T = 3/2$ can be generated, and no bound state was observed in the $^4\text{He}(K^-, \pi^+)X$ reaction. The bound state of $^4_\Sigma\text{He}$ has been observed in the $^4\text{He}(K^-, \pi^-)X$ reaction in which both of $(T, T_3) = (3/2, 1/2)$ and $(1/2, 1/2)$ are allowed. Therefore, the bound state is considered to have $T = 1/2$. The Lane's term can explain the fact that the bound state of $^4_\Sigma\text{He}$ was observed in the $T = 3/2$ channel only as this term are the opposite sign for the $T = 3/2$ and $T = 1/2$ channels.

1.4.1 The Σ-nucleus potential

A theoretical analysis was performed to reproduce the missing-mass spectra of the $^4\text{He}(\text{in-flight } K^-, \pi^-)X$ and $^4\text{He}(\text{stopped } K^-, \pi^-)X$ reactions in the mass region from the ground state of $^4_\Lambda\text{He}$ to the quasi-free Σ production [37]. In the analysis, the Λ-nucleus potential $U_{\Lambda,T}$ and the Σ-nucleus potential $U_{\Sigma,T}$ when the total isospin was T were assumed to be

$$U_{\Lambda,T} = V_{\Lambda,T} + iW_{\Lambda,T}, \tag{1.3}$$

$$U_{\Sigma,T} = V_{\Sigma,T} + iW_{\Sigma,T}, \tag{1.4}$$

respectively. Here, $V_{\Lambda,T}$, $W_{\Lambda,T}$, $V_{\Sigma,T}$, and $W_{\Sigma,T}$ are the real and imaginary parts of the Λ-nucleus and Σ-nucleus potentials, respectively. While $W_{\Lambda,T}$ was introduced to take into account the Λ escape and the core breakup processes, $W_{\Sigma,T}$ contains also the Σ-Λ conversion processes. The pole of $^4_\Sigma\text{He}$ was discussed together with the pole of $^4_\Lambda\text{He}$ because the ΛN-ΣN mixing is considerably large. $U_{\Sigma,T=1/2}$, $U_{\Sigma,T=3/2}$, and $U_{\Lambda,T=1/2}$ were determined by fitting the missing-mass spectra for the $^4\text{He}(K^-, \pi^\pm)X$ reactions.

Figures 1.3 and 1.4 show the real part and the imaginary part of the $3N$-Y potential [37]. $V_{\Lambda,T=1/2}$ had a repulsive core with a height of 30 MeV and an attractive pocket with a depth of -10 MeV. $V_{\Sigma,T=1/2}$ had a repulsive core with a height of 20 MeV and an attractive pocket with a depth of -30 MeV. $V_{\Sigma,T=3/2}$ had a repulsive core with a height of 120 MeV and a shallow attractive pocket. The depths of $W_{\Sigma,T=1/2}$ and $W_{\Sigma,T=3/2}$ are -30 MeV and -1 MeV, respectively.

1.4.2 Theoretical analysis on the missing-mass spectra

The theoretical analysis attempted to reproduce the measured missing-mass spectra of the $^4\text{He}(K^-, \pi^-)X$ reaction in the KEK and BNL experiments using above potentials. The ground state in which the Σ hyperon occupies the $L = 0$ orbit around the ^3H or ^3He core, is denoted as 0^+ in Figs. 1.5 and 1.6. The excited state denoted as 1^- in which the Σ hyperon occupies the $L = 1$ orbit, should be populated, but the peak or bump structure was not observed in these experiments. To reproduce the experimental spectra, the strength of the potential for the excited state was normalized. The normalized Σ-nucleus potential for the $L = 1$ state U'_Σ was introduced as

$$U'_\Sigma = V'_\Sigma + iW'_\Sigma. \tag{1.5}$$
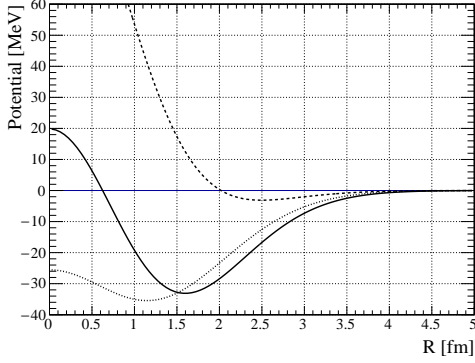
Figure 1.3: Real part of the $3N$-Y potential with $J^\pi = 0^+$ on the isospin basis at the Σ threshold. The solid curve, dashed curve and dotted curve denote $V_{\Sigma,T=1/2}$, $V_{\Sigma,T=3/2}$ and $V_{\Lambda,T=1/2}$.
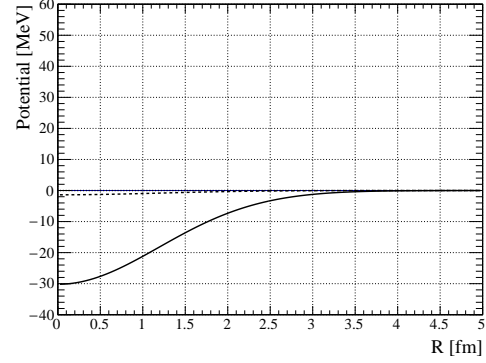
Figure 1.4: Imaginary part of the $3N$-Y potential with $J^\pi = 0^+$ on the isospin basis at the Σ threshold. The solid curve, dashed curve and dotted curve denote $W_{\Sigma,T=1/2}$, $W_{\Sigma,T=3/2}$ and $W_{\Lambda,T=1/2}$.

V'_Σ and W'_Σ were defined as

$$
\begin{aligned}
V'_\Sigma &= N_R V_\Sigma, \\
W'_\Sigma &= N_I W_\Sigma,
\end{aligned}
\tag{1.6}
$$

respectively. Here, N_R and N_I are the normalization factors for the $L = 1$ state. From the experimental spectra of the BNL-AGS E905 and the KEK E167 results, the normalization factors of $(N_R, N_I) = (0.6, 0.9)$ and $(0.5, 0.5)$ were obtained, respectively [37, 38]. The measured spectra are reasonably well reproduced by using the normalization fac-
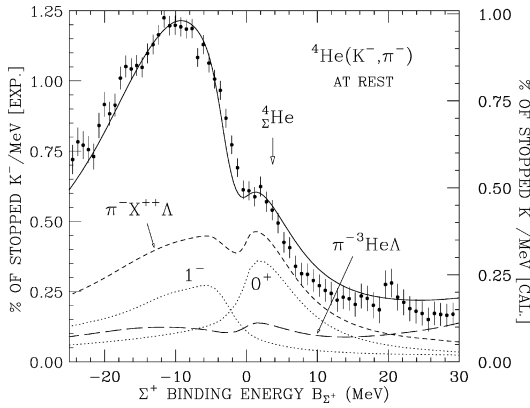
Figure 1.5: The theoretical analysis in the ^{4}He(in-flight $K^-, \pi^-)X$ reaction [37].
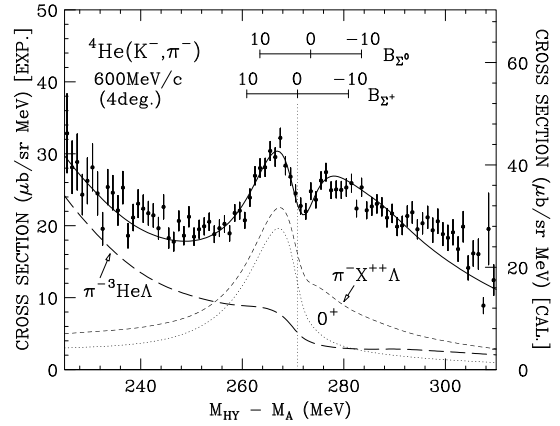
Figure 1.6: The theoretical analysis in the ^{4}He(stopped $K^-, \pi^-)X$ reaction [38].

tors as shown in Figs. 1.5 and 1.6. However, this result is quite uncertain because the normalization factors optimized for the two experiments are not consistent with each

other. It is unclear whether this prescription is correct or not because no $L = 1$ state
was not observed in these experiments.

The ^{4}He$(K^-, \pi^-)X$ reaction converts p or n in the $L = 0$ orbit in ^{4}He to Σ^+ or
Σ^0. To populate Σ in the $L = 1$ orbit, angular momentum transfer of $\Delta L = 1$ is
necessary. Since the momentum transfer is small in the ^{4}He$(K^-, \pi^-)X$ reaction at the
beam momentum $p_{K^-} = 0.6$ GeV$/c$ and at the scattering angle around $4°$, the angular
momentum transfer of $\Delta L = 0$ is preferable. This might be the reason why the excited
state was not observed in the BNL E905 experiment.

In the KEK E167 experiment, where the (stopped K^-, π^-) reaction was measured,
the larger momentum $\Delta p \sim 160$ MeV$/c$ can be transferred than that in the BNL E905
experiment. Thus, it was expected that the $\Delta L = 1$ transition was enhanced. However,
in the case of the stopped K^- reaction, the angular momentum can be transferred
also from the atomic orbit just before the K^- absorption by nuclei. Since the angular
momentum of the atomic orbit in the initial state should be taken into account, it is
unclear whether the $\Delta L = 1$ transition populates the $L = 1$ state or not.

In order to determine the Σ-nucleus potential for the $L = 1$ state reliably, it is
necessary to identify the $L = 1$ state and determine the cross section for this state
by measuring the (in-flight K^-, π^-)X reaction at larger momentum transfer than the
BNL-AGS E905 experiment.

1.5 J-PARC E13 experiment

As discussed in the previous section, the $L = 1$ state should be searched for to exam-
ine the Σ-nucleus interaction. To realize this, the following experimental conditions are
proposed. To reduce the uncertainty in the angular momentum transfer, the (in-flight
K^-, π^-) reaction should be used. Using a K^- beam at the high momentum, the mo-
mentum transfer in the (K^-, π^-) reaction becomes larger, and thus the $L = 1$ state
should be effectively populated .

The J-PARC E13 experiment was proposed as an experiment to realize the above
conditions. In the experiment, the Σ-nucleus interaction was studied by measuring a
missing-mass spectrum of the ^{4}He(in-flight K^-, π^-)X reaction at the angular range of
2–14 degrees using a K^- beam at 1.5 GeV$/c$. With these conditions, the momentum
transfer of 230–370 MeV$/c$ is large enough to populate the $L = 1$ state as shown in
Fig. 1.7

Figure 1.8 shows the theoretical prediction of the missing-mass spectrum at $p_{K^-} =$
1.5 GeV$/c$ and $\theta = 8°$ with $(N_R, N_I) = (0.6, 0.9)$ and $(1, 1)$ [39]. In the $(1, 1)$ case, the
$L = 1$ state shown as 1^- should be strongly excited. On the other hand, in the $(0.6, 0.9)$
case, the structure of the $L = 1$ state can not be seen clearly. Furthermore, in the $(0.6,$
$0.9)$ case, the central energy of excited state is shifted towards the heavier missing mass
than in the $(1,1)$ case because the shallower real part of the Σ-nucleus potential causes
the smaller binding energy. In addition, the reduced imaginary part of the potential
enhances the yields. Since the central energy and the yield depend on the strengths of
the real and imaginary parts of the potential, respectively, the central energy and the

yield of the excited state provide impotrant insight for the potential.

In this thesis, the experimental details and the result of the J-PARC E13 experiment are reported.
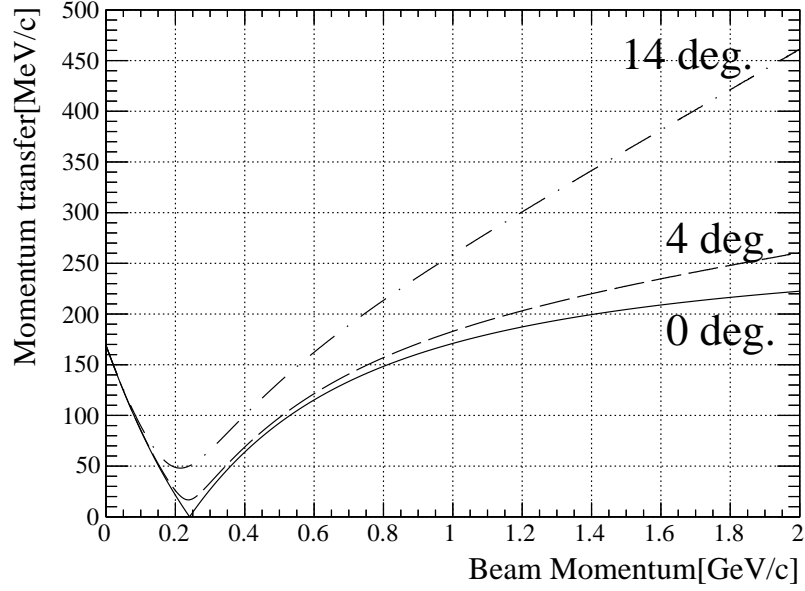
Figure 1.7: The momentum transfer of the ^{4}He$(K^-, \pi^-)\Sigma$ reaction as a function of the beam momentum. Solid, dashed, and dot-dashed lines show the momentum transfer at the π^- scattering angles of 0, 4, and 14 degree, respectively.
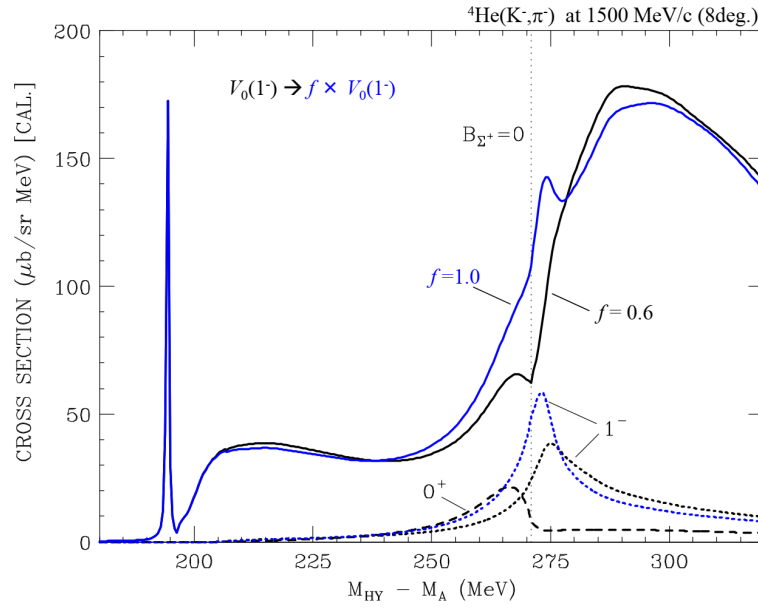
Figure 1.8: The theoretical prediction of the missing-mass spectra for the ^{4}He$(K^-, \pi^-)X$ reaction at $p_{K^-} = 1.5$ GeV/c and $\theta = 8°$ with $(N_R, N_I) = (0.6, 0.9)$ and $(1, 1)$ [40]. The blue and black solid lines show the expected missing-mass spectra with $(0.6, 0.9)$ and $(1, 1)$, respectively. The black dashed line shows the component of the ground state of $^4_\Sigma$He. The blue and black dotted lines show the component of the excited state with $(0.6, 0.9)$ and $(1, 1)$, respectively.

Chapter 2

Experiment

The data used in this study was taken in the J-PARC E13 experiment carried out in 2015 at the K1.8 beam line, J-PARC. In this chapter, the experimental setup including the beam line, the target and the spectrometers is explained. The data-acquisition system and the data summary are also described.

2.1 J-PARC

J-PARC stands for Japan Proton Accelerator Research Complex located in Tokai, Ibaraki, Japan. J-PARC has accelerators and experimental facilities to use high-intensity proton beams. J-PARC has three accelerators: a linear accelerator (Linac), a Rapid Cycling Synchrotron (RCS) and a synchrotron (MR: Main Ring). J-PARC also has three experimental facilities: Materials and Life science experimental Facility (MLF), Neutrino experimental facility (NU), and Hadron experimental facility (HD).

H$^-$ ions are generated by an ion source in Linac and boosted up to 400 MeV (50 mA) and then transported to RCS. At the injection section of RCS, electrons in the H$^-$ ions are stripped off by a thin foil of carbon, and H$^+$ beams (proton beams) are produced. The proton beams are accelerated up to 3 GeV in RCS, and transported to MLF and MR. The proton beams are accelerated up to 30 GeV in MR, and are extracted to HD and NU.

In this experiment, the repetition rate of the beam spill was 6.0 s, and the beam duration time was 2.1 s. 2.5×10^{13} protons per spill were irradiated on the primary target in the 24 kW accelerator operation.

2.2 Hadron experimental facility

Various hadron and nuclear physics experiments are conducted in HD. The proton beams extracted from MR are injected to the primary gold target. Reactions between beam protons and the gold target generate various secondary particles such as protons, neutrons, K mesons, π mesons, antiprotons, and so on. The acceleration cycle is about six seconds for HD. Secondary particles are shared by several beam lines. HD has three

secondary beam lines in 2015, which are so-called K1.8, K1.8BR, and KL beam lines. The J-PARC E13 experiment for this study was conducted in the K1.8 beam line.

2.3   K1.8 beam line

The K1.8 beam line was designed for experiments of strangeness nuclear physics using π and K meson beams with the maximum momentum of 2.0 GeV/c. In order to obtain high purity kaon beam, there were two mass separation sections and the intermediate focus slit. The secondary beams which have a specific charge, mass, and momentum were transported.

In this experiment, the K^- intensity at the experimental target was 3×10^5 per spill with the K^-/π^- ratio of 2-3 at the beam momentum of 1.5 GeV/c. The specifications of the K1.8 beam line and the experimental beam conditions are summarized in Tables 2.1 and 2.2, respectively.

Table 2.1: The specifications of the K1.8 beam line.

Maximum momentum	2.0 GeV/c
Production target	gold
Target thickness	66 mm
Production angle	6°
Momentum bite	±3%
Beam line length	46 m

Table 2.2: The experimental beam condition.

Primary proton momentum	30 GeV/c
Primary proton intensity	2.5×10^{13}/spill
Repetition cycle	6 s
Spill length	2.1 s
Secondary K^- momentum	1.5 GeV/c
Secondary K^- intensity	$\sim 3 \times 10^5$/spill
K^-/π^-	2-3

2.4   Experimental setup

The experimental setup of the spectrometers is shown in Fig. 2.1. The momenta of the K^- beam and the scattered π^- were measured using the K1.8 beam line and the SKS spectrometer systems, respectively. The SKS system has a wide momentum acceptance

to cover a large momentum range of 1.1-2.0 GeV/c and a wide angular acceptance 0°-14° to produce the exited states of hypernuclei. The missing-mass resolution achieved 5 MeV (FWHM).
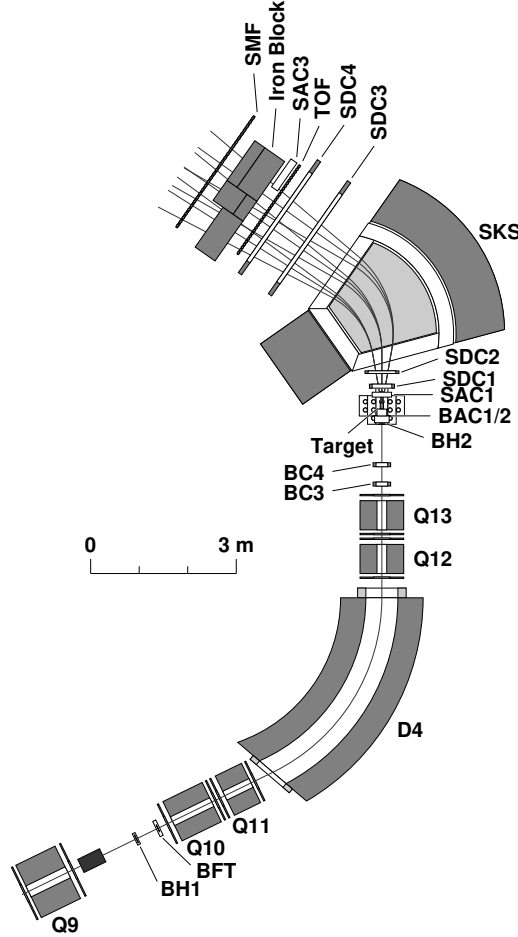
Figure 2.1: The setup of the K1.8 beam line and the SKS spectrometers.

2.4.1 K1.8 beam line spectrometer

The K1.8 beam line spectrometer consisted of magnets, trackers and time-of-flight detector. The spectrometer analyzed a momentum and a trajectory of each secondary beam particle. A schematic view of the K1.8 beam line spectrometer is shown in the lower part of Fig. 2.1. The K1.8 beam line spectrometer was the QQDQQ magnet system which was a combination of one dipole (D4) and four quadrupole magnets (Q10, Q11, Q12 and Q13). The designed momentum resolution is 3.3×10^{-3} (FWHM) [41]. The specification of the K1.8 beam line spectrometer is summarized in Table 2.3.

Beam hodoscopes and beam line trackers were placed in front of and behind the

Table 2.3: The specifications of the K1.8 beam line spectrometer.

Momentum resolution	3.3×10^{-4}(FWHM)
Maximum momentum	2.0 GeV/c
Bending angle	60°
Flight path	11.2 m
Effective length (D4)	4 m

QQDQQ magnets. The beam hodoscopes (BH1 and BH2) were for a measurement of the time-of-flight of beam particles. The beam line trackers (BFT, BC3 and BC4) were for a measurement of trajectories of beam particles. Čerenkov counters (BAC1 and BAC2) for an identification of beam particles were placed just in front of the experimental target. BH2, BAC1, and BAC2 were used to create a trigger signal.

Beam hodoscopes

Beam Hodoscope 1 and 2 (BH1 and BH2) were plastic scintillation counters for time-of-flight measurement. Both hodoscopes consisted of segmented scintillators (SAINT-GOBAIN, BC420), acrylic light guides and PMTs (Hamamatsu, H6524MOD) as shown in Figs. 2.2 and 2.3. The thicknesses of scintillators for BH1 and BH2 were 5 mm and 8 mm, respectively. BH1 and BH2 had the effective areas of 170 mm (horizontal) × 66 mm (vertical) and 111 mm (horizontal) × 50 mm (vertical), respectively. Each segment of BH1 and BH2 had overlaps with neighboring segments to get rid of ineffective area. The numbers of the segmentation of BH1 and BH2 were eleven and five, respectively. For BH1, PMTs were connected via the light guides on the both sides of the scintillator. For BH2, PMTs were connected via the light guides on the bottom side of the scintillator. The resolution of time-of-flight is about 200 ps (σ).

Beam line trackers

The beam line trackers for a measurement of beam trajectories were a fiber tracker (BFT) and drift chambers (BC3 and BC4). The beam momentum was reconstructed from straight track measured by BC3 and BC4 and a horizontal hit position at BFT together with a transport matrix of the QQDQQ magnet system.

BFT was a tracking detector consists of scintillating fibers (Kuraray SCSF-78MJ) and Multi-Pixel Photon Counter (MPPC, Hamamatsu S12571-100P). The fibers are arranged horizontally in x and x' planes as shown in Fig. 2.4. Each plane had 160 scintillating fibers with a diameter of 1 mm and 160 MPPCs. Each fiber had 0.5 mm overlaps with neighboring fibers to cover insensitive areas due to claddings in fibers. Each MPPC was connected to the one side of a fiber. The effective area was 160 mm (horizontal) × 80 mm (vertical). The timing resolution is about 0.8 ns (σ). The position resolution is about 150 μm (σ).

Each drift chamber of BC3 and BC4 consisted of x, x', u, u', v and v' sense wire
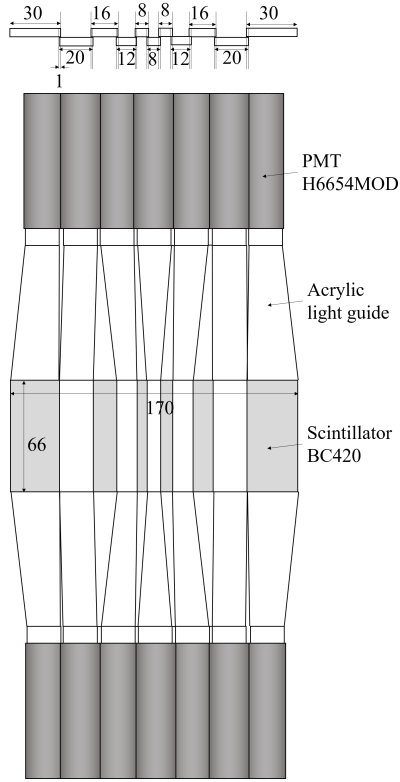
Figure 2.2: The schematic view of BH1.
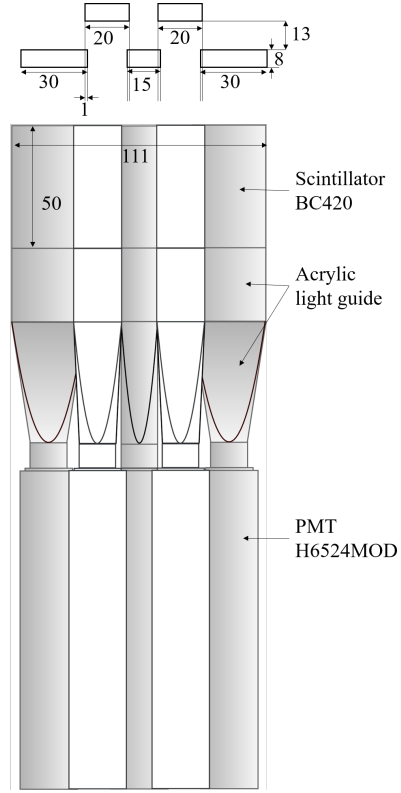
Figure 2.3: The schematic view of BH2.
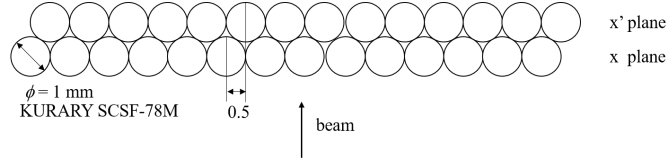
Figure 2.4: The plane structure of BFT.

planes. A pair of two layers such as xx′, uu′ or vv′ is called as a pair plane. Each plane had sixty-four sense wires. The wire spacing was 3 mm. The effective area was 192 mm (horizontal) × 100 mm (vertical). Wires in the x, u, v pair planes were tilted by 0°, 15° and −15°, respectively. A sense wire was surrounded by two potential wires and two cathode planes as shown in Fig. 2.5 and was made of a gold-plated tungsten wire with a diameter of 12.5 μm. A potential wire was made of a gold-plated beryllium copper wires with a diameter of 75 μm. A cathode plane was made of a carbon-coated Mylar film. The thickness of the film was 12 μm. The position of the cathode plane was 2 mm from wires. The operation voltages of potential wires and cathode planes were −1.24 kV and −1.23 kV, respectively. The sense wires were connected to the ground. Chamber windows were aluminized Mylar film with a thickness of 12.5 μm. The gas mixture was argon of 76 %, iso-butane (C_4H_{10}) of 20 % and dimethoxy-methane ($C_3H_8O_2$) of 4 %,

and was in the atmospheric pressure. The position resolution is about 200 μm (σ).
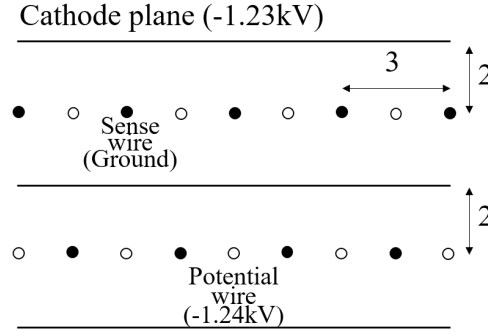
Figure 2.5: The cell structure of BC3 and BC4.

Čerenkov detector for beam particle

Beam Aerogel Čerenkov Counter (BAC) consisted of BAC1 and BAC2 and was a threshold type Čerenkov detector as shown in Fig. 2.6. A silica aerogel with a refractive index of 1.03 was used as a radiator. The refractive index corresponded to the threshold momenta of 0.6 GeV/c for pions and 2.0 GeV/c for kaons. Čerenkov light was detected by six PMTs (Hamamatsu, H6614-70UV) attached to the bottom of a radiator container. The thicknesses of the radiators for BAC1 and BAC2 were 66 mm. The effective area was 160 mm (horizontal) $\times$ 57 mm (vertical). Polytetrafluoroethylene (CF2)$_n$ was used as an inner diffused-type reflector. In the typical beam condition with the momentum of 1.5 GeV/c, the K^- beam trigger efficiency was more than 95% with the π^- beam missidentification ratio of less than 3% in the trigger level.
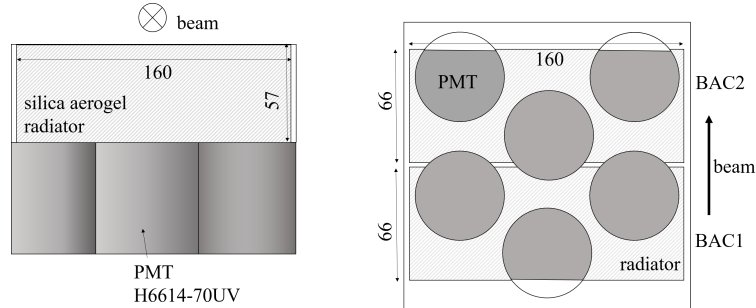
Figure 2.6: The schematic view of BAC. BAC consisted of BAC1 and BAC2.

2.4.2 SKS spectrometer

The SKS spectrometer (Superconducting Kaon Spectrometer) system reconstructed the momentum for scattered particles. The SKS system consisted of a superconducting

dipole magnet, trackers and time-of-flight detectors and had a large acceptance of 100 msr and a momentum resolution of $\Delta p/p \sim 10^{-3}$. A schematic view of the SKS spectrometer is shown in the upper part of Fig. 2.1. Four drift chambers (SDC1, SDC2, SDC3 and SDC4) were employed for measurements of trajectories of scattering particles. A Time-Of-Flight wall (TOF) were employed for a time-of-flight measurement between BH2 and TOF, and a trigger detector. A Čerenkov detector (SAC1) for an identification of the scattered particle was placed just behind the experimental target. In order to reduce the beam through events in trigger level, scintillation counters (SFV) and a Čerenkov detector (SAC3) were placed as beam veto counters just behind TOF. In addition, in order to reduce the $K^- \rightarrow \mu^- \bar{\nu}_\mu$ beam decay events, Muon Filter (SMF) were placed behind TOF.

SAC1, TOF, SAC3, SFV and SMF were used to create a trigger signal. The specification of the SKS system is summarized in Table 2.4.

Table 2.4: The specifications of the SKS system.

Momentum acceptance	$1.1 \sim 2.0$ GeV/c
Momentum resolution	0.3 % (at 1.5 GeV/c)
Bending angle	55° (at 1.5 GeV/c)
Magnetic field (at center)	2.5 T
Solid angle	100 msr
Flight path	$\sim$5 m

Čerenkov detector for scattered particles

Aerogel Čerenkov Counter for Scattered pion (SAC1) was placed just behind the experimental target. SAC1 was a threshold type Čerenkov detector and distinguished ejected pions from beam kaons. A silica aerogel with a refractive index of 1.03 was used as a radiator. The index corresponded to the threshold momenta of 0.6 GeV/c for pions and 2.0 GeV/c for kaons. The thickness of the radiator was 66 mm. Čerenkov light was detected by five PMTs (Hamamatsu, H6614-70UV) attached to the bottom of a radiator container as shown in Fig. 2.7. The effective area was 342 mm (horizontal) $\times$ 80 mm (vertical). The efficiency for π^- is 99%.

Scattered-particle trackers

The SKS spectrometer system had four drift chambers (SDC1, SDC2, SDC3 and SDC4). SDC1 and SDC2 were placed in front of the SKS magnet. SDC3 and SDC4 were placed behind the SKS magnet. Trajectories at spacial positions in front of and behind the SKS magnet were measured by the drift chambers.

SDC1 consisted of x, x', u, u', v and v' planes. Each plane had 78 sense wires. The wire spacing was 5 mm. The effective area was 400 mm (horizontal) $\times$ 150 mm (vertical). Wires in the x, u, v pair planes were tilted by 0°, 15° and −15°, respectively. A sense wire
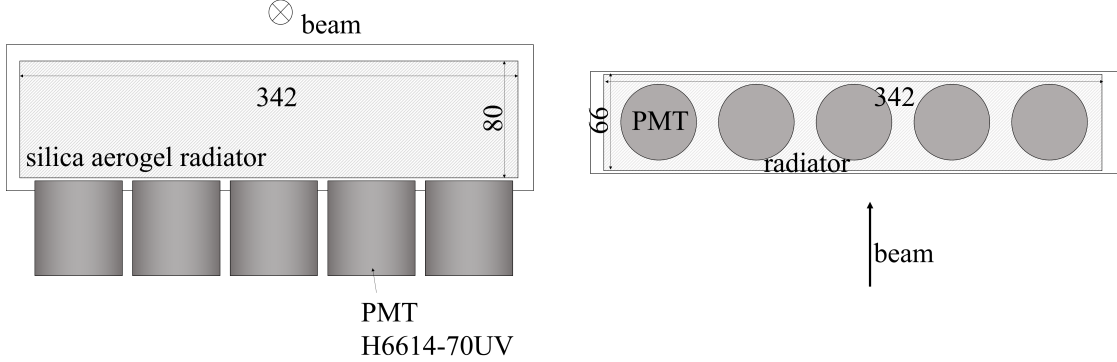
Figure 2.7: The schematic view of SAC1.

was surrounded by two potential wires and two cathode planes as shown in Fig. 2.5 and was made of a gold-plated tungsten wire with a diameter of 12.5 μm. A potential wire was made of a gold-plated beryllium copper wire with a diameter of 75 μm. A cathode plane was made of a carbon-coated Mylar film with a thickness of 12 μm. The position of the cathode plane was 2.5 mm from wires. The operation voltages of potential wires and cathode planes were -1.3 kV. The sense wires were connected to the ground. Chamber windows were aluminized Mylar films with a thickness of 12.5 μm. The gas mixture was argon of 76 %, iso-butane (C_4H_{10}) of 20 %, and dimethoxy-methane ($C_3H_8O_2$) of 4 %, and was in the atmospheric pressure. The position resolution is about 200 μm (σ).

SDC2 had the same structure and gas mixture as that of SDC1 except for following points. SDC2 consisted of x, x', u and u' planes. The effective area was 560 mm (horizontal) $\times$ 150 mm (vertical). Each plane had 112 sense wires. The operation voltages of potential wires and cathode planes are -1.4 kV.

SDC3 and SDC4 consisted of x, u, v, x', u' and v' planes. The x plane had 108 sense wires. The u and v planes had 120 wires. The wire spacing was 20 mm. Wires in the x, u and v planes were tilted by $0°$, $30°$ and $-30°$, respectively. The effective area was 2140 mm (horizontal) $\times$ 1140 mm (vertical). A sense wire was surrounded by potential and cathode wires as shown in Fig. 2.5 and was made of a gold-plated tungsten wire with a diameter of 25 μm. A potential wire and a cathode wire were made of a gold-plated beryllium copper wires with a diameter of 80 μm. The position of a cathode wire plane was 6 mm from sense wires. The operation voltages of sense, the 1st potential and the 2nd potential wires were 2.2 kV, -0.35 kV and -0.45 kV, respectively. Cathode wires were connected to the ground. A gas mixture was argon of 50 % and ethane (C_2H_6) of 50 %, and was in the atmospheric pressure. The position resolution is about 250 μm (σ).

Time-of-flight wall

A Time-Of-Flight wall (TOF) was an array of plastic scintillation counters for time-of-flight measurement. Schematic view of TOF is shown in Fig. 2.9. Each plastic scin-
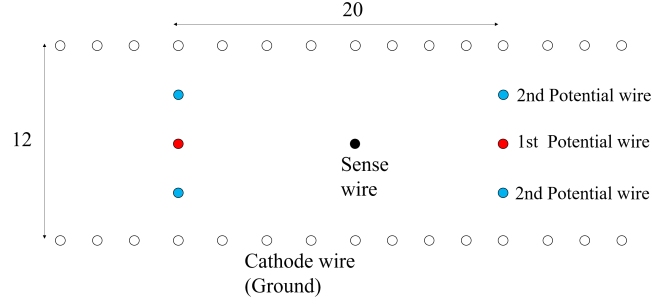
Figure 2.8: The cell structure of SDC3 and SDC4

tillation counter consisted of a plastic scintillator (SAINT-GOBAIN, BC410), acrylic light guides, and PMTs (Hamamatsu, H1949). TOF had an effective area of 2240 mm (horizontal) × 1000 mm (vertical) and was segmented to improve the time resolution in each segment. The number of segmentation was 32. The thickness of the scintillators were 30 mm. The PMTs were connected via the light guides on the both sides of the scintillator. The resolution of time-of-flight between BH2 and TOF is about 150 ps (σ).
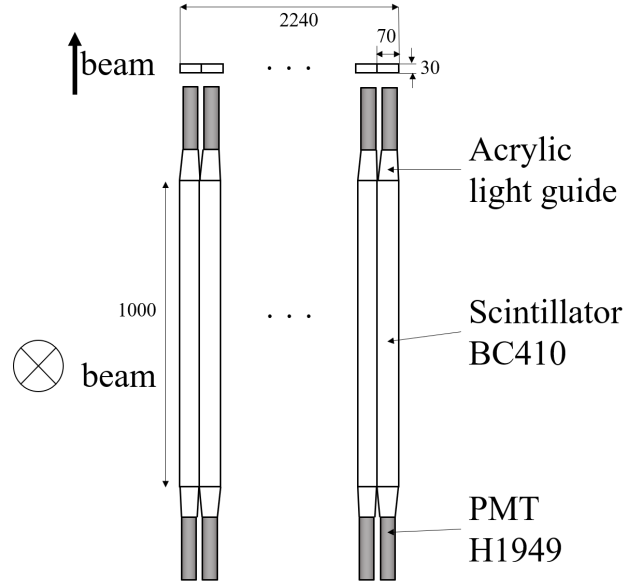
Figure 2.9: The schematic view of TOF.

Beam kaon veto counters

Beam kaon veto counters consisted of plastic scintillation counters (SFV) and an aerogel Čerenkov counter (SAC3) as shown in Figs. 2.10 and 2.11, respectively. The effective area of SFV and SAC3 covered profile of K^- beams which path through the SKS magnet.

SFV and SAC3 were placed behind TOF.

SFV was an array of plastic scintillation counters which identified charged particles. Each plastic scintillation counter consisted of a plastic scintillator (SAINT-GOBAIN, BC420), an acrylic light guide and PMT (Hamamatsu, H3167). The effective area was 400 mm (horizontal) × 200 mm (vertical) and was segmented to decrease the beam hit rate. The thickness of the scintillator was 8 mm. The number of segmentation was six. Each segment had overlaps with neighboring segments to avoid ineffective areas. PMTs were connected via the light guides on upside of the scintillator.

SAC3 was a threshold type Čerenkov detector. A silica aerogel with a refractive index of 1.028 corresponding to the threshold momenta of 0.6 GeV/c for pions and 2.0 GeV/c for kaons was used as a radiator. Čerenkov light was detected by 16 PMTs (Hamamatsu, R6681) attached to the top and bottom side of a radiator container. The thickness of the radiator was 120 mm. The effective area was 400 mm (horizontal) × 200 mm (vertical). The efficiency for π^- is 99%.
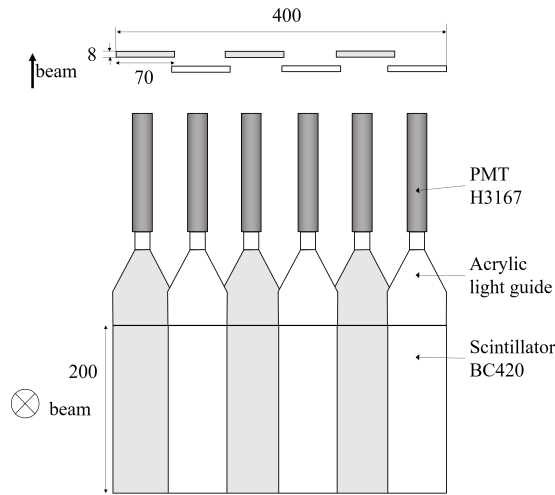
Figure 2.10: The schematic view of SFV.
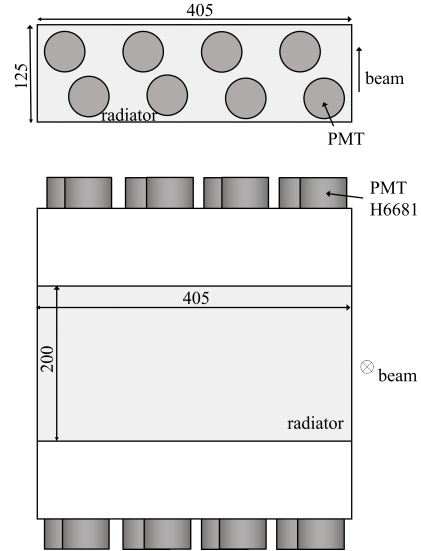
Figure 2.11: The schematic view of SAC3.

Muon filter

Muon Filter (SMF) was placed behind TOF as shown in Fig. 2.12 and was an array of Čerenkov counters (LC) and iron blocks. The iron blocks with thicknesses of 50 cm and 70 cm were placed in front of LC. Each Čerenkov counter consisted of an acrylic radiator, acrylic light guides and PMTs (Hamamatsu, H1949 and H6410). The threshold of the acrylic radiator was low enough to detect pions and kaons. The PMTs were connected via the light guides on the both sides of the radiator. The number of segmentation of SMF was 28. The effective area was 2800 mm (horizontal) × 1400 mm (vertical). The thickness of the radiator was 40 mm.
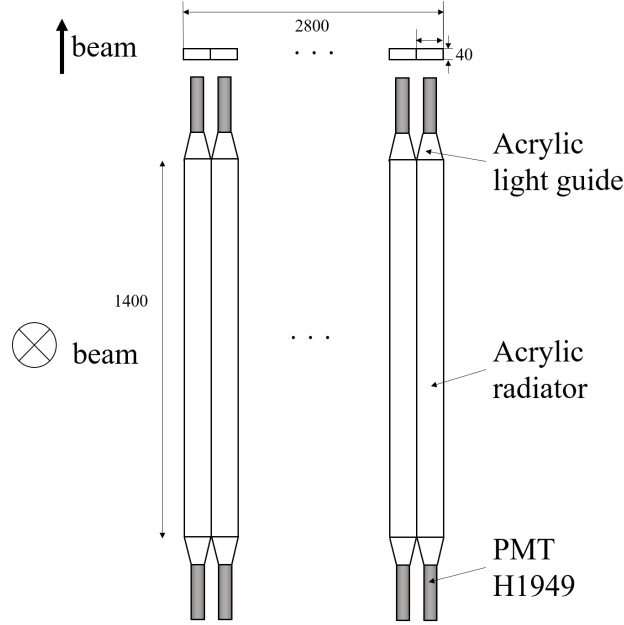
Figure 2.12: The schematic view of SMF.

2.4.3 Liquid ^{4}He target

A liquid ^{4}He target was used. The density was estimated to be of 0.125 g/cm^3 from the temperature and the reservoir gas pressure. The stability of the liquid helium density was $\Delta\rho/\rho < 10^{-5}$ during the physics run.

The liquid ^{4}He target cell is shown in Fig. 2.13 and consisted of a target vessel, a radiation shield and a vacuum chamber. These components had cylindrical shapes. The target vessel was made of stainless steel (SUS). The thicknesses of the cylindrical part and the windows of the target vessel were 0.2 mm and 0.1 mm, respectively. The target vessel length was 218 mm along the beam direction. The target length became 10±4 mm longer than the vessel size by pressure under operation. The radiation shield was made of aluminum. Thicknesses of both the cylindrical part and the windows were 0.2 mm. The vacuum chamber was made of aluminum for the cylindrical part, Mylar for the upstream window and G10 for the downstream window. The thicknesses of the cylindrical part, the upstream and downstream windows were 2 mm, 0.3 mm and 0.5 mm, respectively. Specifications of the liquid ^{4}He target cell are summarized in Table 2.5.

2.4.4 Trigger

In order to select the (K^-, π^-) reaction events efficiently, the (K, π) trigger was defined as follows.

$$(K, \pi) \equiv Kin \times \pi out \qquad (2.1)$$

Table 2.5: The specifications of the liquid ^{4}He target cell.

Diameter	120 mm
Length	218 mm
Volume	2466 cm^3
Liq. helium density	0.125 g/cm^3
liq. ^{4}He thickness	2.8 g/cm^2
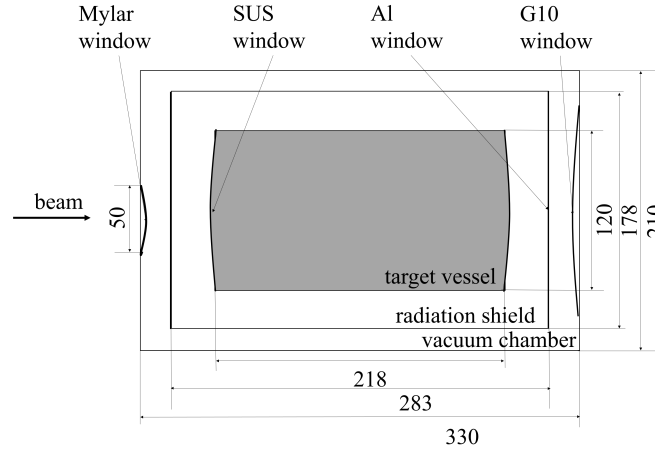
Figure 2.13: The schematic view of the target cell.

To identify an event for that beam particle was K^- and not π^-, the Kin trigger selected an event with a hit in BH2 and not in BAC1 nor BAC2 as shown in Eq. (2.2).

$$Kin \equiv BH2 \times \overline{BAC1} \times \overline{BAC2} \tag{2.2}$$

To identify an event for that scattered particle was π^-, the πout trigger selected an event with a hit in TOF and SAC1. In addition to the πout trigger, to reject the K^- event, $\overline{SAC3 \times SFV}$ was required. The πout trigger is shown in Eq. (2.3).

$$\pi out \equiv TOF \times SAC1 \times \overline{\overline{SAC3} \times SFV} \tag{2.3}$$

The $K^- \to \mu^- \bar{\nu}_\mu$ beam decay events were contained in the (K, π) trigger. To reject the decay events, the (K, π)w/SMF trigger required the SMF veto. The (K, π)w/SMF trigger was defined as follows.

$$(K, \pi)\text{w/SMF} \equiv (K, \pi) \times \overline{SMF} \tag{2.4}$$

In the J-PARC E13 experiment, the (K, π)w/SMF trigger was used. The trigger logic diagram is shown in Fig. 2.14.
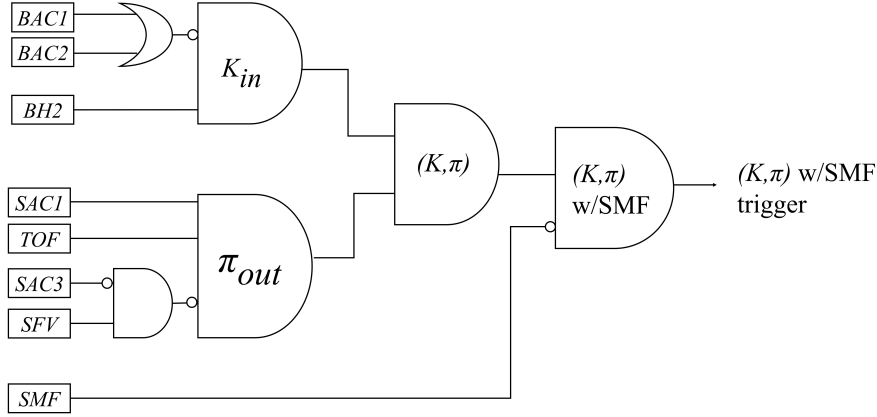
Figure 2.14: The trigger logic diagram.

2.4.5 Data-acquisition system

The DAQ diagram for the J-PARC E13 experiment is shown in Fig. 2.15. The Master Trigger Module (MTM) received a trigger and busy signals from subsystems, and distributed the event and the spill numbers to receiver modules in the subsystems. Signals of BH1, BH2, BAC1, BAC2, SAC1, TOF, SAC3, SFV and SMF were digitized with TKO TDC/ADC modules. Signals of SDC3 and SDC4 were digitized with TKO TDC (Dr.TII) modules. The TKO bus was accessed by the Super Memory Partner module, which was a memory module of VME, via the Super Control Header module. Data on the memory were gathered by the on-board CPU VME controller and transmitted via TCP Ethernet. Signals of BFT were digitized with Extended Analogue Silicon PM Integrated Read-Out Chip (EASIROC) modules [42]. The EASIROC module communicate with a DAQ server via the TCP/IP protocol. Signals of BC3, BC4, SDC1 and SDC2 were digitized with the COmmon Pipe-lined Platform for Electronics Readout-lite (COPPER-lite) modules [43]. The COPPER-lite module communicated with a DAQ server via the TCP/IP protocol.

The data-acquisition (DAQ) system was HD-DAQ [44] which was developed for J-PARC hadron experiments. The DAQ server contained Controller, Event Builder, Event Distributer and Recorder. The Controller sent messages to all systems. The Event Builder collected data from the detectors using the TCP/IP network and sent built data to Event Distributer. The Event Distributer distributed the data to the Recorder and the Online Monitor. The Recorder sent the data to the File Server with a compression.

2.5 Data summary

The J-PARC E13 experiment was performed in April and May 2015. In total, 23 G kaon beams were irradiated on the liquid ^{4}He target with a beam momentum of 1.5 GeV/c. For the momentum calibration of the spectrometer systems, a Σ^+ production run and beam-through runs were taken. A polystyrene target with 2.9 g/cm^2 was used to measure
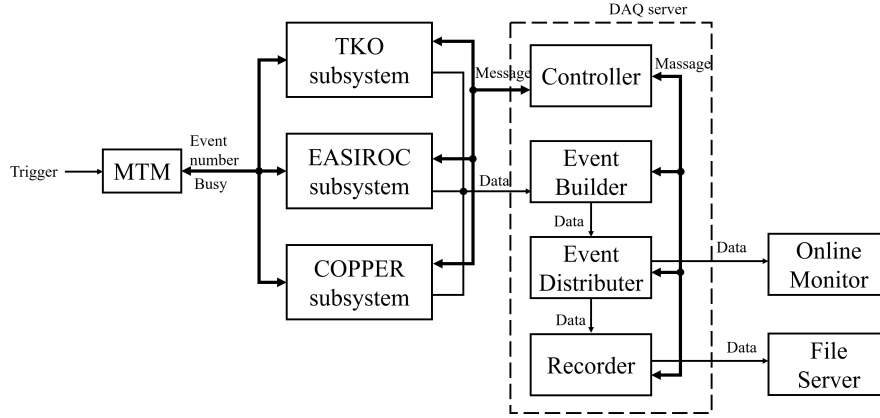
Figure 2.15: The schematic view of DAQ system.

the $p(K^-, \pi^-)\Sigma^+$ reaction. For beam-through runs, beam momenta of 1.2, 1.37, 1.5 and 1.8 GeV/c were used with or without the liquid ^{4}He target. In addition, data with the empty target cell was taken. The data summary was shown in Table 2.6.

Table 2.6: The data summary of the J-PARC E13 experiment.

Purpose	Target	Momentum (GeV/c)	Number of K^-
physics run	^{4}He	1.5	2.3×10^{10}
Σ^+ production	$(CH_2)_n$	1.5, 1.8	1.0×10^9
empty target run	empty cell	1.5	6.0×10^6
beam through	w/ ^{4}He	1.2, 1.37, 1.5, 1.8	1×10^6
beam through	w/o ^{4}He	1.2, 1.37, 1.5, 1.8	2×10^5

Chapter 3

Analysis

3.1 Overview

The procedure of obtaining the missing-mass spectrum of the ^{4}He(K^-, π^-)X reaction is explained. In Sects. 3.2 and 3.3, the momentum of the K^- beam and the outgoing π^- are analyzed, respectively. Then, in Sect. 3.4, the reaction vertex is calculated to select events occurred in the target cell. Finally, the missing-mass of the ^{4}He(K^-, π^-)X reaction is calculated in Sect. 3.6. Using the missing-mass peak of the Σ^+ hyperon and the ground state of $^4_\Lambda$He, momenta measured by spectrometers is calibrated in Sect. 3.5.2. And then, to convert to the cross section from counts, detector efficiencies and normalization factors are estimated in Sect. 3.7. To evaluate this experimental set up, we obtain the production cross section for Σ^+ hyperon in Sect. 3.8.

3.2 K^- beam analysis

In this analysis, K^- beam events were selected by the time-of-flight method. A momentum of kaon is analyzed using the QQDQQ system with trackers.

3.2.1 Beam particle identification

Using the Time-Of-Flight for Beam particles ($BTOF$) between BH1 and BH2, kaon is distinguished from pion. The peak of $BTOF$ came to zero when a kaon was selected (see Fig. 3.1). Pion events locate at $BTOF = 1.8$ ns when the beam momentum is 1.5 GeV/c. To reject the pion contamination, events in -0.9 $< BTOF <$ 0.9 were selected.

3.2.2 Momentum reconstruction of kaon

BFT analysis

Since BFT has only x and x' layers, only a x position is obtained using a hit fiber position of BFT. Because a count rate is higher at upstream of QQDQQ magnets than that at the downstream. A tight timing cut, $-5 < time$ [ns] < 5, is applied to reduce
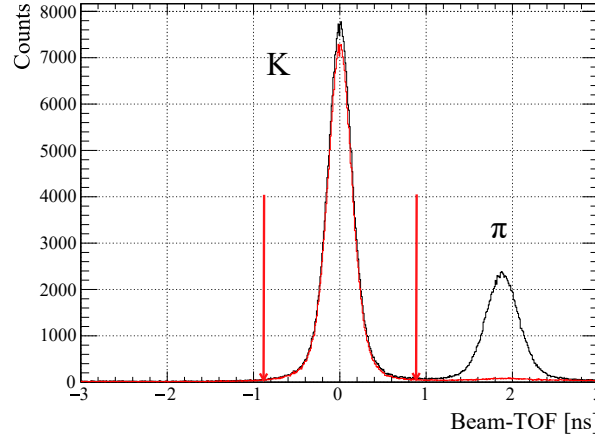
Figure 3.1: The BTOF distribution after TDC calibration and slewing correction. Black line shows $BH1 \times BH2$ trigger events. Red line shows that for Kin trigger events.

accidental hit as shown in Fig. 3.2. The clustering is applied in case of both layer hits. In the clustering, averaged *time* and *x*-position are calculated.
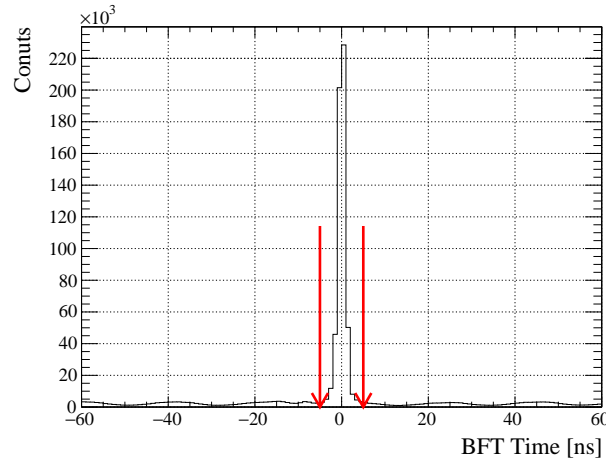
Figure 3.2: The time distribution of BFT.

BcOut tracking

There are BC3 and BC4 just behind QQDQQ magnets. The procedure for the local straight tracking is called the *BcOut* tracking. The average detection efficiency of the single layer for kaon is 99.8%, which is enough to measure kaons. The hit position can be converted from the measured drift time.

Three-dimensional particle trajectories at the exit of the QQDQQ magnets are reconstructed using hit positions on each layer with the least squares method. The χ^2 is

defined as

$$\chi^2 \;=\; \frac{1}{n-4} \sum_{i=1}^{n} H_i \left(\frac{X_i - f\left(z_i\right)}{\sigma_i} \right)^2 \tag{3.1}$$

$$n \;=\; \sum_{i=1}^{12} H_i \tag{3.2}$$

$$H_i \;=\; \begin{cases} 1 & \text{if i-th plane has a hit} \\ 0 & \text{if i-th plane has no hit} \end{cases} \tag{3.3}$$

where Xi is a local hit position in ith plane represented and $f(z_i)$ is a position calculated from a tracking result at the plane i. The local straight track is expressed by four track parameters, i.e. $x0, y0, u0, v0$, which respectively denote x and y position at the origin of a local tracking coordinate and its slope, dx/dz and dy/dz. Tracks are accepted in which at least eight layer hits participate with the χ^2 value of less than 8. The tracking efficiency is 99.2%.
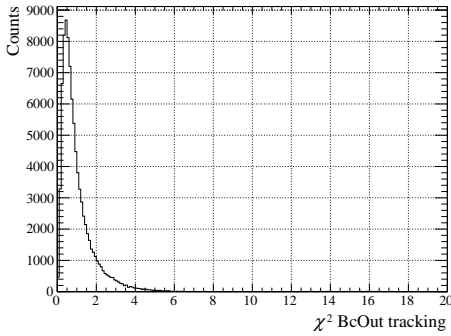
Figure 3.3: The χ^2 distribution of the BcOut Tracking.
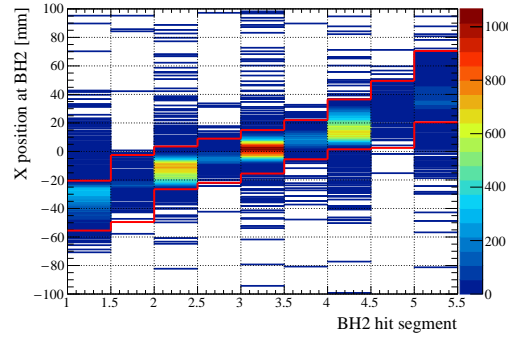
Figure 3.4: The correlation between a hit segment of BH2 and a reconstructed position of BcOut. Events out of black lines are rejected.

To find out single true track, the matching between a hit segment of BH2 and a reconstructed position of BcOut tracking at the BH2 position is checked. Fig. 3.4 shows the correlation between a hit segment of BH2 and a reconstructed position of BcOut. Events in the area surrounded by the red lines in Fig. 3.4 are selected. The efficiency of finding the single true track is 97.5%.

Reconstruction of momentum and trajectory using transport matrix

To reconstruct the beam momentum, the three transport matrix $\vec{M}$ is used. $\vec{M}$ are obtained by the ORBIT program [45].

$$\vec{X_{in}} = M(\vec{X_{out}}, \delta), \tag{3.4}$$

$$\vec{X_{in}} = (x_{in}, y_{in}, \frac{dx_{in}}{dz_{in}}, \frac{dy_{in}}{dz_{in}}) \tag{3.5}$$

$$\vec{X_{out}} = (x_{out}, y_{out}, \frac{dx_{out}}{dz_{out}}, \frac{dy_{out}}{dz_{out}}), \tag{3.6}$$

where δ is the fractional momentum deviation from the central momentum p_0. The three-dimensional particle trajectories $\vec{X_{out}}$ at the exit of the QQDQQ magnets are obtained from the BcOut tracking. x_{in} is obtained from the BFT analysis. In addition, the three-dimensional particle trajectories $\vec{X_{in}}$ at the entrance of the QQDQQ magnets can be obtained. Figure 3.5 shows reconstructed momentum distribution. The measured momentum is denoted as $p = p_0(1+\delta)$. The obtained momentum deviation is 0.02 MeV/c at 1.5 GeV/c.
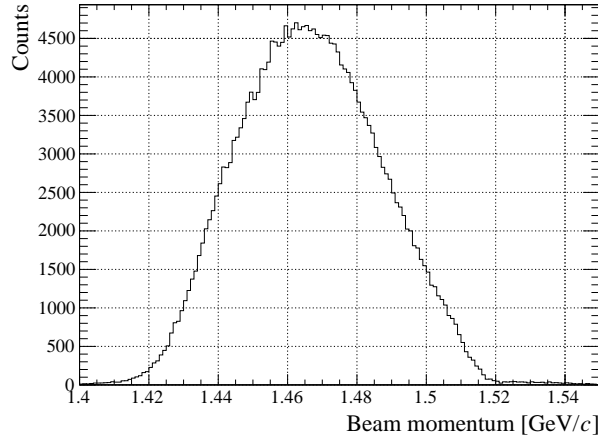
Figure 3.5: The reconstructed beam-momentum distribution for the physics run with the beam momentum of 1.5 GeV/c.

To find out single true track, the matching between a hit segment of BH1 and a reconstructed position of K1.8 tracking at the BH1 position is checked as shown in Fig. 3.6. Events in the area surrounded by the red lines are accepted. After the matching analysis, the tracking efficiency and the efficiency of finding the single true track are 99.1% and 97.5%, respectively.

3.3   Outgoing π^- analysis

The four-momentum of the outgoing particle is obtained using the SKS system. The trajectories at the entrance and the exit of the SKS magnet are measured using SDC1,
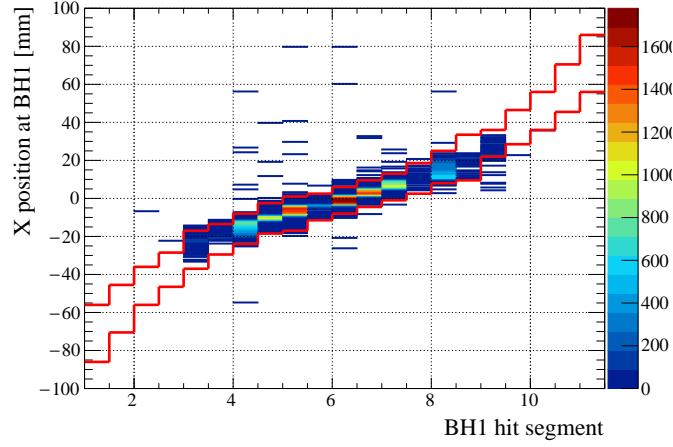
Figure 3.6: The correlation between a BH1 hit segment and a position from the K1.8 tracking. Events out of Red lines are rejected.

SDC2, SDC3 and SDC4 as explained in Sects. 3.3.1 and 3.3.1. After these tracking as the pre-tracking, the momenta of outgoing particles are reconstructed by the Runge-Kutta method as explained in Sect. 3.3.1.

Not only scattered pions but also beam kaons are detected by the SKS system. Outgoing π^- can be distinguished from kaon by checking the mass-square of an outgoing particle as explained in Sect. 3.3.2. A contamination of outgoing kaons are negligibly small. In this analysis, the mass-square cut is not applied.

3.3.1 Momentum reconstruction of pion

SdcIn jpre-tracking

Analysis procedure of the SdcIn pre-tracking is also similar to that of the BcOut tracking described in 3.2.2. The average detection efficiency of all 10 layers is 97.5%, which is large enough to measure pions. The three-dimensional particle trajectories at the entrance of the SKS magnet are reconstructed using the same least squares method as the BcOut tracking in Eq. 3.2. The χ^2 distribution of the SdcIn pre-tracking is shown in Fig. 3.7. Tracks in which at least eight hits participate with the reduced χ^2 value of less than 30 are accepted. The tracking efficiency is 99.0 %.

SdcOut pre-tracking

Analysis procedure of the SdcOut pre-tracking is also similar to that of the BcOut tracking described in 3.2.2. The averaged detection efficiency is 97.4%. The χ^2 distribution of the SdcOut pre-tracking is shown in Fig. 3.8. Tracks in which at least nine hits participate with the reduced χ^2 value of less than 30 are accepted. The tracking efficiency is 96.6%.
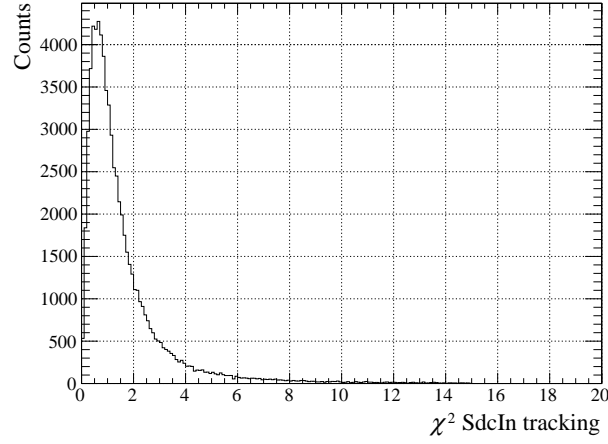
Figure 3.7: The χ^2 distribution of the SdcIn pre-tracking.
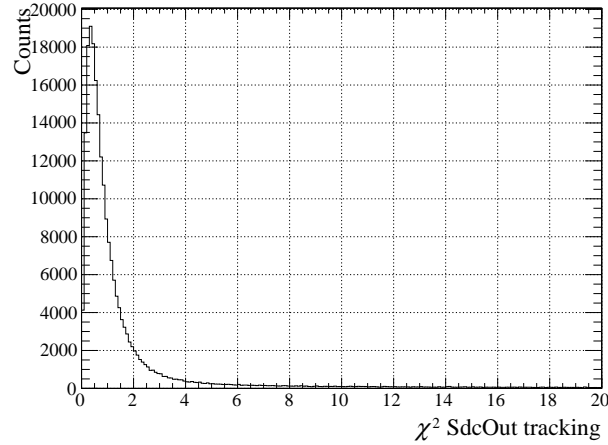
Figure 3.8: The χ^2 distribution of the SdcOut pre-tracking.

Combined tracking with the Runge-Kutta method (SKS tracking)

To reconstruct the momentum of the scattered particle, combined tracking with the Runge-Kutta method [46] is called the *BcOut* tracking. The magnetic field is calculated by ANSYS [47].

The χ^2 distribution of the SKS tracking is shown in Fig. 3.9. Tracks in which at least nine hits participate with the reduced χ^2 value of less than 30 are accepted. The tracking efficiency is $96.23 \pm 0.12\%$.
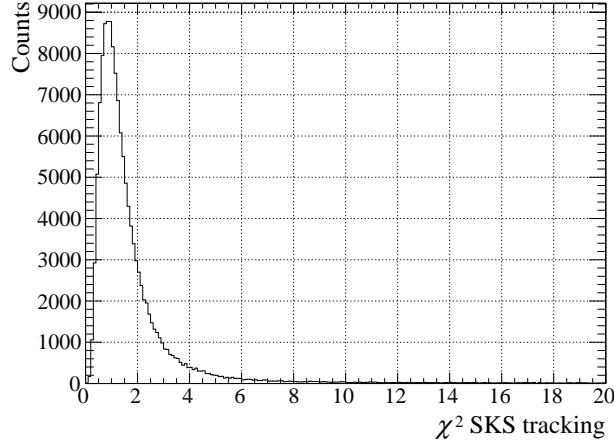
Figure 3.9: The χ^2 distribution of the SKS tracking.

3.3.2 Scattered particle identification

To identify scattered particles, the mass-square M^2 is calculated as

$$M^2 = \left(\frac{p}{\beta}\right)^2 \left(1 - \beta^2\right) \tag{3.7}$$

$$\beta = \frac{L}{ct}, \tag{3.8}$$

where, p is the momentum reconstructed by the SKS system. β is the velocity using the flight path length L by the SKS system and the time-of-flight t between BH2 and TOF wall.

Figure 3.10 shows the obtained mass-square distribution. In this experiment, π^- and K^- can be detected. Since the beam kaon has the momentum considerably higher than that of π^-, the beam kaon through/scattered events are located in lower region of missing-mass of the (K^-, π^-) reaction as shown in Fig. 3.11. Since there is almost no background in missing-mass the region of interest ($M > 3990$ MeV/c^2), the mass-square cut is not applied in this analysis.

3.4 Vertex reconstruction

The reaction vertex can be calculated with momenta of the beam K^- and the ejected π^-.

The x-, y-, and z-vertex distribution are shown in Fig. 3.12 (a), (b), and(c), respectively. The reaction vertex is the center point of the closest distance vector. The vertex cut corresponding to the size of target is applied. The closest distance is that between vectors of the K^- beam and scattered π^-. The distribution of the closest distance is shown in Fig. 3.12 (d). The closest distance smaller than 30 mm is accepted. The cut efficiency of the closest distance is 99.0%.
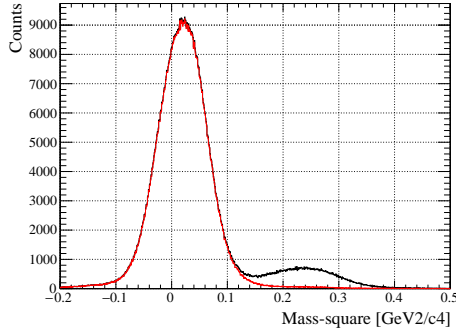
Figure 3.10: The mass-square distribution. Black line shows (K, π) trigger events. Red line shows events in the region of interest of particle momentum.
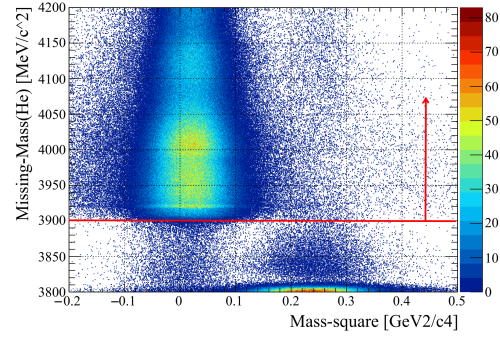
Figure 3.11: The correlation between mass-square and the missing-mass of the $^4\mathrm{He}(K^-, \pi^- X)$ reaction. Red arrow shows events in accepted region of interest.
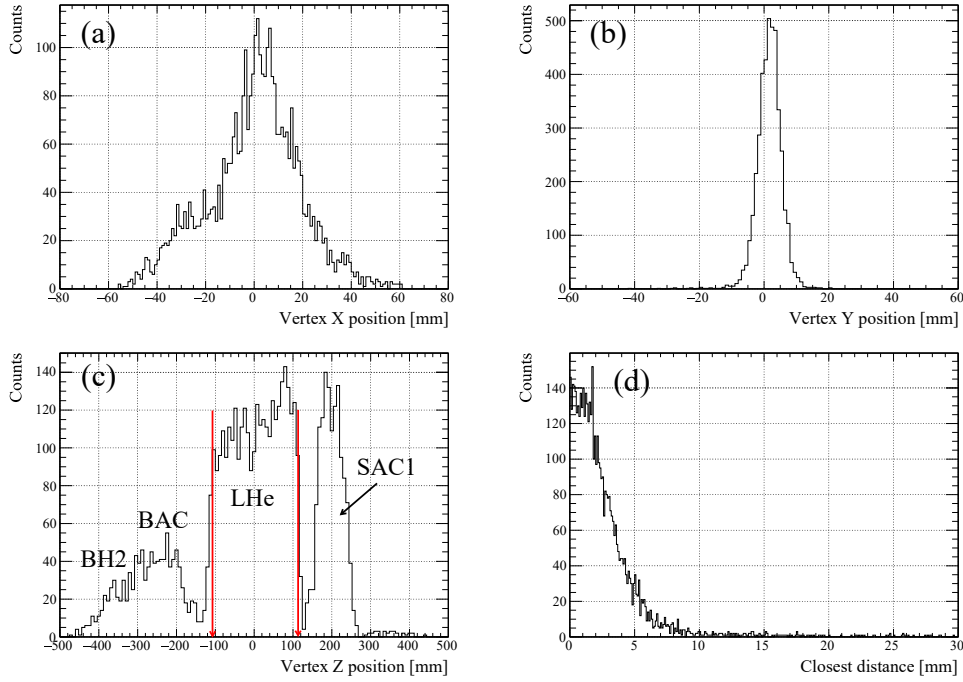
Figure 3.12: (a), (b), and (c) the x, y, and z-vertex distribution, respectively. (d) the closest distance distribution.

3.5   Momentum calibration

Reconstructed momenta from the K1.8 and the SKS spectrometers are known to have offset values. In addition, momenta from the SKS tracking are shifted depending on the path in the SKS. The momenta are calibrated using a beam-through analysis and a missing-mass analysis.

3.5.1 Energy-loss correction

Energies decrease when particle pass through materials. The energy-loss was estimated using the Bethe-Bloch's equation as

$$\frac{d\bar{E}}{dx} = Kz^2 \frac{Z}{A} \frac{1}{\beta} \left[\frac{1}{2} \ln \frac{2m_e c^2 \beta^2 \gamma^2 W_{max}}{I} - \beta^2 - \frac{\delta(\beta\gamma)}{2} \right]. \tag{3.9}$$

This calculation is applied for every material along the particle trajectories. The list of the materials in this experiment is shown in Table 3.1. The most thick material is the helium target. Aerogel Čerenkov Counter (BAC and SAC1) is the next. The energy

Table 3.1: The list of the materials

	thickness [g/cm^2]	energy-loss [MeV]
BH2	0.83	1.6
BAC	2.6	3.2
Mylar	0.03	0.05
SUS	0.08	0.1
Al	0.05	0.09
G10	0.09	0.15
SAC1	1.4	1.7
LHe	2.7	5.5
CH$_2$	2.9	6.3

loss is used. Peak positions of the momentum difference distribution should be shifted from the averaged value. The shape of the distribution also is simulated by using the Monte-Carlo method. At that time, the Landau distribution for pion and the Vavilov distribution are used considering the detector resolutions. The shift values are about 1.5 MeV/c.

3.5.2 Calibration of the K1.8 beam-line and SKS spectrometer systems

True momenta p'_{K18} and p'_{SKS} in the K1.8 beam line and the SKS spectrometer system are written as

$$p'_{K18} = p_{K18} - g(p_{K18}) \tag{3.10}$$
$$p'_{SKS} = p_{SKS} - f(p_{SKS}), \tag{3.11}$$

where p_{K18} and p_{SKS} are measured momenta, $g(p_{K18})$ and $f(p_{SKS})$ are calibration functions for the K18 beam line spectrometer and the SKS system, respectively. Polynomial functions are assumed for the calibration functions [48]. $g(p_{K18})$ and $f(p_{SKS})$ are defined as a linear function for the K1.8 beam line spectrometer and a second-order function for the SKS system as follows.

$$g(p_{K18}) = \alpha p_{K18} + \beta \tag{3.12}$$
$$f(p_{SKS}) = A p_{SKS}^2 + B p_{SKS} + C \tag{3.13}$$

To calibrate these spectrometers, the beam-through data were taken at four different energies. When $g(p_{K18})$ is given, $f(p_{SKS})$ can be calculated using the beam-through data. Since $p'_{K18} = p'_{SKS}$, the measured momentum difference Δp between the K1.8 and SKS system is defined as

$$\Delta p = p_{SKS} - p_{K18} \tag{3.14}$$
$$= f(x) - g(x) \tag{3.15}$$
$$= h(p). \tag{3.16}$$

The momentum difference Δp distribution is shown in Fig. 3.13. As an example of the $g(p_{K18}) = 0$, four points of beam momenta are shown in Fig. 3.14. Fitting these points, the calibration function $f(p_{SKS})$ can be obtained. The calibration function $g(p_{K18})$ for
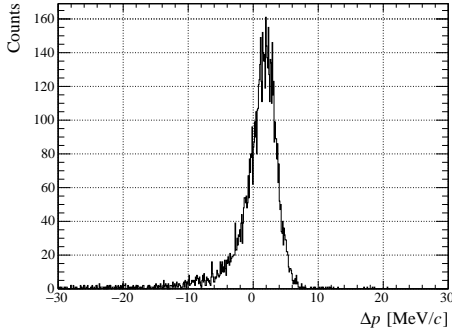
Figure 3.13: The calibrated distribution of the momentum difference $\Delta p = p_{SKS} - p_{K18}$ at the beam momentum of 1.5 GeV/c.
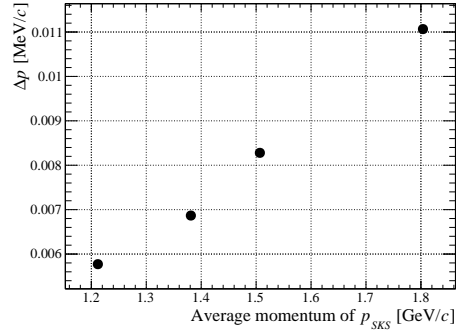
Figure 3.14: The momentum difference Δp depending on momenta p_{SKS} with $g(p_{K18}) = 0$.

the K18 spectrometer has to be determined. To determine α and β, the peak positions of the missing-mass distributions for Σ^+ and the ground-state of $^4_\Lambda$He are used. $\alpha = 1.36$ and $\beta = 45.4$ are obtained. Peak positions of the missing-mass distribution also should be shifted from the reference value taken from the past emulsion experiment [49]. For the ground state of $^4_\Lambda$He, the shift value is 0.88 MeV.

3.6   Missing-mass analysis

The four-momentum vector of the reaction product P_X is defined as

$$P_X = P_K + P_{\text{tgt}} - P_\pi, \tag{3.17}$$

where P_K, P_{tgt}, and P_π are the four-momentum vectors of the beam K, the ^{4}He target (at rest), and the scattered π. Then, the missing-mass M_X of the ^{4}He$(K^-, \pi^-)X$ reaction is calculated using

$$M_X = \sqrt{\left(E_K + M_{tgt} - E_\pi\right)^2 - \left(p_K^2 + p_\pi^2 - 2p_K p_\pi \cos\theta_{Lab}\right)}, \tag{3.18}$$

where E_K, E_π, p_K and p_π are the energies the momenta of pion and kaon, respectively. M_{tgt} stands for a target mass and θ_{Lab} is the scattering angle of the pion. The distribution of the missing-mass of the ${}^4\text{He}(K^-,\pi^-)X$ reaction at $\theta_{Lab} = 2\text{-}14$ degrees is shown in Fig. 3.15. Though hypernuclear productions and hyperon quasi-free process can be seen in the spectrum, the background distribution resides in all range of the missing-mass. Main background contribution is the $K^- \to \pi^-\pi^0$ decay event. To compare the experimental result with the theoretical calculation for the ${}^4\text{He}(K^-,\pi^-)X$ reaction, the background should be subtracted. Since the background distribution depends on both the momentum and the scattering angle for the scattered particle, the spectrum is distorted by the analysis cut of $K^- \to \pi^-\pi^0$ decay. To deal with that, the distribution of $K^- \to \pi^-\pi^0$ background is estimated using the Geant4 package and is subtracted as explained in Sect. 4.

Figure 3.15: The distribution of the missing-mass of the ${}^4\text{He}(K^-,\pi^-)X$ reaction at $\theta_{Lab} = 2\text{-}14$ degrees.

3.7 Cross section calculation

To calculate the cross section of the missing-mass distribution, the acceptance of the SKS system and the efficiencies of the detectors are considered. The differential cross

section can be written as follows.

$$\frac{d\sigma}{d\Omega} = \frac{N_{scat}}{N_{tgt}N_{beam}\epsilon_{det}f_{absK}f_{abs\pi}f_{dec\pi}f_{ovk}\Delta\Omega} \tag{3.19}$$

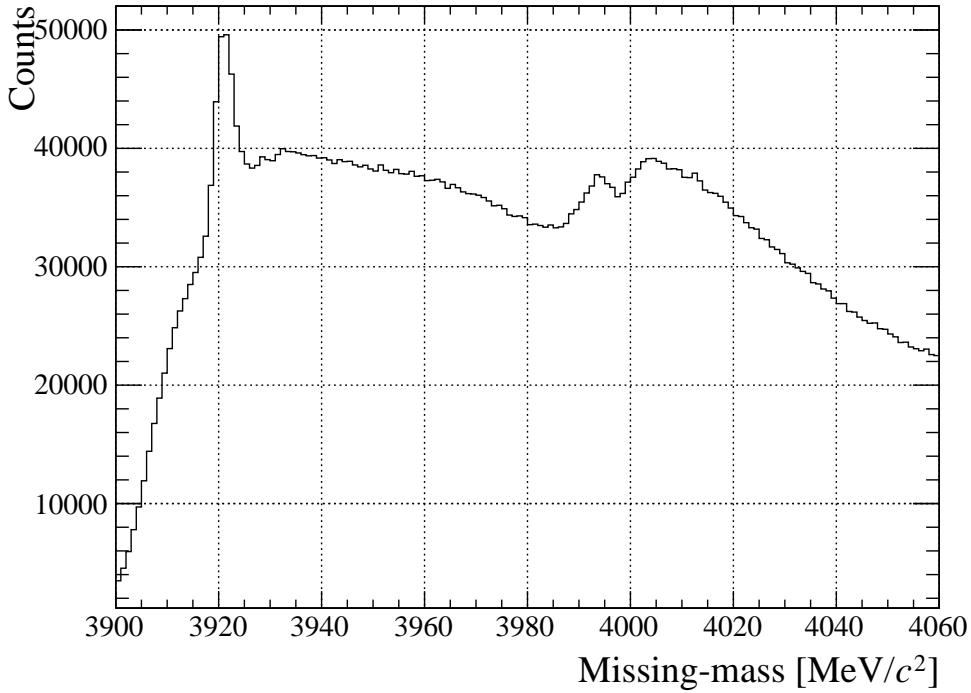Here, N_{scat} and N_{tgt} are the numbers of scattered pions and nuclei in a target. N_{beam} is the number of the beam track in $BH1 \times BH2$ trigger multiplied by its pre-scale factor of 1.28×10^4. $\Delta\Omega$ is the solid angle of the SKS spectrometer. f_{absK} and $f_{abs\pi}$ are the absorption factors for kaon and pion, respectively, and are evaluated using Geant4 simulation. f_{dec} is the π^- decay factor and is explained in Sect. 3.7.3. The total detector efficiency ϵ_{det} is

$$\epsilon_{det} = \epsilon_{SAC}\epsilon_{SdcIn}\epsilon_{SdcOut}\epsilon_{SKS}\epsilon_{vtx}\epsilon_{cdist}. \tag{3.20}$$

These efficiencies are summarized in Table 3.2. The acceptance $\Delta\Omega$, the oversuppression ratio f_{ovk} table and π^- decay factor are applied event by event.

Table 3.2: The list of efficiencies and factors.

Name	Efficiency [%]
ϵ_{SAC}	99.1 ± 0.2
ϵ_{SdcIn}	99.0 ± 0.04
ϵ_{SdcOut}	96.7 ± 0.04
ϵ_{SKS}	96.2 ± 0.1
ϵ_{cdist}	100
f_{abs}	90.6 ± 0.8

3.7.1   Acceptance of SKS

The acceptance of SKS is calculated by Monte Carlo simulation using Geant4. The realistic SKS system and beam profile are reproduced in the simulation. The effective solid angle $\Delta\Omega(p,\theta)$ is defined as

$$\Delta\Omega(p,\theta) = 2\pi \int_{\theta-\frac{1}{2}\Delta\theta}^{\theta+\frac{1}{2}\Delta\theta} \frac{N_a(p,\theta)}{N_g(p,\theta)}d\cos\theta, \tag{3.21}$$

where p and θ are the generated momentum of scattered π^- and scattering polar angle, respectively. N_a and N_g are the number of accepted and generated π^- at each momentum and angle estimated by the simulation, respectively. The mesh size in the simulation is $\Delta\theta = 0.1$ degrees and $\Delta M = 1$ MeV/c^2. The table of the $\frac{N_a}{N_g}$ ratio as the acceptance table of the SKS system is called. The acceptance tables are shown in Fig. 3.17. The acceptance for the scattering events to the left of the entrance of the SKS magnet in 9–14 degrees range may rapidly change as shown in Fig. 3.17 (a) and thus have a large ambiguity. Therefore, only the scattering event to the right is analyzed in this angular range. The acceptance table as shown in Fig. 3.17 (c) was average of (a) and (b), and was applied in each event.
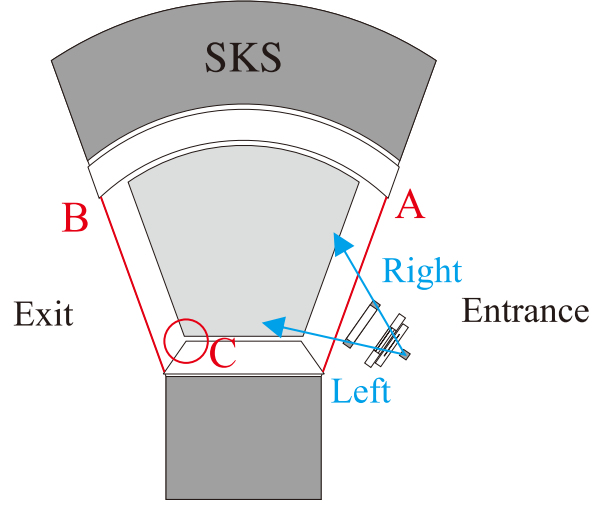
Figure 3.16: The blue arrow shows the definition of the scattering to the left and the right in horizontal plane, respectively [48].

Figure 3.17: The acceptance table of the SKS system. (a) and (b) show the tables scattering to the left and the right in horizontal plane, respectively. (c) shows the averaged table.

3.7.2   Oversuppression by SMF

As mentioned in Sect. 2.4.2, SMF is introduced to reject the muons from the $K^- \to \mu\nu$ decay. SMF can clearly reject $K^- \to \mu^-\nu$ decay events as shown in Fig. 3.18. However, some fraction of π^- is killed by SMF. This is called an oversuppression. The oversuppression ratio is estimated by Monte Carlo simulation using Geant4. The hadron interaction and the particle-transportation were taken into account in the simulation. Electromagnetic interaction and decay are were ignored. π^- of $\beta > 1/$ index on an SMF segment is regarded to the oversuppression. The oversuppression table is shown in Fig. 3.19. The oversuppression ratio varies from 2 to 30 %.

Figure 3.18: The correlation between measured momenta and scattering angles. (a) shows events with SMF veto off. (b) shows events with SMF veto on.

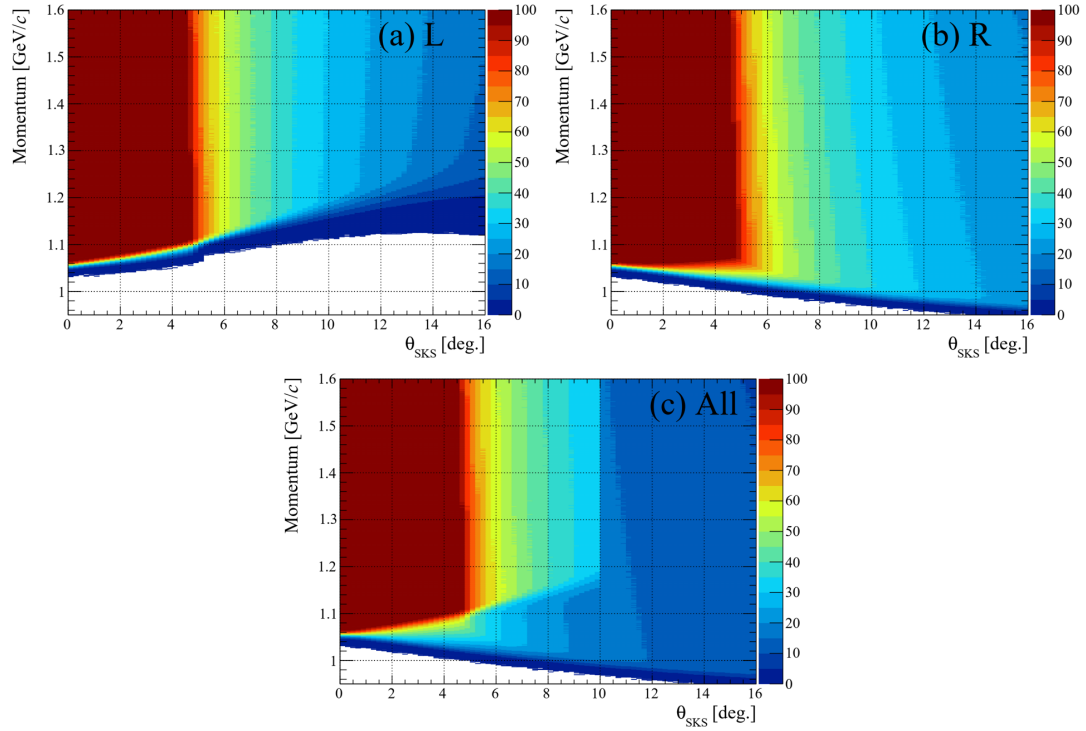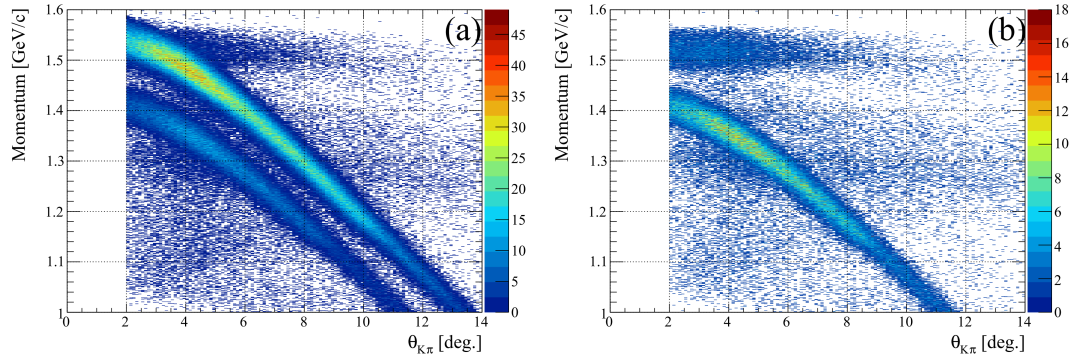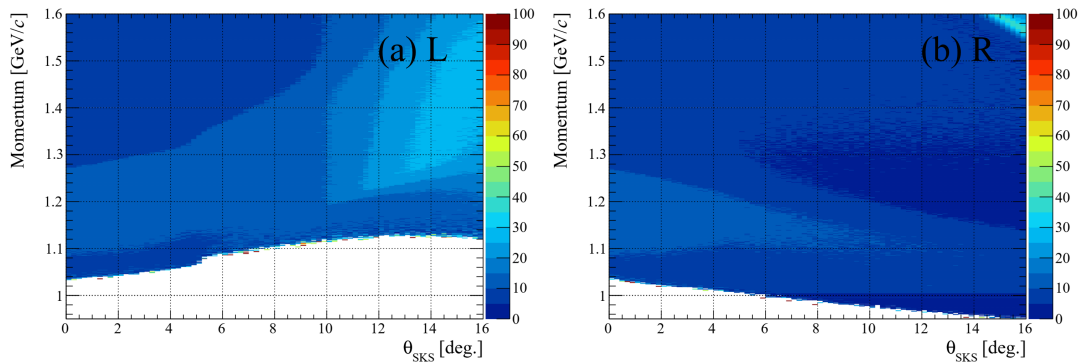Figure 3.19: The oversuppression table of SMF. (a) and (b) show the tables scattering to the left and the right in horizontal plane, respectively.

3.7.3 Decay factor of π^-

(K, π) trigger can not record data of $\pi^- \to \mu^- \nu$ decays since they are killed by SMF. Its decay rate have to be estimated. The decay factor f_{decay} is written as

$$f_{decay} = \exp(-\frac{L}{\beta\gamma c\tau}), \tag{3.22}$$

where L is a track length of a scattered particle measured by the SKS system. The value of $c\tau$ for π^- is 7.8 m. The factor varies from 2 to 8% depending on L.

3.7.4 Z-vertex cut efficiency

To eliminate contamination from the materials other than the target (BAC, SAC1, and the windows of the target cell), events with z-vertex within the target length are selected. Figures 3.20 and 3.21 show the z-vertex spectra in every 1 degree. The z-vertex resolution gets worse as the scattering angle decreases. Therefore, events of the reaction at the LHe target are lost when the z-vertex cut position is fixed. The z-vertex cut efficiency is estimated by a fitting. Figures 3.20 and 3.21 show the z-vertex distributions with the fitting functions. Red line shows a total fitting function. In the fitting function, all materials are considered as shown by dashed lines. The fitting function was made by folding the box-shape material distribution along the beam trajectory with the z-vertex resolution. The z-vertex cut efficiency depends on the scattering angle as shown in Fig. 3.22. The efficiency error is came from changing of the fitting range. A function of the z-vertex cut efficiency is obtained using a probability density function. The efficiency is applied event by event. The error of the z-vertex efficiency is calculated by using changing of the cross section every the missing-mass bin.

3.8 Production cross section of Σ^+ hyperon

The Σ^+ production cross section is obtained via the (K^-, π^-) reaction using a CH$_2$ target to calibrate momenta of both the spectrometer system. A thickness of the CH$_2$ target is 3 cm. In the Σ^+ production analysis, the z-vertex cut condition is different from the ^{4}He target run. In addition, the vertex resolution gets worse depending on the scattering angle. The cut condition does not cut events from the reaction. The number of total beams is about 10^8.

The cross section is 0.59 ± 0.01 mb/sr in the angular range of $\theta_{\mathrm{Lab}} = 2$-$14°$. The angular dependence of the production cross section via the $p(K^-, \pi^-)\Sigma^+$ reaction is obtained as shown in Fig. 3.24. Filled circles show this work. The errors are small because of the statistics. Open circles show the result of the previous emulsion experiment [50]. This result is in good agreement with the result of the past emulsion experiment.
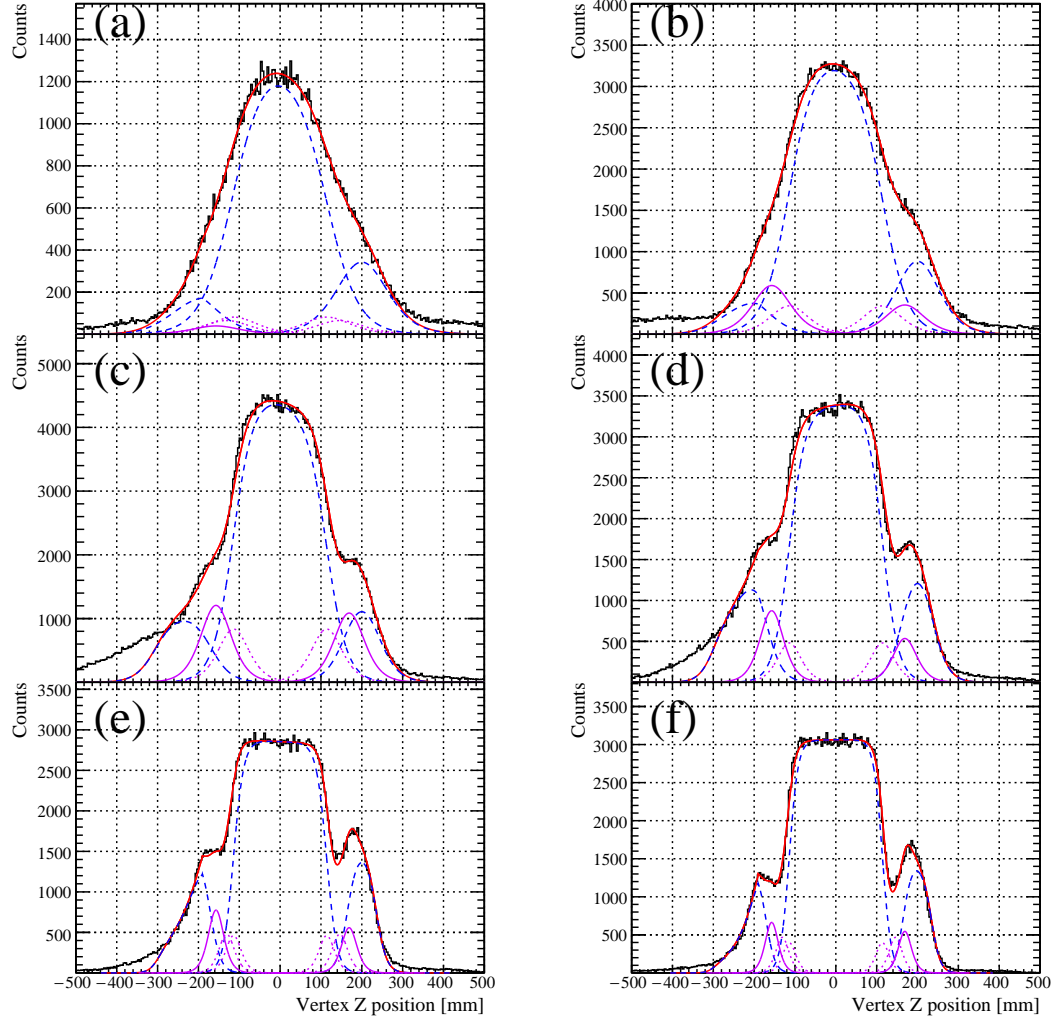
Figure 3.20: The Z-vertex distribution of the physics run. (a)-(f) corresponds to θ = 2-3, 3-4, 4-5, 5-6, 6-7, 7-8 degrees. The red line shows a total fitting function. The blue line shows the contribution of materials (LHe, BAC, SAC1, and the windows of the target cell).
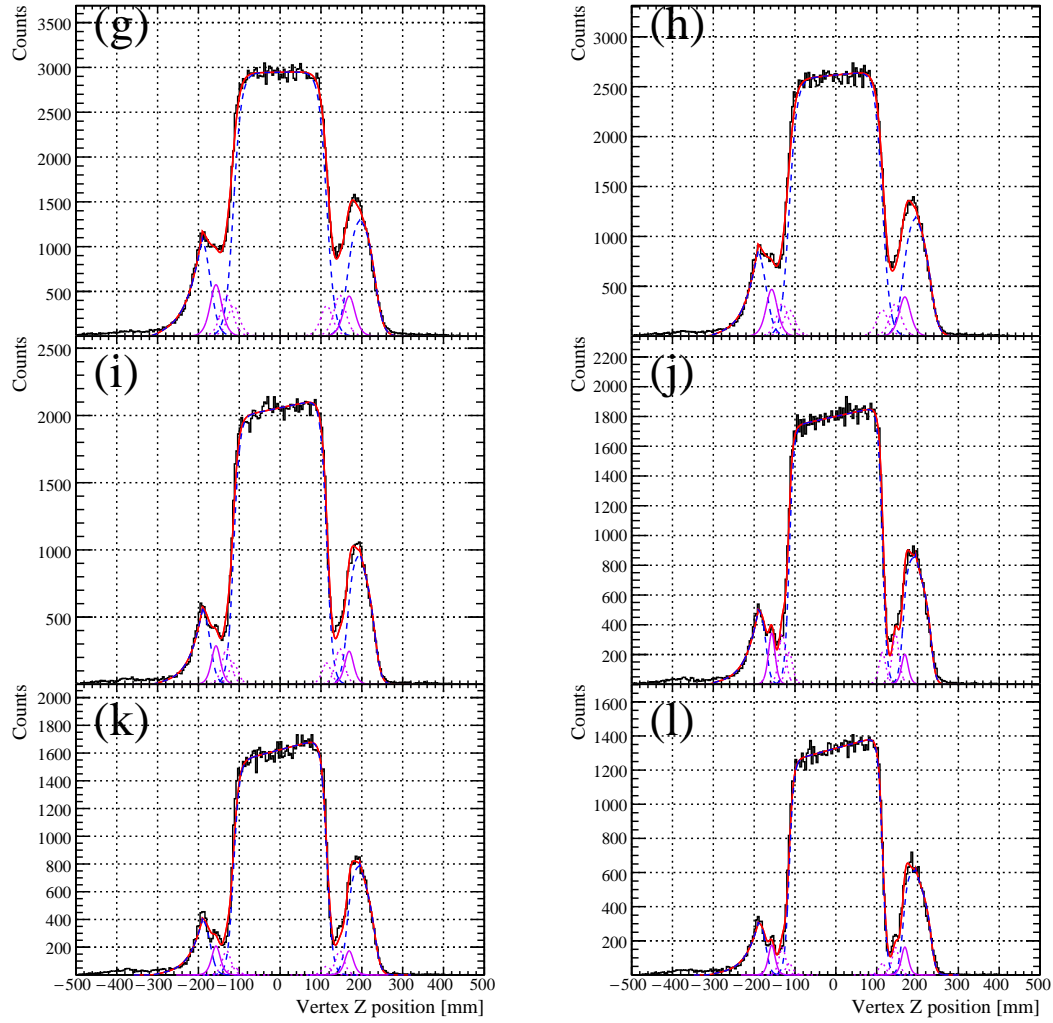
Figure 3.21: The Z-vertex distribution of the physics run. (g)-(l) corresponds to $\theta =$ 8-9, 9-10, 10-11, 11-12, 12-13, 13-14 degrees. The red line shows a total fitting function. The blue line shows the contribution of materials (LHe, BAC, SAC1, and the windows of the target cell).
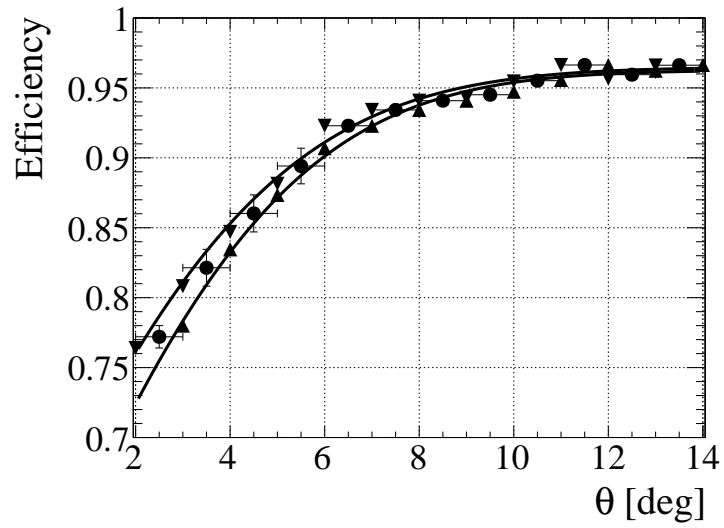
Figure 3.22: The θ dependency of the Z-vertex cut efficiency.
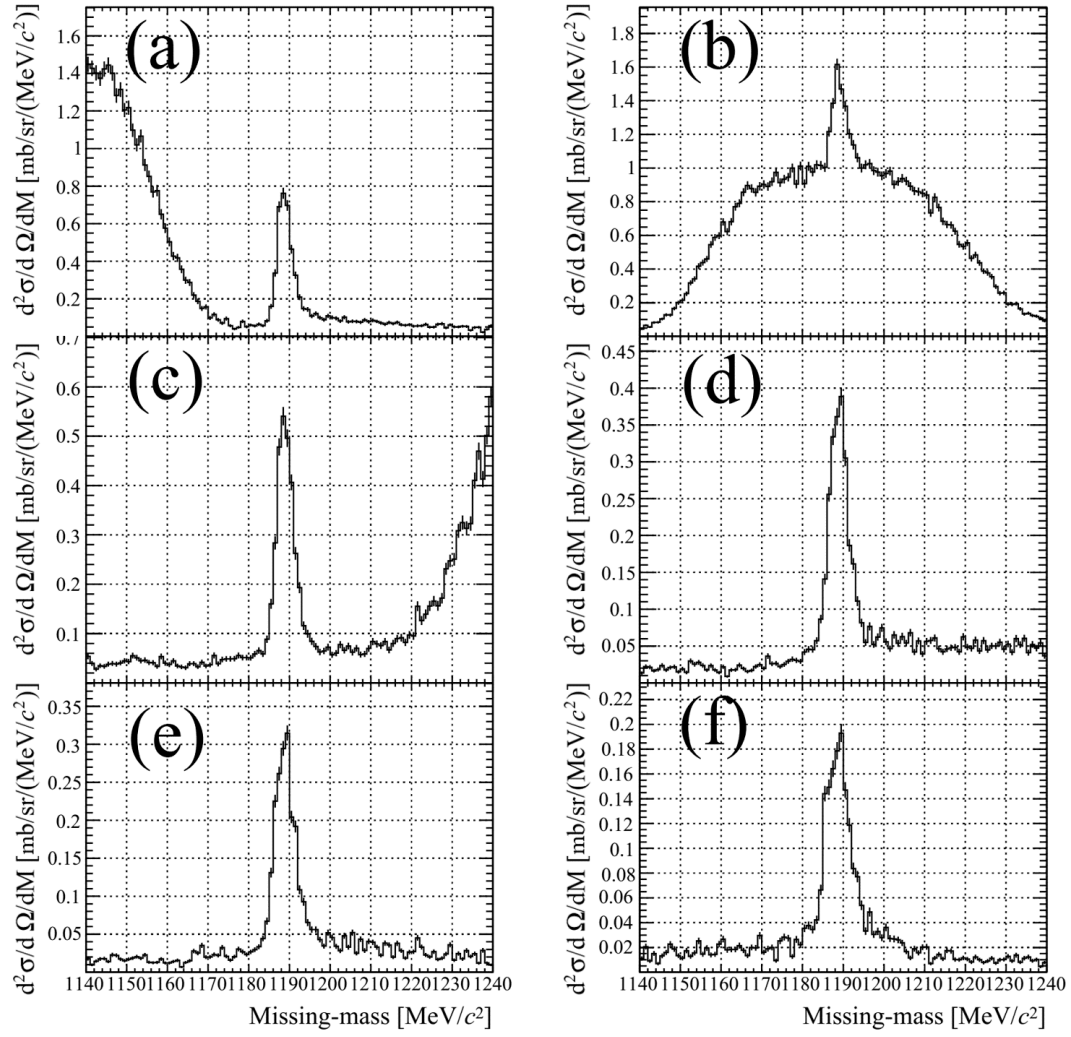
Figure 3.23: The production cross sections of Σ^+. (a)-(f) corresponds to $\theta = $ 2-3.5, 3.5-6.5, 6.5-8, 8-10, 10-12, 12-14 degrees. The main component of background is $K^- \to \pi^- \pi^0$ decay event.
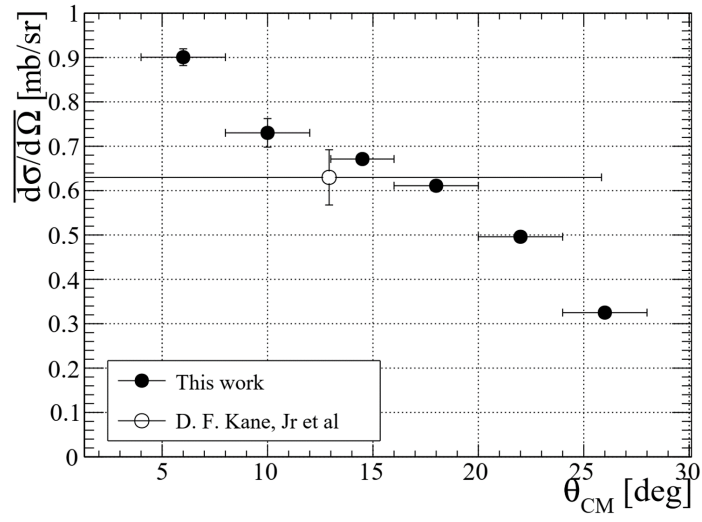
Figure 3.24: The angular dependence of the production cross section of the $p(K^-, \pi^-)\Sigma^+$ reaction. The filled circles show the results of this work. The open circles show the result of the previous emulsion experiment[50].

Chapter 4

Background estimation

4.1   Overview

The main background component for the ^{4}He$(K^-, \pi^-)X$ reaction is π^- events from $K^- \to \pi^- \pi^0$ decay. Since this decay has common outgoing particle π^- and has momentum and scattering angle of similar value, it is difficult to be rejected by the trigger or analytical methods. Therefore, we estimate the background contribution by Monte-Carlo simulation and subtract it from the measured spectrum. The simulation is evaluated using the empty target run, which is explained in Sects. 4.2 and 4.3. The background spectrum is calculated using this Monte-Carlo simulation which is explained in Sect. 4.4.

4.2   Empty target run

In the empty target run, the experimental setup is the same as the physics run except for the liquid ^{4}He. Instead, the target cell was almost empty although ^{4}He gas at ??? Pa remained.

The correlation between the missing-mass X in the $K^- \to \pi^- X$ reaction and the scattering angle θ_{SKS} is shown in Fig. 4.2. To select the $K^- \to \pi^- \pi^0$ decay events, events in 3σ region of the π^0 peak in missing-mass spectrum of the $K^- \to \pi^- X$ reaction are selected. Therefore, using this relation, the decay events can be selected.

The missing-mass spectrum of ^{4}He$(K^-, \pi^-)X$ reaction assuming only the background of ^{4}He run is shown in Fig. 4.3. The structure of the decay spectrum in angular range of $\theta < 8°$ is not leaked into the missing-mass region as shown in Fig. 4.1. In addition, to estimate the background distribution in the ^{4}He run, the horizontal axis is normalized from cross section using a factor of $N_{tgt} \times N_{beam}$.

4.3   Simulation of empty target run

A missing-mass distributions of the empty target run are simulated using Geant4. In the simulation, the realistic SKS system (the SKS magnet, the trackers, SMF, and the target
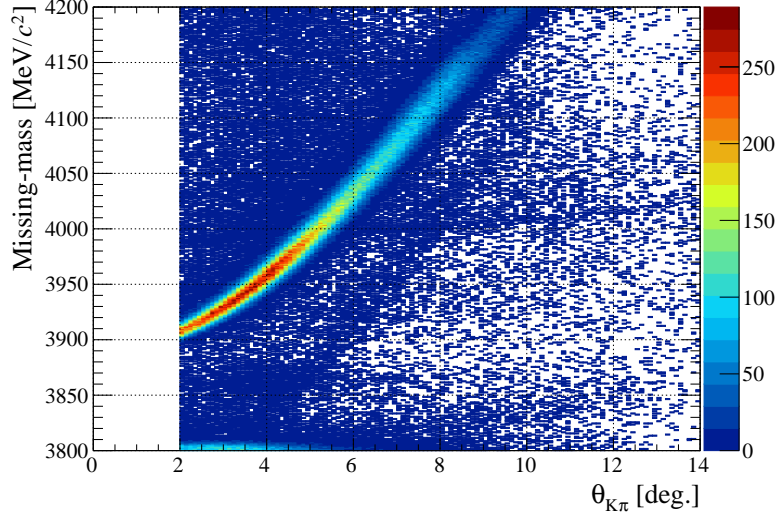
Figure 4.1: The correlation between the missing-mass of the $^{4}\text{He}(K^-, \pi^-)X$ reaction and the scattering angle $\theta_{K\pi}$ for the empty target run. The main component is $K^- \rightarrow \pi^- \pi^0$ decay events.

cell) and beam profile are reproduced. As for the physics processes, electromagnetic and hadron interactions and decay reaction are included. Only the kinematics of the $K^- \rightarrow \pi^- \pi^0$ decay is simulated.

The simulated distribution has to be converted from the number of events to the cross section. To scale the distribution, the relation between the yield of our experiment N including a beam decay background and a double-differential cross section $\frac{d\sigma_{\text{all}}}{dMd\Omega_{\text{lab}}}$ is written as,

$$\Delta N = N_{\text{b}}\, N_{\text{t}}\, \frac{d\sigma_{\text{all}}}{dMd\Omega_{\text{lab}}}\, \Delta M\, \Delta\Omega\, \epsilon_{\text{vertex}}\, \epsilon_{\text{other}}\, f_{\text{acc}}, \tag{4.1}$$

where, M is a missing-mass, N_{b} and N_{t} are the numbers of beams and targets, and ΔM is a missing-mass bin width, and $\Delta\Omega$ is a solid angle, and ϵ_{vertex} is an efficiency of z-vertex cut, and ϵ_{other} is a total efficiency of other contribution (detector efficiency, analysis efficiency, and so on). On the other hand, a decay contribution in the experimental data N_{decay} is written as,

$$\Delta N_{\text{decay}} = N_{\text{b}}\, \frac{d^2 Br}{dMd\Omega_{\text{lab}}}\, \Delta M\, \Delta\Omega\, e^{-\frac{l1}{L}} \left(1 - e^{-\frac{l2}{L}}\right) \epsilon_{\text{other}}\, f_{\text{acc}}, \tag{4.2}$$

where, $\frac{d^2 Br}{dMd\Omega_{lab}}$ is a decay branching ratio of a $K^- \rightarrow \pi^- \pi^0$ background, and L is a decay length of a beam particle ($L = \beta\gamma c\tau$), and $l1$ is a distance between a position where beams were counted and upstream of z-vertex cut, and $l2$ is a width of z-vertex cut.
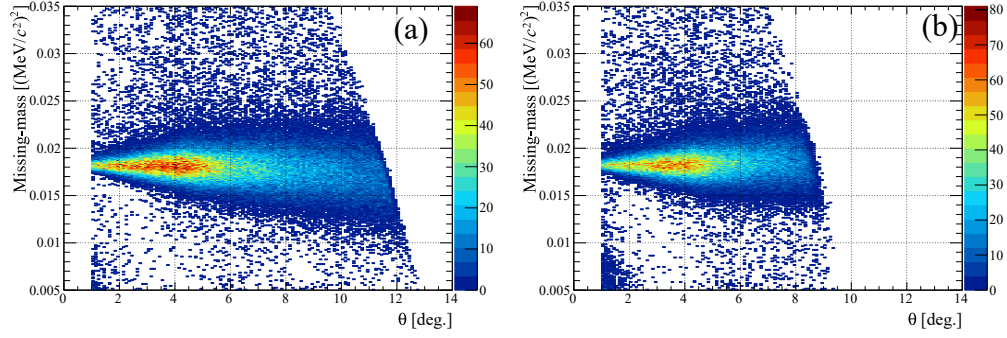
Figure 4.2: The correlation plots between the missing-mass MM_{π^-} and the scattering angle θ_{SKS}. (a) and (b) show the distribution for scattering to the left and right, respectively.
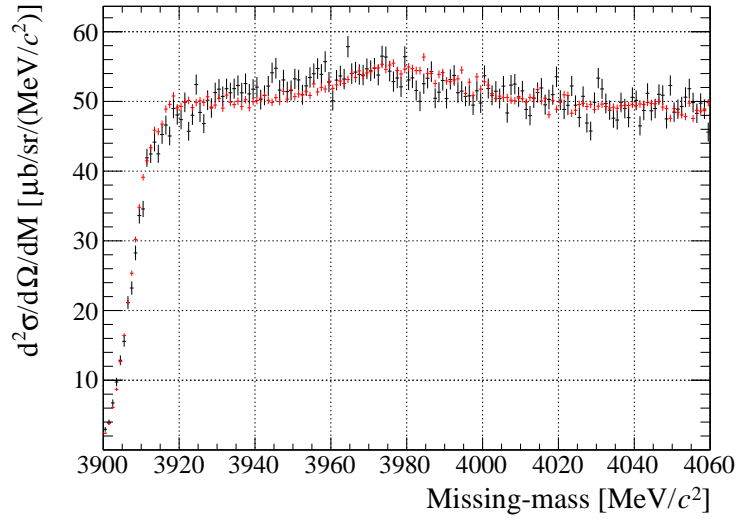
Figure 4.3: The missing-mas spectrum of the $K^- \to \pi^- X$ reaction in the $K^- \to \pi^- \pi^0$ decay events of the empty target run in angular range of 2-14 degrees. Black spectrum shows the experimental data. Red spectrum shows the results of the simulation.
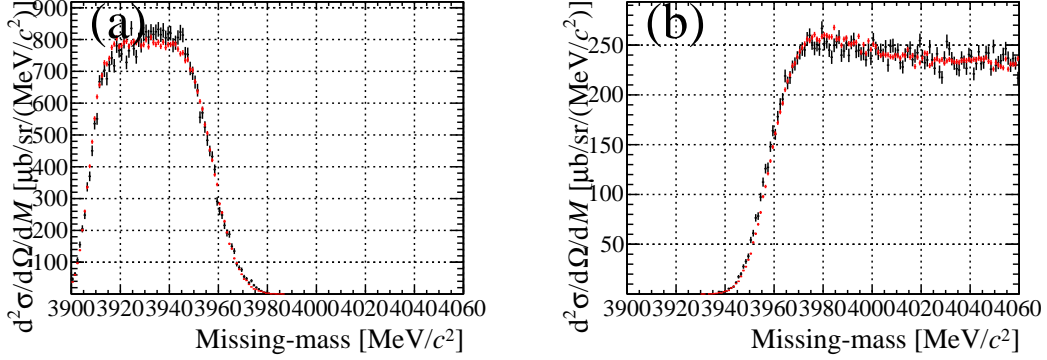
Figure 4.4: The missing-mas spectrum of the $K^- \to \pi^- X$ reaction in the $K^- \to \pi^- \pi^0$ decay events of the empty target run divided into ...Red spectra show the results of the simulation.

$\frac{d\sigma_{\text{all}}}{dMd\Omega_{\text{lab}}}$ is derived from Eq. 4.1 using Eq. 4.2. Then, $\frac{d^2\sigma_{\text{decay}}}{dMd\Omega_{\text{lab}}}$ is written as

$$\frac{d\sigma_{\text{decay}}}{dMd\Omega_{\text{lab}}} = \frac{N_{decay}}{N_b\, N_t\, \Delta M\, \Delta\Omega\, \epsilon_{\text{vertex}}\, \epsilon_{\text{other}}\, f_{\text{acc}}} \tag{4.3}$$

$$= \frac{1}{N_b} \frac{d^2 Br(\text{bg})}{dMd\Omega_{\text{lab}}} \frac{e^{-\frac{l1}{L}}\left(1 - e^{-\frac{l2}{L}}\right)}{\epsilon_{\text{vertex}}}. \tag{4.4}$$

N_{gen} is defined as the number of beam particle decays, and assume that the particle is accepted N_{acc} in a region of ΔM and $\Delta\Omega$. Eq.4.4 can be rewritten as,

$$\frac{d\sigma_{\text{decay}}}{dMd\Omega_{\text{lab}}} = \frac{1}{N_b} \frac{Br(\text{bg})}{\Delta M \Delta\Omega_{\text{lab}}} \frac{N_{\text{acc}}}{N_{\text{gen}}} \frac{e^{-\frac{l1}{L}}\left(1 - e^{-\frac{l2}{L}}\right)}{\epsilon_{\text{vertex}}}. \tag{4.5}$$

The branching ratio of this channel is 20.06 %.

The simulated distribution is compared with the observed data. as shown in Figs. 4.3 and 4.4. The horizontal axis is tuned using factor of 4 %. The simulated spectra are well reproduced.

4.4   BG distribution for $^4\text{He}(K^-, \pi^-)X$ reaction

The simulation of the ^{4}He physics run is made using the same way of the empty target simulation except for the liquid ^{4}He filling. Figure 4.5 shows the simulated missing-mass spectrum of $^4\text{He}(K^-, \pi^-)X$ reaction for the ^{4}He run. The region is not selected because π^0 cut is not applied in case of ^{4}He run. Therefore, the decay spectrum are a large scattering angle. Its yield was order of 10^{-3} in angular range larger then 8 degrees. In the next section, the simulated distribution from the $^4\text{He}(K^-, \pi^-)X$ reaction is subtracted.
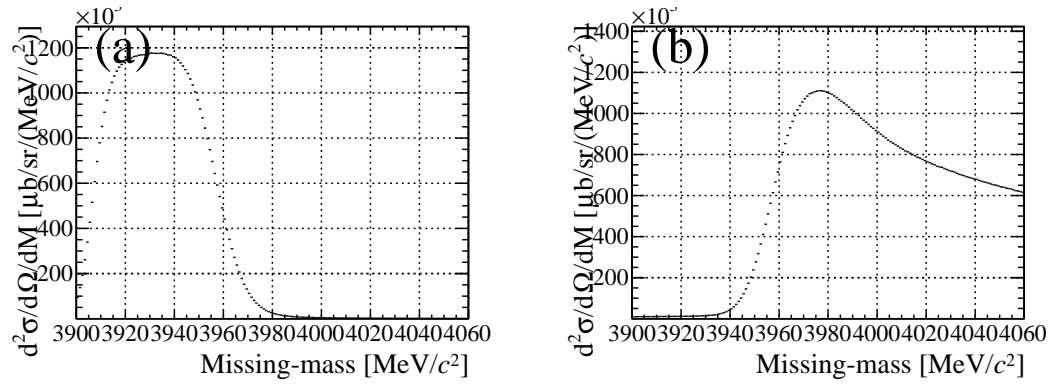
Figure 4.5: The simulated distributions for the ^{4}He run.

Chapter 5

Results and Discussion

The ground and excited states of $^{4}_{\Sigma}$He are discussed based on the obtained missing-mass spectrum of the ^{4}He$(K^{-}, \pi^{-})X$ reaction in this chapter.

5.1 Angular-averaged missing-mass spectrum

The experimental data coveres the angular range of $2° < \theta < 14°$. In this section, the missing-mass spectrum of the ^{4}He$(K^{-}, \pi^{-})X$ reaction over the full angular range is discussed. Figure 5.1 shows the angular-averaged missing-mass spectrum. The vertical axis corresponds to the double-differential cross section in a unit of μb/sr/(MeV/c^2). The holizontal axis corresponds to the missing-mass in a unit of MeV/c^2. The experimental data are shown by the black histogram. The $K^{-} \to \pi^{-}\pi^{0}$ decay background estimated by the Monte Carlo simulation in Sec. 4.4 is shown by the red histogram. The decay background is subtracted from the experimental data. After the subtraction of the decay background, Fig. 5.2 is obtained. The following four components are observed in the subtracted spectrum: The peak structure around 3920 MeV/c^2 corresponds to the bound state of $^{4}_{\Lambda}$He, the peak structure around 3995 MeV/c^2 corresponds to the ground state of $^{4}_{\Sigma}$He, and the significant bump structures in the missing-mass ranges of 3925–3975 MeV/c^2 and 4000–4060 MeV/c^2 come from the Λ and Σ quasi-free production processes, respectively. The excited state of $^{4}_{\Sigma}$He predicted around the missing-mass of 4005 MeV/c^2 by the theoretical calculation is searched in the following sections.

To discuss the Σ hypernucleus, the binding energy B_{Σ} of the Σ hypernucleus is defined as

$$B_{\Sigma} = M\left(3N\Sigma\right) - M_X \tag{5.1}$$

where M_X is the missing-mass in the ^{4}He$(K^{-}, \pi^{-})X$ reaction, $M\left(3N\Sigma\right)$ is the masses of $3N$ and Σ. In the case of the Σ hypernucleus, the two thresholds of the Σ^{+} and Σ^{0} quasi-free production processes should be considered. The threshold of the Σ^{+} quasi-free production process at 3998.31 MeV/c^2 is lower than that of the Σ^{0} quasi-free production process at 4001.05 MeV/c^2. In the present analysis, $B_{\Sigma} = 0$ is defined with the threshold of the Σ^{+} quasi-free production process. The B_{Σ} spectrum is obtained from Fig. 5.2 by using Eq. 5.1 as shown in Fig. 5.3.
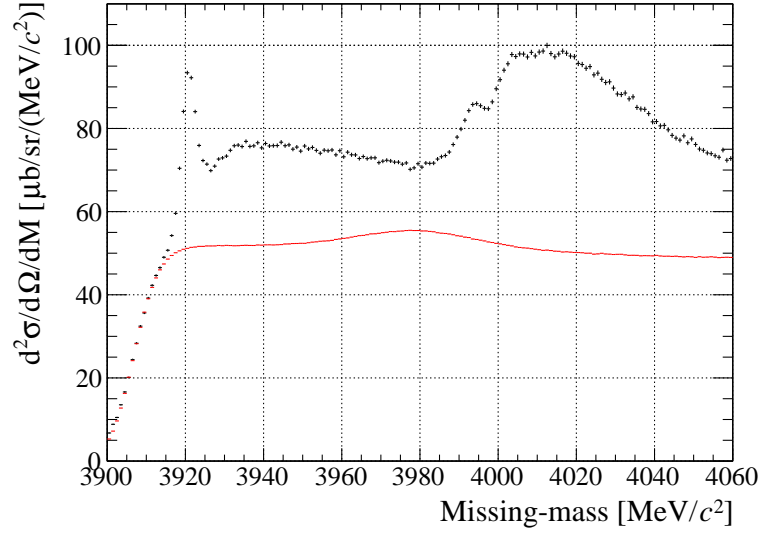
Figure 5.1: Angular-averaged missing-mass spectrum of the ^{4}He$(K^-, \pi^-)X$ reaction. The black histogram shows the measured data. The simulated $K^- \rightarrow \pi^- \pi^0$ background distribution is shown by the red histogram.
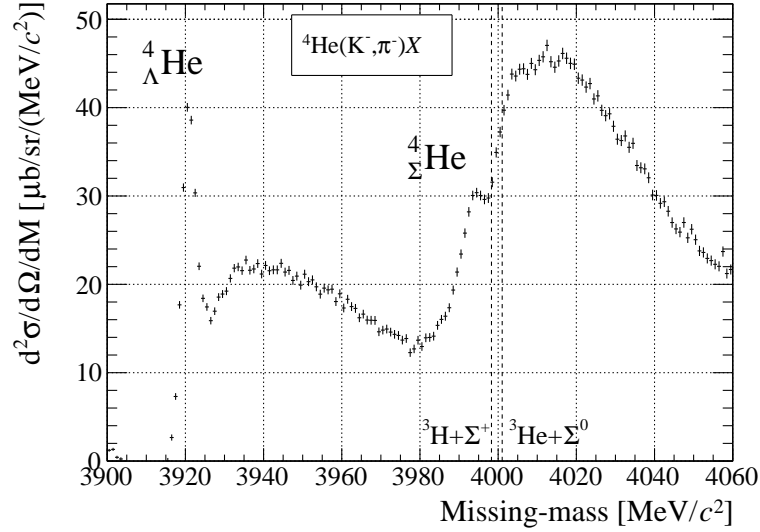
Figure 5.2: Angular-averaged missing-mass spectrum of the ^{4}He$(K^-, \pi^-)X$ reaction after the background subtraction. The dashed lines show the thresholds of the ^{3}H $+\Sigma^+$ and ^{3}He $+\Sigma^0$ quasi-free production process.
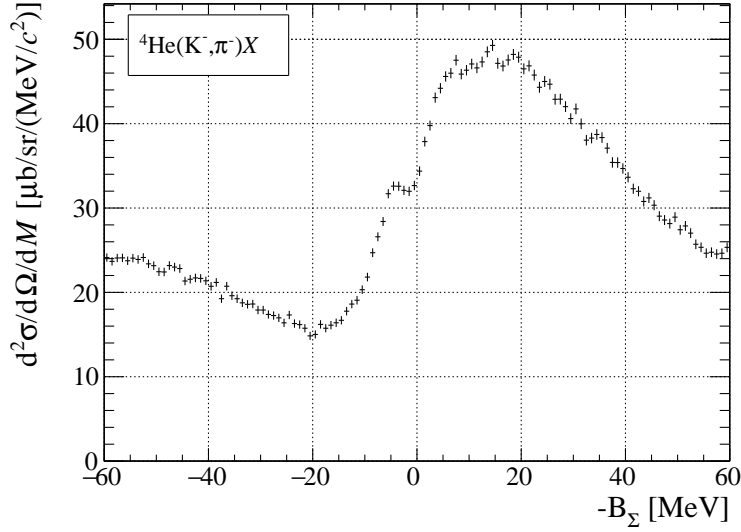
Figure 5.3: Angular averaged B_Σ spectrum.

5.1.1 Fitting of the B_Σ spectrum to search for the excited state of $^4_\Sigma$He

As mentioned above, the excited state of $^4_\Sigma$He was predicted around the Σ thresholds by the theoretical calculation. To search for this excited state, the fitting of the B_Σ spectrum is performed. Details of the fitting procedure is described in this section.

The fitting of the B_Σ spectrum is performed at $B_\Sigma = -55$–40 MeV/c. There are the four components: the ground state of $^4_\Sigma$He, the Λ and Σ quasi-free production processes, and the hypothesical excited states of $^4_\Sigma$He. The four fitting functions are defined for the four components.

Σ hypernucler states for the ground and excited states

For the groud and excited states of $^4_\Sigma$He, the same fitting functions are employed. A simple Gaussian function is not appropliate due to the following two reasons. One reason is that the peak shape of the $^4_\Sigma$He state is broad due to the $\Sigma N \to \Lambda N$ conversion. The other reason is that their shapes should be asymmetric due to the threshold effect.

The Flatte funcion is useful to take into acount these effects. The Flatte function was developed to reproduce the resonance shape of the $K\bar{K}$ system close to the threshold [51]. This function is employed to reproduce the resonance shapes both of the ground and the excited states of $^4_\Sigma$He. The Flatte function is written as

$$f(B_\Sigma) = \begin{cases} \dfrac{C}{a^2 + (q-b)^2} & (B_\Sigma > 0) \\[3mm] \dfrac{C}{(q-a)^2 + b^2} & (B_\Sigma \leq 0) \end{cases} \tag{5.2}$$

q is defined as $q = \sqrt{2\mu|B_\Sigma|/\hbar^2}$ where μ is the reduced mass of Σ and a core nucleus. C

is the normalization constant. The resonance shape depends on the parameters a and b which are related to the binding energy B and the width Γ as

$$B \quad = \quad \frac{\hbar^2 \left(b^2 - a^2\right)}{2\mu}, \tag{5.3}$$

$$\Gamma \quad = \quad -\frac{2\hbar^2 ab}{\mu}, \tag{5.4}$$

To estimate the errors of B and Γ, B and Γ are used as the fitting parameters, and a and b are calculated internally.

Λ quasi-free productions

An exponential function given by Eq. 5.5 is employed to fit the B_Σ distribution of the Λ quasi-free production process as

$$g(B_\Sigma) = C_{\Lambda\mathrm{qf}} \ \exp(\alpha_{\Lambda\mathrm{qf}} B_\Sigma), \tag{5.5}$$

where $C_{\Lambda\mathrm{qf}}$ and $\alpha_{\Lambda\mathrm{qf}}$ are the fitting parameters. $\alpha_{\Lambda\mathrm{qf}}$ should be negative to reproduce the tail shape of the distribution.

Σ quasi-free productions

The missing-mass distribution of the Σ quasi-free production process rises rapidly from the Σ production threshold and has a broad bump structure. It is important how to determine the Σ production threshold in the fitting function. As described above, the Σ quasi-free production process has the two different thresholds, the Σ^+ and Σ^0 thresholds. Therefore, in the fitting function, an effective threshold is employed. The effective threshold M_{th} of the missing mass is determined by averaging the two thresholds. The $T = 1/2$ component is considered to be dominant around the threshold. Then, the $T = 1/2$ state is written with the $^3\mathrm{H} + \Sigma^+$ and the $^3\mathrm{He} + \Sigma^0$ states as

$$|T_{1/2}\rangle = -\sqrt{\frac{2}{3}}\,|^3\mathrm{H}\,\Sigma^+\rangle + \sqrt{\frac{1}{3}}\,|^3\mathrm{He}\,\Sigma^0\rangle. \tag{5.6}$$

By considering the relation, the effective threshold M_{th} of the Σ quasi-free production process is assumed to be

$$M_{\mathrm{th}} = \frac{2}{3}\,M\left(^3\mathrm{H}\Sigma^+\right) + \frac{1}{3}\,M\left(^3\mathrm{He}\Sigma^0\right) = 3999.22\,\mathrm{MeV}. \tag{5.7}$$

Then, the effective threshold B_{th} in the binding energy B_Σ is

$$B_{\mathrm{th}} = M_{\mathrm{th}} - \left[M\left(^3\mathrm{H}\right) + M\left(\Sigma^+\right)\right] = 0.91\,\mathrm{MeV}. \tag{5.8}$$

The fitting function for the Σ quasi-free production process is defined as

$$h(B_\Sigma) \quad = \quad C_{\Sigma\mathrm{qf}}\sqrt{B'_\Sigma}\,\exp\left(\alpha_{\Sigma\mathrm{qf}}B'_\Sigma + \beta_{\Sigma\mathrm{qf}}B'^2_\Sigma\right), \tag{5.9}$$

$$B'_\Sigma \quad = \quad B_\Sigma - B_{\mathrm{th}}. \tag{5.10}$$

The binding energy B_Σ is redefined by using the effective threshold B_{th} as B'_Σ. $\sqrt{B'_\Sigma}$ corresponds to the phase-space volume in the threshold region. The exponential function is employed to reproduce the overall shape of the missing-mass distribution of the Σ quasi-free production process, and $\alpha_{\Sigma\text{qf}}$, and $\beta_{\Sigma\text{qf}}$ are the fitting parameters. $C_{\Sigma\text{qf}}$ is a normalization factor. The $\Sigma N \to \Lambda N$ conversion broadens the missing-mass distribution. This effect is included by folding the function with a Gaussian function.

$$h'(B_\Sigma) = \frac{1}{\sqrt{2\pi}\sigma_{\text{conv}}} \int h(B) \exp\left[-\frac{(B_\Sigma - B)^2}{2\sigma_{\text{conv}}}\right] dB \qquad (5.11)$$

where σ_{conv} is the parameter of the spreading effect.

Effect of the missing-mass resolution

The experimental resolution of the missing mass should be considered. The missing-mass resolution 5.2 MeV/c^2 (FWHM) is estimated from the peak width of the ground state of $^4_\Lambda$He. To include the resolution, the overall fitting function $F(B_\Sigma)$ is smeared by folding with a Gaussian function.

$$F(B_\Sigma) = \frac{1}{\sqrt{2\pi}\sigma_{\text{conv}}} \int \left[f_{\text{gs}}(B) + f_{\text{ex}}(B) + g(B) + h'(B)\right] \exp\left[-\frac{(B_\Sigma - B)^2}{2\sigma_{\text{resol}}}\right] dB$$
$$(5.12)$$

where $f_{\text{gs}}(B_\Sigma)$ and $f_{\text{ex}}(B_\Sigma)$ are the Flatte functions for the ground and the excited states of $^4_\Sigma$He, respectively.

Result of fitting

$F(B_\Sigma)$ given by Eq. 5.12 is fitted to the B_Σ spectrum in the binding-energy range from -55 to 40 MeV. Figure 5.4 shows the result. The black line shows the overall fitting function. The red, blue and green lines show the fit functions for the $^4_\Sigma$He states, the Σ quasi-free production process and the Λ quasi-free production process, respectively. The peaks at $B_\Sigma \approx 6$ MeV and $B_\Sigma \approx -4$ MeV correspond to the ground and the excited states, respectively. The overall fitting function well reproduces the B_Σ spectrum and the reduced χ^2_w value is $90.0/83 = 1.08$.

The best-fit parameters of the fitting are summarized in the first colmun of Table 5.1.

5.1.2 Significance of the excited state of $^4_\Sigma$He

In this section, the significance of the existence of the excited state of $^4_\Sigma$He is discussed. The integrated cross section of the excited state is calculated by using the fitting result. The error is estimated by searching lower/upper cross sections corresponding to $\chi^2 + 1$ by changing the C_{ex} value. The cross section is 74^{+27}_{-21} μb/sr. The significance is 3σ.

To estimate the significance more precisely, a null hypothesis is tested. It is assumed that the excited state does not exist in the null hypothesis whereas the excited exists in the alternative hypothesis. The fitting with the null hypotheses is performed without the component of the excited state f_{ex}.
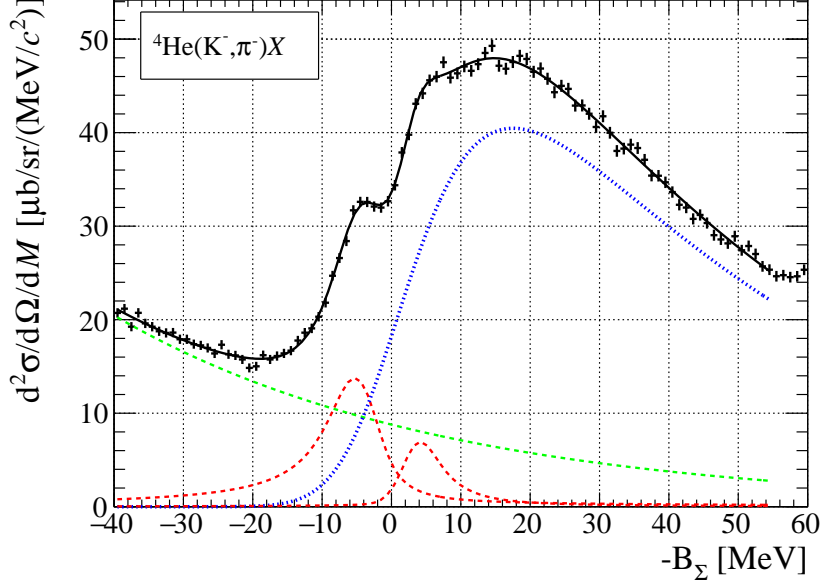
Figure 5.4: Averaged B_Σ spectrum over the angular range of $2° < \theta < 14°$. The red line shows the components of the ground state of $^4_\Sigma$He. The blue and green lines show the components of the Σ and Λ quasi-free production processes, respectively. The black line shows the overall fitting.

Figure 5.5 shows the fitting result of the null hypotheses. It fails to reproduce the threshold region, and the reduced χ^2_{wo} value is $185.8/86 = 2.16$.

The best-fit parameters of the fitting are summarized in the second colmun of Table 5.1.

The χ^2 value of 185.8 with $N_{df} = 86$ in the null hypothesis corresponds to the p value 2.59×10^{-9}. On the other hand, the χ^2 value of 90.0 with $N_{ndf} = 83$ in the alternative hypothesis corresponds to the p value 0.28. The difference in the p values strongly indicates the existence of the excited state. The difference in the χ^2 values between the null and the alternative hypotheses is $185.8 - 90.0 = 95.8$. The probability distribution of the χ^2 difference follows the χ^2 distribution of $N_{df} = 86 - 83 = 3$. The χ^2 difference of 95.8 is quite larger than $N_{df} = 3$. Thus, the null hypothesis should be rejected.

5.1.3 Significance with the different fitting functions

The different fiting functions are fitted to the B_Σ spectrum because the result is possibly senstive to the shape of the fitting function. For this purpose, the fitting function of the Σ quasi-free production process is changed from the square root function to a linear function. In addition, a fitting with a slightly different value of the effective threshold B_{th} is tried. To see the robustness of the existence of the excited state, a simple costant distibution for the Λ quasi-free production process is also tested.

Table 5.1: Parameter list of the overall fitting function in fit(0).

	Parameter	Alternative Value	Null Value
$^{4}_{\Sigma}\mathrm{He_{gs}}$	B_{gs}	-3.55 ± 0.41	-4.83 ± 0.18
	Γ_{gs}	6.14 ± 0.97	2.00 ± 0.82
	C_{gs}	$(1.41 \pm 0.66) \times 10^{-2}$	$(1.04 \pm 0.64) \times 10^{-3}$
$^{4}_{\Sigma}\mathrm{He_{ex}}$	B_{ex}	4.43 ± 0.52	-
	Γ_{ex}	4.45 ± 1.17	-
	C_{ex}	$(4.30 \pm 2.51) \times 10^{-3}$	-
$\Lambda \mathrm{QF}$	$C_{\Lambda\mathrm{qf}}$	$(4.97 \pm 0.28) \times 10^{-1}$	$(5.34 \pm 0.11) \times 10^{-1}$
$\Sigma \mathrm{QF}$	$C_{\Sigma\mathrm{qf}}$	1.30 ± 0.14	1.82 ± 0.82
	$\alpha_{\Sigma\mathrm{qf}}$	$(3.08 \pm 0.27) \times 10^{-2}$	$(4.32 \pm 0.12) \times 10^{-2}$
	$\beta_{\Lambda\mathrm{qf}}$	$(2.09 \pm 0.37) \times 10^{-5}$	$(5.82 \pm 0.23) \times 10^{-4}$
	σ_{conv}	6.17 ± 0.95	8.13 ± 0.38
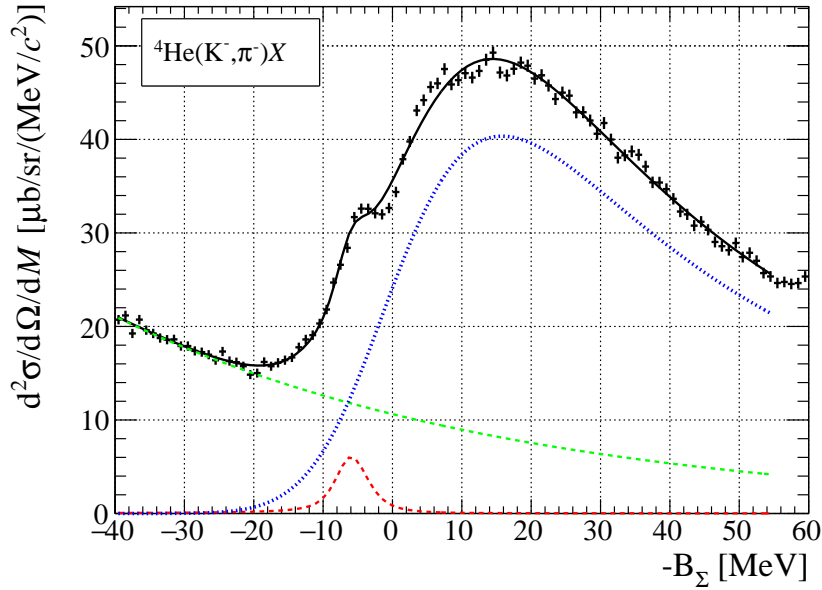
Figure 5.5: Angular averaged B_{Σ} spectrum fitted by assuming no excited state of $^{4}_{\Sigma}\mathrm{He}$. Descriptions for all lines are the same as Fig. 5.4.

(1) Liearly rising function for the Σ quasi-free production process

The fitting with the liearly rising function $H'_{B_{\Sigma}}$ is tried for the Σ quasi-free production process instead of the square-root rising function.

$$H(B_{\Sigma}) \;=\; C_{\Sigma\mathrm{qf}} B'_{\Sigma} \exp(\alpha_{\Sigma\mathrm{qf}} B'_{\Sigma} + \beta_{\Sigma\mathrm{qf}} B'^{2}_{\Sigma}), \qquad (5.13)$$

$$B'_{\Sigma} = B_{\Sigma} - B_{\mathrm{th}},$$

Table 5.2: Summary of the results of the four different fitting functions.

	Null hypothesis		Alternative hypothesis		Difference
	χ^2_{wo}/ndf_{wo}	p_{wo}	χ^2_w/ndf_w	p_w	$\chi^2_{wo} - \chi^2_w$
fit(0)	$185.8/86 = 2.16$	2.59×10^{-9}	$90.0/83 = 1.08$	2.82×10^{-1}	95.9
fit(1)	$194.7/86 = 2.26$	2.14×10^{-10}	$86.4/83 = 1.04$	3.79×10^{-1}	108.3
fit(2)	$185.1/86 = 2.15$	3.19×10^{-9}	$91.2/83 = 1.10$	2.52×10^{-1}	93.9
fit(3)	$168.4/67 = 2.51$	1.08×10^{-10}	$66.0/64 = 1.03$	4.07×10^{-1}	102.4

$$H'(B_\Sigma) = \frac{1}{\sqrt{2\pi}\sigma_{\mathrm{conv}}} \int H(B) \exp\left(-\frac{(B_\Sigma - B)^2}{2\sigma_{\mathrm{conv}}}\right) dB \qquad (5.14)$$

Figures 5.6 and 5.7 show the fitting results in the null and alternative hypotheses, respectively. The meaning of the lines are the same as those in Fig. 5.4. The fitting function for the alternative hypothesis well reproduces the B_Σ spectrum and the reduced χ^2 value is $86.4/83 = 1.04$. On the other hand, the fitting function for the null hypothesis fails to reproduce the B_Σ spectrum in the threshold region, and the reduced χ^2 value is $194.7/86 = 2.23$. The cross section of the excited state is 103.8 ± 8.7 μb/sr. The significance is larger than 10σ. The χ^2 value of 194.7 with $N_{\mathrm{df}} = 86$ in the null hypothesis corresponds to the p value of 2.14×10^{-10}. On the other hand, the χ^2 value of 86.4 with $N_{\mathrm{ndf}} = 83$ in the alternative hypothesis corresponds to the p value of 0.38. The difference in the p values strongly indicates the existence of the excited state. The difference in the χ^2 values between the null and the alternative hypotheses is $194.7 - 86.4 = 108.3$. The probability distribution of the χ^2 difference follows the χ^2 distribution with $N_{\mathrm{df}} = 86 - 83 = 3$. The χ^2 difference of 108.3 is quite larger than $N_{\mathrm{df}} = 3$. Thus, the null hypothesis should be rejected even if the uncertainty in the missing-mass distribution of the Σ quasi-free production process is taken into account.

Figure 5.6: Angular-averaged B_Σ spectrum with the overall fitting assuming the liearly rising function for the Σ quasi-free production and no excited state of $^4_\Sigma$He. Descriptions for all lines are the same as Fig. 5.4.
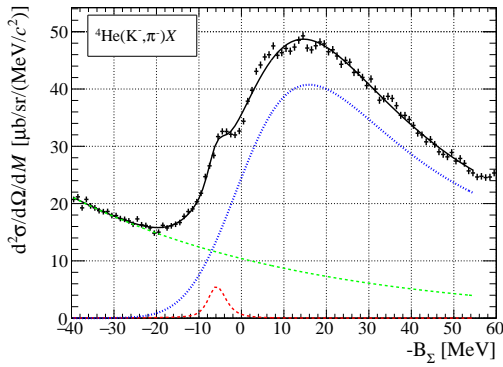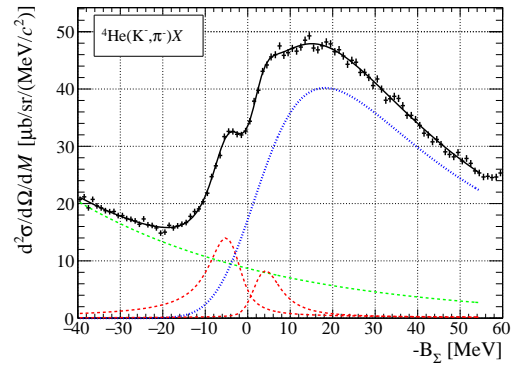
Figure 5.7: Angular-averaged B_Σ spectrum with the overall fitting assuming the liearly rising function for the Σ quasi-free production and the excited state of $^4_\Sigma$He. Descriptions for all lines are the same as Fig. 5.4.

The best-fit parameters of the fitting are summarized in Table 5.3.

Table 5.3: Parameter list of the overall fitting function in fit(1).

	Parameter	Alternative Value	Null Value
$^4_\Sigma\text{He}_\text{gs}$	B_gs	-3.25 ± 0.51	-4.85 ± 0.18
	Γ_gs	7.75 ± 1.04	1.67 ± 0.76
	C_gs	$(2.36 \pm 1.14) \times 10^{-2}$	$(7.58 \pm 4.83) \times 10^{-4}$
$^4_\Sigma\text{He}_\text{ex}$	B_ex	4.27 ± 0.60	$-$
	Γ_ex	5.08 ± 1.40	$-$
	C_ex	$(6.30 \pm 4.41) \times 10^{-3}$	$-$
ΛQF	$C_{\Lambda\text{qf}}$	-1.17 ± 0.12	-0.99 ± 0.04
	$\alpha_{\Lambda\text{qf}}$	$(-2.13 \pm 0.29) \times 10^{-2}$	$(-1.78 \pm 0.11) \times 10^{-2}$
ΣQF	$C_{\Sigma\text{qf}}$	0.59 ± 0.08	0.87 ± 0.02
	$\alpha_{\Sigma\text{qf}}$	0.40 ± 0.06	0.59 ± 0.01
	$\beta_{\Lambda\text{qf}}$	$(-9.60 \pm 0.30) \times 10^{-3}$	$(-2.28 \pm 0.10) \times 10^{-2}$
	σ_conv	6.28 ± 0.83	8.18 ± 0.23

(2) Different threshold of the Σ quasi-free process

The effective threshold of the Σ quasi-free production process might be affected by the ratio of the cross sections of the elementary processes to produce Σ^+ and Σ^0. In Sec. 5.1.1, the prodcuction cross section of Σ^+ is assumed to be same with that of Σ^0. When the production cross section of Σ^+ is twice Σ^0, the effective threshold is 0.55 MeV which is 0.36 MeV lower than the original value. Figures 5.8 and 5.9 show the fitting results with the null and alternative hypotheses, respectively. The fitting function for the alternative hypothesis well reproduces the B_Σ spectrum and the reduced χ^2 value is $111.4/83 = 1.34$. On the other hand, the fitting function for the null hypothesis fails to reproduce the threshold region, and the reduced χ^2 value is $181.8/86 = 2.11$. The cross section of the excite state is 78.4 ± 6.6 μb/sr. The significance is seem to be more than 10σ. The χ^2 value of 181.8 with $N_\text{df} = 86$ in the null hypothesis corresponds to the p value 7.79×10^{-9}. On the other hand, the χ^2 value of 111.4 with $N_\text{ndf} = 83$ in the alternative hypothesis corresponds to the p value of 0.02. The difference in the p values strongly indicates the existence of the excited state. The difference in the χ^2 values between the null and the alternative hypotheses is $181.8 - 111.4 = 70.4$. The probability distribution of the χ^2 difference follows the χ^2 distribution with $N_\text{df} = 86 - 83 = 3$. The χ^2 difference of 70.4 is quite larger than $N_\text{df} = 3$. Thus, the null hypothesis should be rejected even if the uncertainty of the threshold is taken into account.

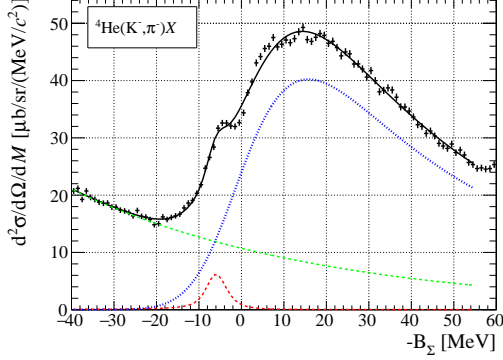The best-fit parameters of the fitting are summarized in Table 5.4.

Figure 5.8: Angular-averaged B_Σ spectrum with the overall fitting assuming shifted threshold for the Σ quasi-free production and no excited of $^4_\Sigma$He. Descriptions for all lines are the same as Fig. 5.5.

Figure 5.9: Angular-averaged B_Σ spectrum with the overall fitting function assuming shifted threshold for the Σ quasi-free production and the excited state of $^4_\Sigma$He. Descriptions for all lines are the same as Fig. 5.4.

(3) Constant distibution for Λ quasi-free

A constant distribution for the Λ quasi-free production process is tested assuming the extreme case of the cross section of the Λ quasi-free production process is much larger than expected. Figures 5.10 and 5.11 show the fitting results with the null and alternative hypotheses, respectively. The fitting function for the alternative hypothesis well reproduces the B_Σ spectrum and the reduced χ^2 value is $66.0/64 = 1.03$. On the other hand, the fitting function for the null hypothesis fails to reproduce the threshold region, and the reduced χ^2 value is $168.4/67 = 2.51$. The cross section of the excite state is 81.2 ± 0.7 μb/sr. The significance is larger than 10σ. The χ^2 value of 168.4 with $N_{df} = 67$ in the null hypothesis corresponds to the p value of 1.08×10^{-10}. On the other hand, the $\chi^2 = 66.0$ with $N_{ndf} = 64$ in the alternative hypothesis corresponds to the p value of 0.41. The difference in the p values strongly indicates the existence of the excited state. The difference in the χ^2 values between the null and the alternative hypotheses is $168.4 - 66.0 = 102.4$. The probability distribution of the χ^2 difference follows the χ^2 distribution with $N_{df} = 67 - 64 = 3$. The χ^2 difference of 102.4 is quite larger than $N_{df} = 3$. Thus, the null hypothesis should be rejected.

The best-fit parameters of the fitting are summarized in Table 5.5.

Conclusion of existence

The null hypothesis is rejected in the all cases assuming the four different fitting functions as summarized in Table 5.2. It strongly suggests the exsistence of the excited state.

5.1.4   Comparison with the past experiments

The binding energies, widths, and cross sections were obtained from the four fitting results as summarized in Table 5.6. The three valiables of the excited state are measured

Table 5.4: Parameter list of the overall fitting function in fit(2).

	Parameter	Alternative Value	Null Value
$^4_\Sigma\text{He}_\text{gs}$	B_gs	-3.25 ± 0.51	-4.85 ± 0.18
	Γ_gs	7.75 ± 1.04	1.67 ± 0.76
	C_gs	$(2.36 \pm 1.14) \times 10^{-2}$	$(7.58 \pm 4.83) \times 10^{-4}$
$^4_\Sigma\text{He}_\text{ex}$	B_ex	4.27 ± 0.60	$-$
	Γ_ex	5.08 ± 1.40	$-$
	C_ex	$(6.30 \pm 4.41) \times 10^{-3}$	$-$
ΛQF	$C_{\Lambda\text{qf}}$	-1.17 ± 0.12	-0.99 ± 0.04
	$\alpha_{\Lambda\text{qf}}$	$(-2.13 \pm 0.29) \times 10^{-2}$	$(-1.78 \pm 0.11) \times 10^{-2}$
ΣQF	$C_{\Sigma\text{qf}}$	0.59 ± 0.08	0.87 ± 0.02
	$\alpha_{\Sigma\text{qf}}$	0.40 ± 0.06	0.59 ± 0.01
	$\beta_{\Lambda\text{qf}}$	$(-9.60 \pm 0.30) \times 10^{-3}$	$(-2.28 \pm 0.10) \times 10^{-2}$
	σ_conv	6.28 ± 0.83	8.18 ± 0.23

Figure 5.10: Angular-averaged B_Σ spectrum with the overall fitting function assuming constant distribution of the Λ quasi-free production and no excited state of $^4_\Sigma\text{He}$. Descriptions for all lines are the same as Fig. 5.5.
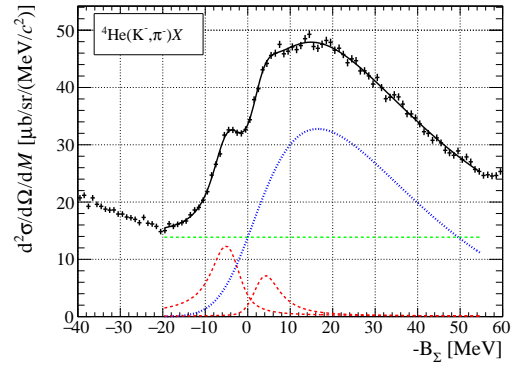
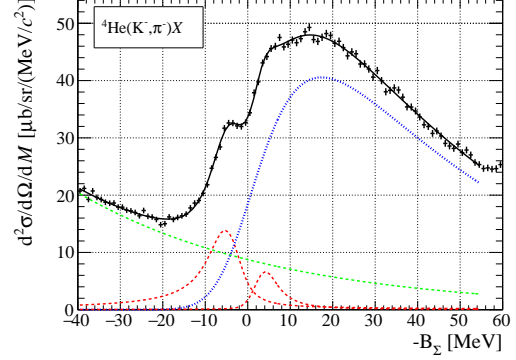Figure 5.11: Angular-averaged B_Σ spectrum with the overall fitting function assuming constant distribution of the Λ quasi-free production and the excited state of $^4_\Sigma\text{He}$. Descriptions of each line are the same as Fig. 5.4.

for the first time. The systematic error is determined by the difference between the all four fitting results. Becuase these observables for the excited state are measured for the first time, there is no data to be compared with the present result.

The binding energy and width of the ground state obtained in this work are compared with the results of the past experiments [25, 30, 52, 32]. These experimental results are summarized in Table 5.7 and Fig. 5.12. The present results are in agreement with other experimental results, but it should be noted that the present values of B and Γ cannot be directly compared with the previous values because the fitting functions are different.

Table 5.5: Parameter list of the overall fitting function in fit(3).

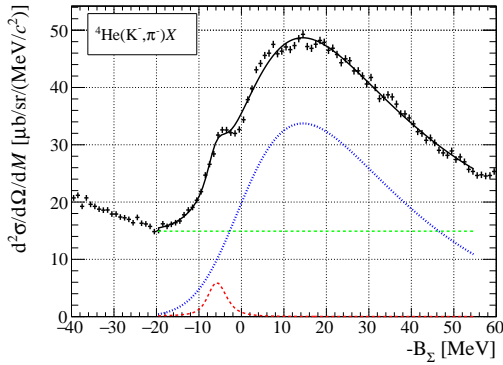|	Parameter	Alternative Value	Null Value
$^{4}_{\Sigma}\mathrm{He}_{\mathrm{gs}}$	B_{gs}	-3.25 ± 0.51	-4.85 ± 0.18
	Γ_{gs}	7.75 ± 1.04	1.67 ± 0.76
	C_{gs}	$(2.36 \pm 1.14) \times 10^{-2}$	$(7.58 \pm 4.83) \times 10^{-4}$
$^{4}_{\Sigma}\mathrm{He}_{\mathrm{ex}}$	B_{ex}	4.27 ± 0.60	$-$
	Γ_{ex}	5.08 ± 1.40	$-$
	C_{ex}	$(6.30 \pm 4.41) \times 10^{-3}$	$-$
ΛQF	$C_{\Lambda\mathrm{qf}}$	-1.17 ± 0.12	-0.99 ± 0.04
	$\alpha_{\Lambda\mathrm{qf}}$	$(-2.13 \pm 0.29) \times 10^{-2}$	$(-1.78 \pm 0.11) \times 10^{-2}$
ΣQF	$C_{\Sigma\mathrm{qf}}$	0.59 ± 0.08	0.87 ± 0.02
	$\alpha_{\Sigma\mathrm{qf}}$	0.40 ± 0.06	0.59 ± 0.01
	$\beta_{\Lambda\mathrm{qf}}$	$(-9.60 \pm 0.30) \times 10^{-3}$	$(-2.28 \pm 0.10) \times 10^{-2}$
	σ_{conv}	6.28 ± 0.83	8.18 ± 0.23

Table 5.6: Summary of fitting results.

	Ground state			Excited state		
	$-B$ [MeV]	Γ [MeV]	$d^2\sigma/d\Omega$ [μb/sr]	$-B$ [MeV]	Γ [MeV]	$d^2\sigma/d\Omega$ [μb/sr]
fit(0)	-3.41 ± 0.43	7.79 ± 0.91	239 ± 15	4.47 ± 0.45	4.03 ± 1.20	74^{+27}_{-21}
fit(1)	-3.25 ± 0.51	7.75 ± 1.04	244 ± 18	4.27 ± 0.60	5.08 ± 1.40	104^{+49}_{-36}
fit(2)	-3.44 ± 0.40	7.88 ± 0.80	243 ± 14	4.50 ± 0.46	5.34 ± 1.28	68^{+24}_{-18}
fit(3)	-3.55 ± 0.41	6.14 ± 0.97	178 ± 12	4.43 ± 0.52	3.77 ± 1.11	81^{+30}_{-23}
	$-3.41^{+0.67}_{-0.55}$	$7.79^{+1.00}_{-2.63}$	239^{+23}_{-74}	$4.47^{+0.49}_{-0.80}$	$4.03^{+2.45}_{-1.37}$	74^{+79}_{-24}

5.2   Angular distribution

To investigate the angular distribution of the cross section, the missing-mass spectra are divided into the six angular ranges $\theta = 2$–4, 4–7.5, 7.5–9, 9–10, 10–12, and 12–14 degrees as shown in Fig. 5.13 with the black line. The $K^- \to \pi^- \pi^0$ decay-background distribution, which is shown with the red points, shifts to the higher missing-mass region as the scattering angle increases. The missing-mass spectrum is divided so that the spectra are not distorted by the edge part of the $K^- \to \pi^- \pi^0$ background distribution in the Σ region. At backward angles $\theta > 7.5$ degrees, there is almost no $K^- \to \pi^- \pi^0$ background. It is noted that the acceptance for the scattering events to the left of the entrance of the SKS magnet at 9–14 degrees may rapidly change and thus have a large ambiguity as mentioned in Sec. 2.4.2. Therefore, only the scattering event to the right is analyzed in these angles.

The divided missing-mass spectra are subtracted by using the simulated background distribution as shown in Fig. 5.14. The distribution of the Λ and Σ quasi-free processes

Table 5.7: Summary of the experimental results about the binding energies and the widths of the ground state of $^4_\Sigma$He.

p_{K^-} [GeV/c]	B [MeV]	Γ [MeV]	Experiment
0	$3.2 \pm 0.3^{+0.1}_{-1.1}$	$4.6 \pm 0.5^{+1.6}_{-1.3}$	KEK-PS E167 [25]
0	2.8 ± 0.7	12.1 ± 1.2	KEK-PS E167 [30]
0.6	4 ± 1	10 ± 2	BNL-AGS E774 [52]
0.6	$4.4 \pm 0.3 \pm 1$	$7.0 \pm 0.7^{+1.2}_{-0.0}$	BNL-AGS E905 [32]
1.5	$-3.41^{+0.67}_{-0.55}$	$7.79^{+1.00}_{-2.63}$	J-PARC E13 (This work)
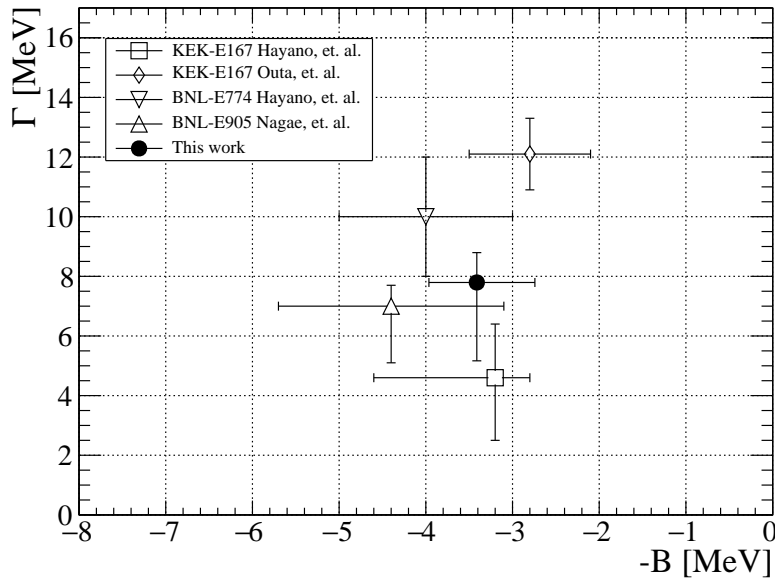
Figure 5.12: Summary of the binding energies and the widths of the ground state of $^4_\Sigma$He reported from different experiments.

become broader at the backward scattering angle as expected. In Fig. 5.14 (b), the background subtraction is not perfect in the missing-mass range of 3940–3990 MeV/c^2, however, this error may have a small effect on the shape of the $^4_\Sigma$He states.

5.2.1 Fitting of the B_Σ spectrum

The B_Σ spectra divided into the six angular ranges are analyzed in this section. The devided B_Σ spectra are fitted by the same fitting functions as the angular-averaged spectrum. The pole parameters (a, b) for the ground and excited states of $^4_\Sigma$He are fixed at the same values with those used in the analysis for the angular-averaged spectrum in Sec. 5.1.1. Since the Σ quasi-free production process is affected by the $\Sigma N \to \Lambda N$ conversion, the smearing parameters for the Σ quasi-free production process are fixed
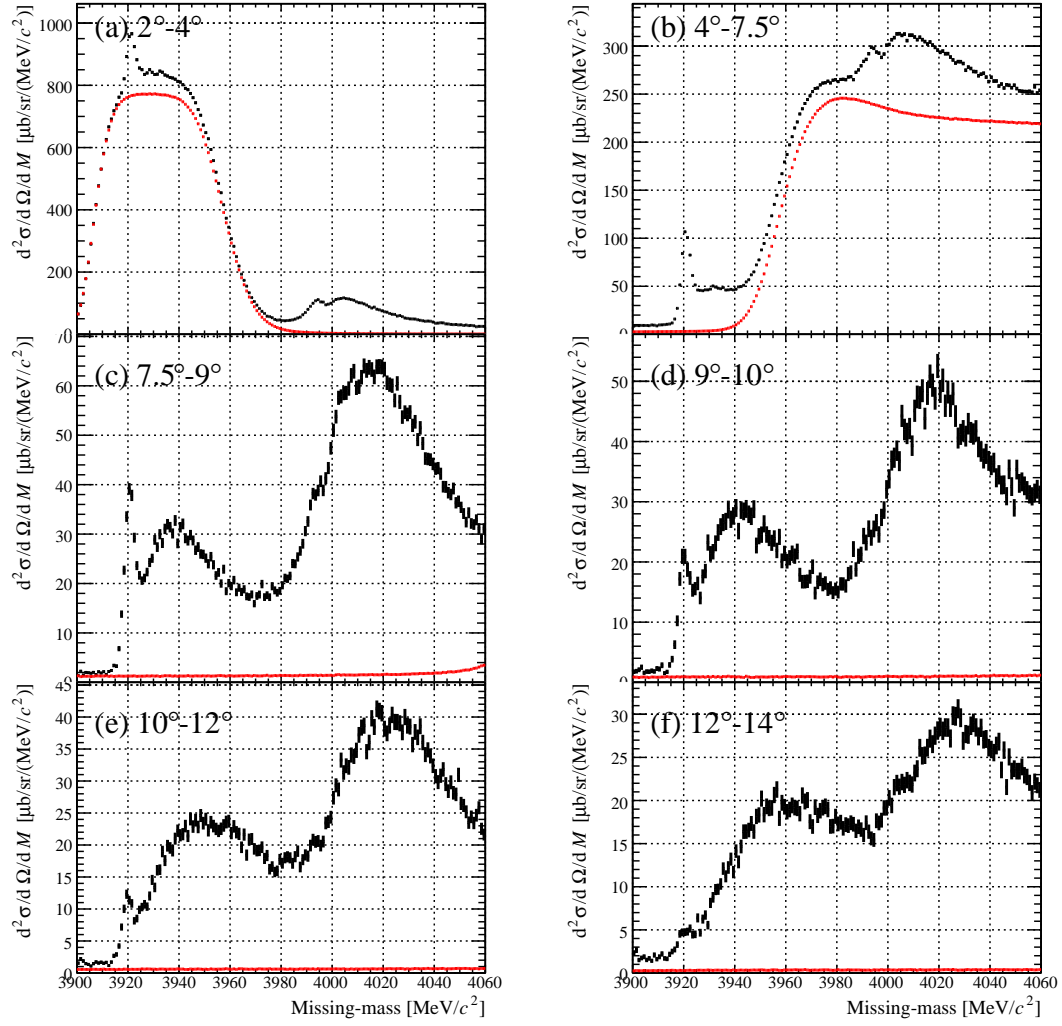
Figure 5.13: Missing-mass spectra of the ^{4}He$(K^-, \pi^-)X$ reaction divided into the six angular ranges. The black points show measured data. The red points show the simulated distribution for the $K^- \rightarrow \pi^- \pi^0$ decay background. (a)-(f) corresponds to the angular ranges, $\theta = 2\text{--}4$, 4–7.5, 7.5–9, 9–10, 10–12, and 12–14 degrees.
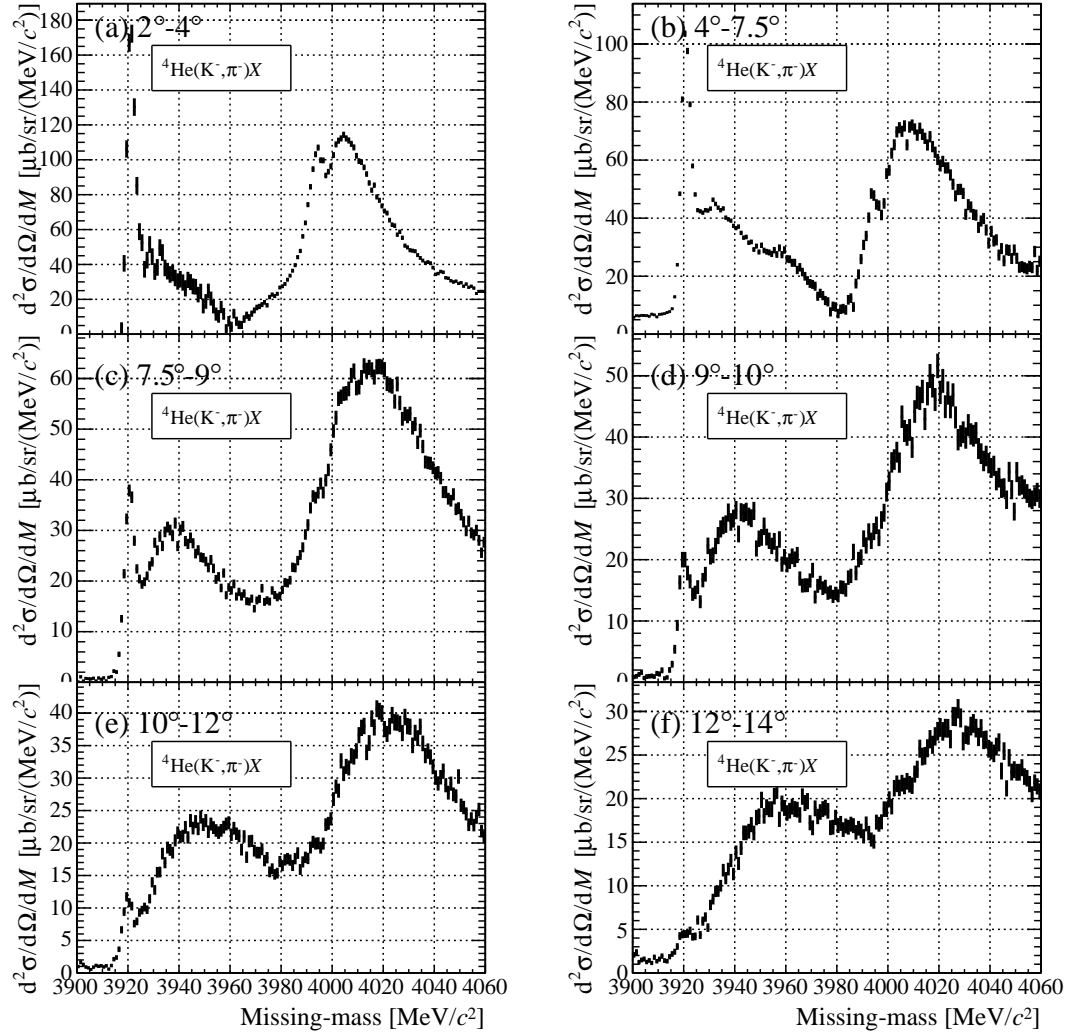
Figure 5.14: Missing-mass spectra of the ^{4}He$(K^-, \pi^-)X$ reaction divided into the six angular ranges after the $K^- \to \pi^- \pi^0$ decay background subtraction. (a)-(f) correspond to the angular ranges, $\theta = 2$–4, 4–7.5, 7.5–9, 9–10, 10–12, and 12–14 degrees.

for all of the spectra. Figure 5.15 shows the B_Σ spectra in the six angular ranges with the fitting functions. The black lines show the fitting function. The red lines show the contributions from the ground state and the excited state of $^4_\Sigma\text{He}$, whereas the blue and green lines show those from the Σ and Λ quasi-free production processes, respectively. For each angular spectrum, the four fittings were also performed in the same way as the angular-averaged spectrum. The fitting function well reproduces the B_Σ spectra. The angular dependence of the reduced χ^2 is shown in Fig. 5.16. The reduced χ^2 value in Fig.5.15(a) is worse than those in the other spectra because the spectrum at 2–4 degrees is not well reproduced in the B_Σ regions of around -20 MeV and 5 MeV due to an oversubtraction of the background. The background subtraction affects the amount of the Λ quasi-free production. The spectrum is fitted with the different function that assumes a flat distribution of Λ quasi-free production in order to estimate the unceartainty of the background subtraction.

5.2.2 Angular distribution of the cross section

The angular distributions of the cross sections for the ground and excited states obtained by the four different fitting functions are shown in Figs. 5.17 and 5.18. The error bars show statistical errors only.

Although fit(0) is carried out with the most realistic assumption, the three different fittings are also performed as described in Sec.5.1.2 in order to evaluate the systematic uncertainties due to the ambiguity of the spectral shapes of the quasi-free processes. Although the magnitudes of the cross sections significantly fluctuate between the different fittings, the shapes of the angular distributions do not change much. In order to estimate the systematic errors of the cross section in the normalization and around the most likelihood value separately, the cross sections from the fit(1), fit(2), and fit(3) are renormalized to minimize the differences from the fit(0) as shown in Figs. 5.19 and 5.20. The scale factors are listed in Table 5.8. The systematic error in the normalization

Table 5.8: Scales of the angular distibutions for the three fittings.

	Ground state	Excited state
fit(1)	1.06	0.95
fit(2)	0.63	0.79
fit(3)	1.39	1.15

is estimated from the standard deviation of the scale factors. Assuming the four cross sections in each angular range are independent, the most likelihood value is determined from the error-weighted mean of the four values. The probability density function (PDF) for the averaged cross section is obtained as a sum of the four PDFs for the cross sections in each angular region. Each PDF is assumed to be a Gaussian function with a width is taken from the statistical error of the cross section. The systematic error of the averaged cross section is determined from the 68.3% confidence interval in the PDF around the most likelihood value. Figure 5.21 shows the angular distribution of the cross sections

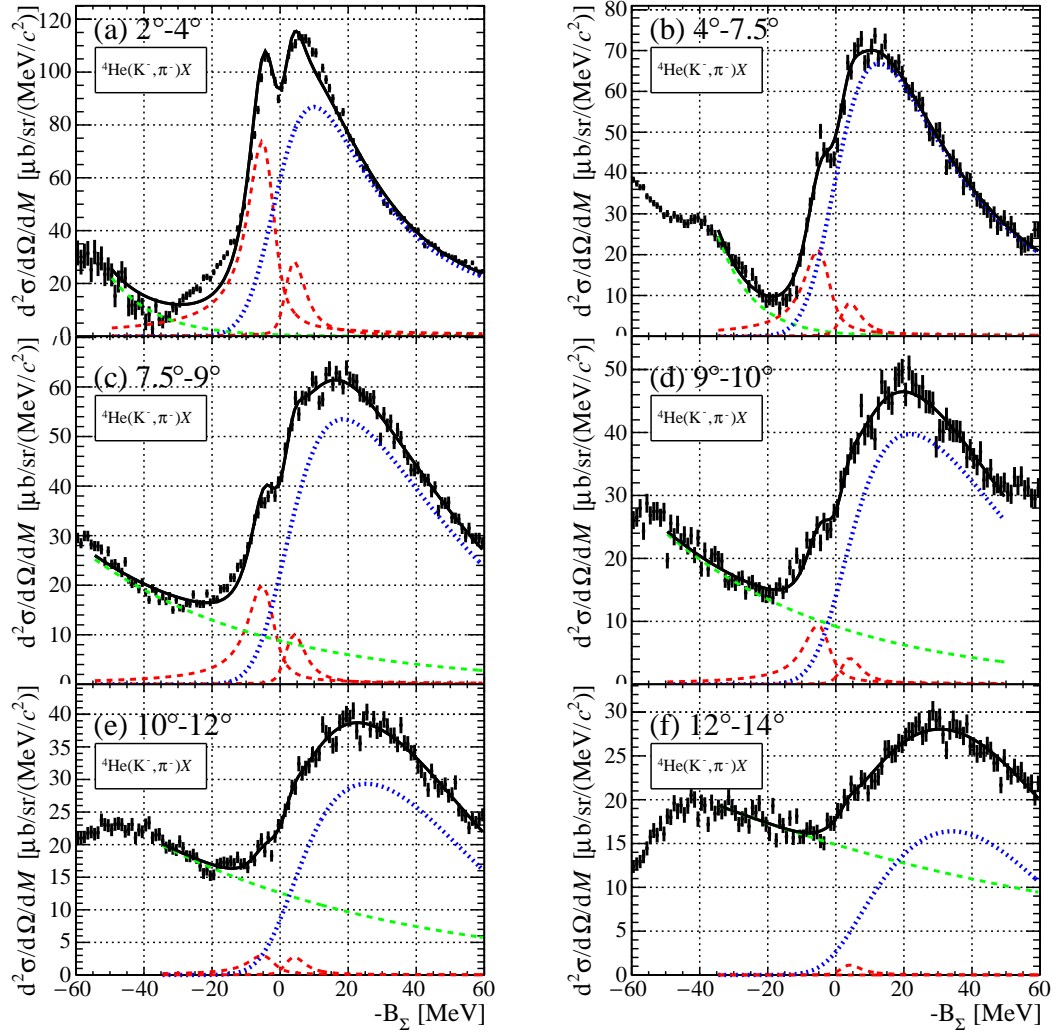Figure 5.15: B_Σ spectra divided into the six angular ranges assuming the excited state of $^4_\Sigma$He. The black lines show the overall fitting function. The red lines show components of the ground state of $^4_\Sigma$He and the excited state of $^4_\Sigma$He. Descriptions for the blue and green lines are the same as Fig. 5.4.
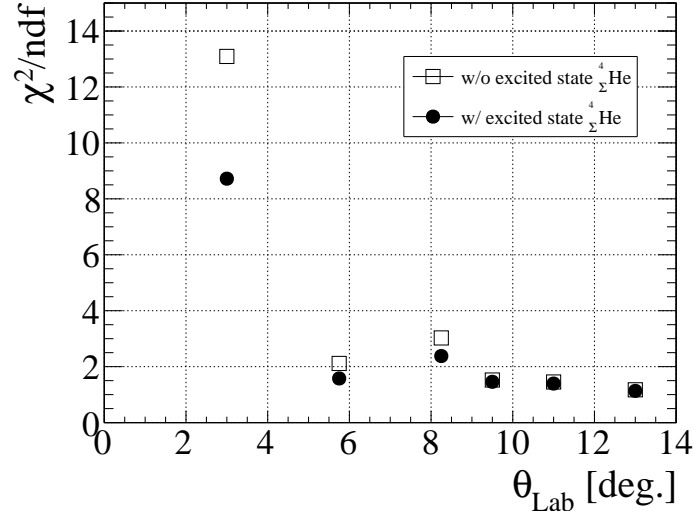
Figure 5.16: Angular distribution of the reduced χ^2_{wo} (open squares) and χ^2_w (filled circles).
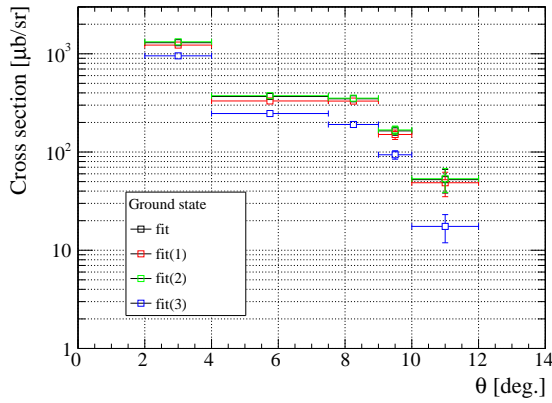
Figure 5.17: Angular distribution of the cross sections of the ground state of $^4_\Sigma$He as shown by the open boxes. The errors are the statistical errrs only.

Figure 5.18: Angular distribution of the cross sections of the excited state of $^4_\Sigma$He as shown by the filled circles. The Y axis in the figure is in logarithmic scale. The errors are the statistical errrs only.

for the ground and excited states of $^4_\Sigma$He with the systematic errors in the normalization and around the most likelihood values. The numerical values of the cross sections are tabulated in Table 5.9.

The cross sections of both the ground and excited states decrease as the angle increases. The spin and parity of each state is theoretically predicted to be 0^+ and 1^-. It is expected that the difference in the transferred angular momenta affects the difference in the slopes in principle, but no clear difference between the ground and excited states is observed. It is, therefore difficult to distinguish the difference in their spins from the
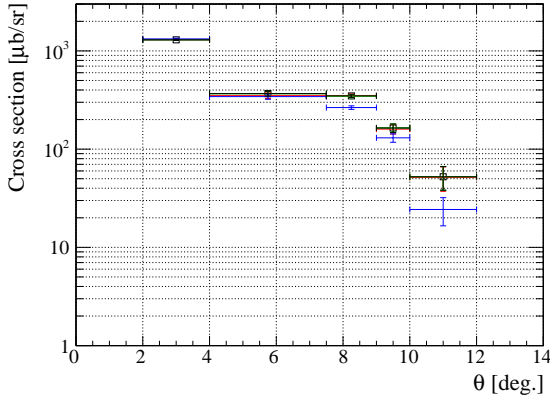
Figure 5.19: Angular distribution of the renormalized cross sections of the ground state of $^4_\Sigma$He as shown by the open boxes. The errors are the statistical errrs only.
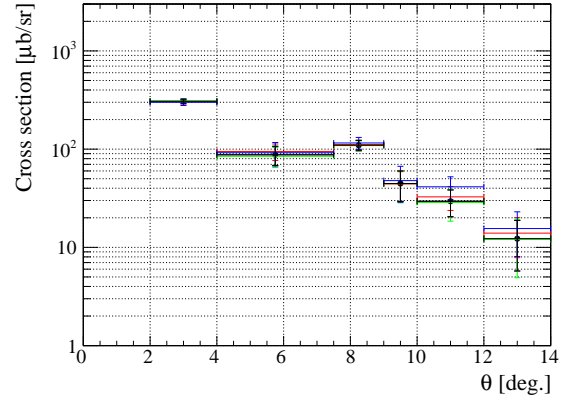
Figure 5.20: Angular distribution of the renormalized cross sections of the excited state of $^4_\Sigma$He as shown by the filled circles. The errors are the statistical errrs only.

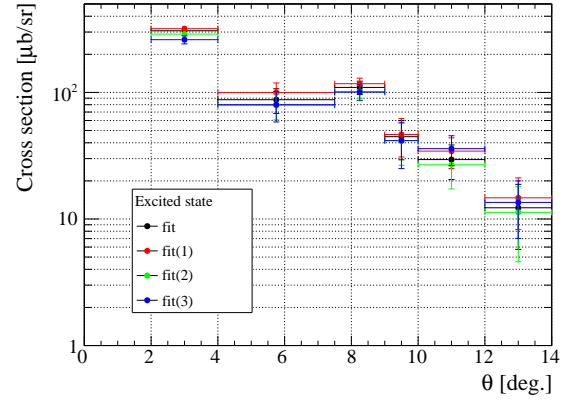Table 5.9: Cross sections for the ground and excited states of $^4_\Sigma$He. The errors do not include the systematic uncertainty in the normalization.

Angle	Ground state $d^2\sigma/d\Omega$ [μb/sr]	Excited state $d^2\sigma/d\Omega$ [μb/sr]
2°–4°	1306^{+26}_{-23}	304^{+18}_{-18}
4°–7.5°	354^{+24}_{-24}	91.5^{+21}_{-21}
7.5°–9°	340^{+19}_{-75}	112^{+14}_{-14}
9°–10°	152^{+22}_{-24}	45^{+17}_{-16}
10°–12°	43^{+20}_{-20}	34^{+11}_{-10}
12°–14°	-	14^{+7}_{-7}

difference in their slopes.

5.3 Comparison with theoretical prediction

5.3.1 Shape of the missing-mass spectrum

The measured centroid energies of the ground state and the excited state are compared with the prediction by the theoretical calculation. For the ground state, the measured centroid energy is $B = 3.41^{-0.67}_{+0.55}$ MeV, and is consistent with both the past experimental value of $B = 4 \pm 1$ MeV and the theoretical value of $B \approx 4$ MeV. It should be noted that the theoretical calculations determine the Σ-nucleus potential to reproduce the centroid energy in the past experiments.

The centroid energy of the excited state is determined to be $B = -4.47^{+0.48}_{-0.80}$ MeV
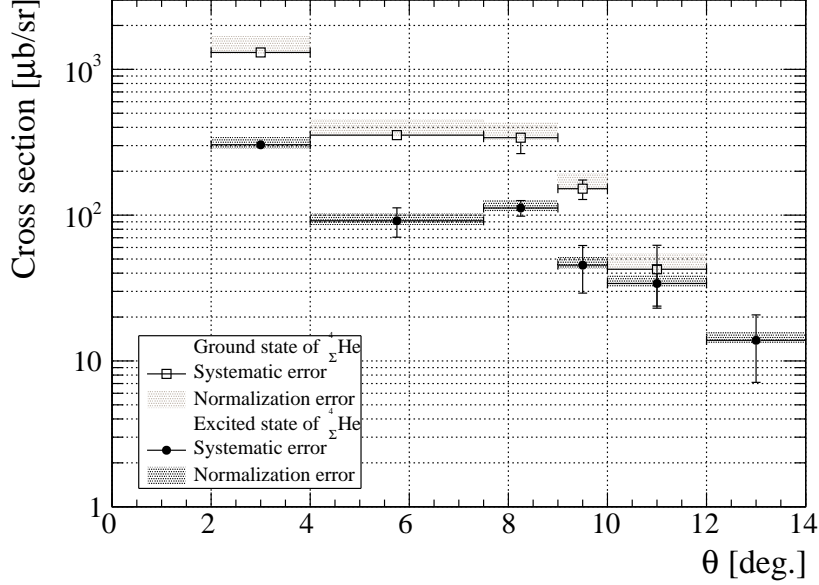
Figure 5.21: Angular distribution of the cross sections of the ground state of $^4_\Sigma$He (open boxes) and the excited state of $^4_\Sigma$He (filled circles). The vertical error bars show the systematic errors around the most likelihood values. The shade boxes show the normalization errors.

in the present measurement for the first time. Because the depth of the real part of the Σ-nucleus potential affects the orbital energy of Σ, the centroid energy depends on the depth of the real part. When the real part is deeper, the centroid energy is lower. On the contrary, when the real part is shallower, the centroid energy is higher as discussed in Sec. 1.5.

The measured missing-mass spectrum at $\theta = 7.5$–$9°$ is compared with theoretical prediction at $\theta = 8°$ in Figs. 5.22 and 5.23 [40]. The centroid energy of the excited state is predicted to be $B \approx 3$ MeV when the normalization factor for the real part is $N_R = 1.0$, and $B \approx 5$ MeV when the normalization factor is $N_R = 0.6$. According to the present measurement, N_R is likely to be in the range of $N_R = 0.6$–1.0. However, this normalization factor cannot explain the cross section because the theoretical cross section of the excited state is larger than that of the ground state, unlike the experimental results. Moreover, the theoretical calculation does not consider the energy dependence of the cross section of the elementary process. The theoretical cross section also decreases when the imaginary part of the ΣN potential. If the coupling to the other reaction channel such as the Λ-Σ coupling is stronger than expected, the imaginary part should be enhanced.

5.3.2   Angular distribution

The angular distributions of the measured cross sections for the ground and excited states are compared with the theoretical predictions in Fig. 5.24.

Figure 5.22: Measured missing-mass spectrum at $\theta = 7.5$–$9°$ after the background subtraction.
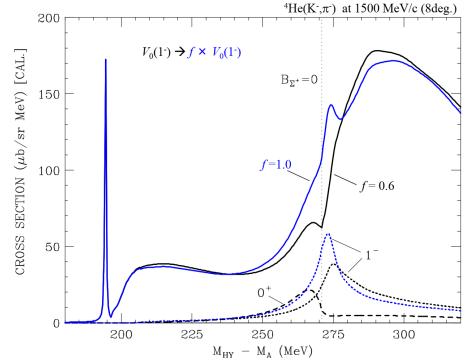
Figure 5.23: Theoretically predicted missing-mass spectrum at $\theta = 8°$ [40].
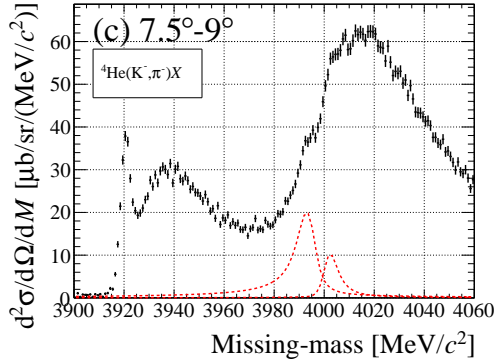
The calculated cross sections are significantly larger than the measured cross sections except for the ground state at $\theta = 2$–$4°$. This result suggests that the imaginary part of the Σ-nucleus potential is larger than expected. The present result should provide a new insight into the Σ-nucleus interaction.

The slope of the angular distribution of the calculated cross section for the ground state is slightly steeper than that for the excited state. This may reflect the difference in the transferred angular momenta between the ground and excited states. However, the calculated slopes for the ground and excited states are both inconsistent with the experiment. In addition, the slope of the measured cross section for the ground state is almost same with that for the excited state. Therefore, it is difficult to distinguish and determine the angular momenta of the Σ hyperons in the ground and excited states in the present analysis.

The angular distribution of the scattering cross section is also affected by the radius of the nucleus in principle. Measurements of the nuclear radii by elastic scattering have been widely performed. In the elastic scattering, the angular distribution of the cross section directly reflects the nuclear radius, since the initial and final states are the same. However, in the case of the (K^-, π^-) reaction with different initial and final states, the relationship between the angular distribution and the nuclear radius is not straightforward.

The theoretical calculation does not satisfactorily describe the angular distributions of the cross sections for the ground and excited states and their relative strength. The further theoretical studies are strongly desired to clarify the Σ-nucleus interaction.

5.4 Future prospect

5.4.1 Follow-up experiment

In the present study, the binding-energy spectrum of $^4_\Sigma$He was obtained with a good statistical accuracy. Because of the large widths of $^4_\Sigma$He states, it is not easy to improve
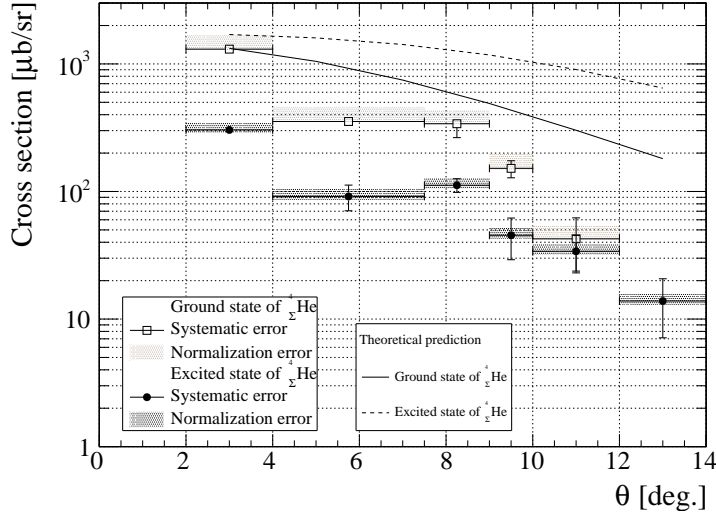
Figure 5.24: Predicted angular distributions of the cross sections for the ground and excited state of $_\Sigma^4$He compared with the measured angular distributions. The solid and dashed lines are the theoretical cross sections of the ground and excited states, respectively.

the peak fitting by accumulating more statistics in the inclusive ^{4}He$(K^-, \pi^-)X$ measurement. The follow-up experiment should be carried out to tag the decay of the Σ hypernuclei for exclusive measurements. Since the Σ hypernucleus decays by the Σ-Λ conversion, unlike the Σ quasi-free production process, one can distinguish the Σ hypernucleus production from the Σ quasi-free production process using a detector for tagging the Λ decay. This measurement was performed in ANL, but the statistical accuracy and missing-mass resolution were poor[53]. Measurements with high statistical accuracy and missing-mass resolution should be performed.

5.4.2   Search for other Σ hypernuclei

There still remain Σ hypernuclei other than $_\Sigma^4$He which have not been fully explored, yet. It is possible to produce a light nucleus with a relatively strong isospin dependent term as described in Sec. 1.4. When Σ hypernuclei with different mass numbers A are found and their binding energies can be measured, the Σ-nucleus potential can be further restricted from the measured binding energies. Since the mass number of $_\Sigma^3$He is smaller than $_\Sigma^4$He, the isospin-dependent term of the Σ-nucleues potential is more emphasized. For example, there is a theoretical prediction that $_\Sigma^3$He can be observed via the ^{3}He$(K^-, \pi^-)X$ reaction, as well as $_\Sigma^4$He [54]. It also may be to fruitful investigate the bound state of ΣN by measuring the missing mass of the $d(K^-, \pi^-)X$ reaction. The isospin-dependent term can be further understood.

5.4.3 Spin-orbit interaction

It is theoretically predicted that the spin-orbit interaction in the ΣN interaction is stronger than that in the NN interaction [55], while the spi-orbit interaction of the ΛN interaction is weaker than that of the NN interaction. If the LS splitting caused by the spin-orbit interaction is larger than the natural width of the Σ hypernucleus (about 7 MeV), it is possible to measure the effect of the spin-orbit interaction by precisely measuring the mass distribution of the Σ hypernuclear states.

Chapter 6

Summary

To investigate the ΣN interaction, it is necessary to examine Σ hypernuclei. $^{4}_{\Sigma}$He is the only Σ hypernucleus ever discovered. Only the ground state of $^{4}_{\Sigma}$He was observed in KEK and BNL using K^- beams with momenta at $p_{K^-} = 0$ and 0.6 GeV/c. The current theoretical calculations cannot reprodece the measured missing-mass spectra unless the Σ-nucleus potential for the excited state is scaled by a normalization factor. However, the potential for the excited state is uncertain since no excited state has been observed. Therefore, the excited state of $^{4}_{\Sigma}$He should be searched for to investigate the Σ-nucleus interaction in more detail.

The missing-mass spectrum for the ^{4}He$(K^-, \pi^-)X$ reaction at $p_{K^-} = 1.5$ GeV/c was measured in the J-PARC E13 experiment. The liquid ^{4}He target with a thickness of 2.7 g/cm^2 was used. Momenta of kaon and pion were measured using the K1.8 beam line and the SKS spectrometer systems, respectively. The SKS system has a large momentum (p_{π^-}=1.1–1.5 GeV/c) and an angular (θ_{lab}=2–14°) acceptances and a good momentum resolution ($\Delta p/p \sim 10^{-3}$). The missing-mass resolution was 5.0 MeV/c (FWHM) for the ground state of $^{4}_{\Lambda}$He.

The $K^- \rightarrow \pi^- \pi^0$ decay events were the main background and their missing-mass spectrum was estimated by a Monte Calro simulation. The measured missing-mass spectrum was subtracted by the simulated background spectrum. The measured spectrum was analyzed by taking into account the ground and excited states in $^{4}_{\Sigma}$He and the Λ and Σ quasi-free production processes. It was found that the measured binding energy and the width of the ground state were consistent with both of the past experimental resluts and the theoretical prediction. To estimate the significance of the existence of the excited state, the null and alternative hypotheses were tested. The null hypothesis was defined as the assumption that there was no excited state. On the other hand, the alternative hypothesis was defined as the assumption that there was the excited state. As the results, the reduced χ^2 value of the alternative hypothesis was 1.08, whereas the probability of null hypothesis was 2×10^{-9}. Thus, the exsistence of the excited state was strongly suggested.

The measured binding energy of the excited state was found to be $4.47^{+0.49}_{-0.80}$ MeV, and this value was within the expected range when the real part of the Σ-nucleus potential

was scaled by a factor of $N_R = 0.6$–1.0. The measured cross section of the excited state was smaller than that of the ground state although the theoretical cross section for the excited state was larger than that for the ground state. This fact suggests that the imaginary part of the Σ-nucleus potential for the excited state might be much larger than that for the ground state.

The measured missing-mass spectrum for the $^4\mathrm{He}(K^-, \pi^-)X$ reaction was divided into the six angular ranges, and the angular distributions of the differential cross sections for the ground and excited states were obtained for the first time. There is almost no difference in the slopes of the angular distributions between the ground and excited states. It is, therefore difficult to distinguish their spins from slopes. The slopes of the measured angular distributions are steeper than the theoretical prediction. It implies that the size of the hypernucleus is possibly larger than expected.

The theoretical calculation does not satisfactorily describe the angular distributions of the cross sections for the ground and excited states and their relative strength. The present result should provide an important insight into the Σ-nucleus interaction, and further theoretical studies are strongly desired to clarify the Σ-nucleus interaction.

Acknowledgements

First of all, I would like to thank all the people who worked together with me, gave advice, supported, and encouraged me to complete the present work. I would like to express my deepest gratitude to Prof. A. Sakaguchi who provided helpful comments and suggestions. I would like to deeply acknowledge Prof. H. Tamura who is the spokesperson of the present experiment. He gladly accepted me as a member of the J-PARC E13 collaboration and a doctor candidate, when I was a doctor course student. I also owe a very important debt to Prof. T. Kawabata whose opinions and information have helped me very much throughout the production of this study. I would like to express my great thanks to Prof. T. Harada for the discussion of the interpretation of experimental results. I appreciate thier supports to write the present thesis.

I would like to thank the J-PARC E13 collaboration, especially, the members who worked together with me. The present experiment could not be carried out without their efforts. Dr. T. O. Yamamoto took the most important role in this experiment. The present experiment succeeded under his leadership. I also appreciate Dr. M. Ukai. She guided me through the all of this work: test experiments for detector study, preparation and operation of the experiment and the present analysis. Dr. R. Honda, Dr. S. B. Yang, and Mr. Y. Sasaki who are main members of the present experiment. This work was successfully completed with their great contributions. Owing to Mr. K. Tanabe, Mr. T. Yamamoto, Ms. N. Ichige, Ms. S. Suto, and Dr. M. Fujita, the areogel detectors and the Hyperball detectors, which were key detectors to handle the high intensity beam, could be developed. I appreciate Dr. S. B. Yang and Dr. H. Ekawa for the drift chambers and also appreciate Dr. K. Hosomi and Dr. S. H. Hayakawa for the DAQ system. I would like to thank Mr. N. Chiga who greatly contribute for design and construction of detectors. The K1.8 beamline and SKS collaboration gave me an opportunity to participate in all the experiments performed in J-PARC K1.8 beamline. I would like to greatly thank Prof. T. Takahashi. He managed a lot of tasks for us and valued my works in this beamline. The present experiment was successfully performed owing to the staffs of J-PARC and KEK. I would like to acknowledge the Hadron beam channel group and the accelerator group.

I would like to greatly acknowledge members of "Nuclear Spectroscopy Group" in Osaka University. I am grateful to Mr. Akaishi, Mr. Y Nakada, Mr. K. Oue, Mr. T. Hayakawa, Mr. K. Kobayashi, and Mr. S. Hoshino for the help and encouragement. I also would like to thank Mrs. T. Fujita, Ms. A. Yagi, Mr. K. Tetsuno,

Bibliography

[1] Jochen Erler, Noah Birge, Markus Kortelainen, Witold Nazarewicz, Erik Olsen, Alexander M Perhac, and Mario Stoitsov. The limits of the nuclear landscape. *Nature*, 486(7404):509, 2012.

[2] Michael Thoennessen. The discovery of isotopes. *Switzerland: Springer Int. Publ*, 2016.

[3] Thomas A. Rijken, M. M. Nagels, and Yasuo Yamamoto. Baryon-Baryon Interactions: 一 Nijmegen Extended-Soft-Core Models 一. *Progress of Theoretical Physics Supplement*, 185:14–71, 06 2010.

[4] R. Machleidt. High-precision, charge-dependent bonn nucleon-nucleon potential. *Phys. Rev. C*, 63:024001, Jan 2001.

[5] R. B. Wiringa, V. G. J. Stoks, and R. Schiavilla. Accurate nucleon-nucleon potential with charge-independence breaking. *Phys. Rev. C*, 51:38–51, Jan 1995.

[6] M M Majumdar, B C Samanta, and S K Samaddar. Energy-dependent nucleus-nucleus potential with the paris interaction. *Journal of Physics G: Nuclear and Particle Physics*, 17(9):1387–1400, sep 1991.

[7] M. Tanabashi, K. Hagiwara, K. Hikasa, K. Nakamura, Y. Sumino, F. Takahashi, J. Tanaka, K. Agashe, G. Aielli, C. Amsler, M. Antonelli, D. M. Asner, H. Baer, Sw. Banerjee, R. M. Barnett, T. Basaglia, C. W. Bauer, J. J. Beatty, V. I. Belousov, J. Beringer, S. Bethke, A. Bettini, H. Bichsel, O. Biebel, K. M. Black, E. Blucher, O. Buchmuller, V. Burkert, M. A. Bychkov, R. N. Cahn, M. Carena, A. Ceccucci, A. Cerri, D. Chakraborty, M.-C. Chen, R. S. Chivukula, G. Cowan, O. Dahl, G. D'Ambrosio, T. Damour, D. de Florian, A. de Gouvêa, T. DeGrand, P. de Jong, G. Dissertori, B. A. Dobrescu, M. D'Onofrio, M. Doser, M. Drees, H. K. Dreiner, D. A. Dwyer, P. Eerola, S. Eidelman, J. Ellis, J. Erler, V. V. Ezhela, W. Fetscher, B. D. Fields, R. Firestone, B. Foster, A. Freitas, H. Gallagher, L. Garren, H.-J. Gerber, G. Gerbier, T. Gershon, Y. Gershtein, T. Gherghetta, A. A. Godizov, M. Goodman, C. Grab, A. V. Gritsan, C. Grojean, D. E. Groom, M. Grünewald, A. Gurtu, T. Gutsche, H. E. Haber, C. Hanhart, S. Hashimoto, Y. Hayato, K. G. Hayes, A. Hebecker, S. Heinemeyer, B. Heltsley, J. J. Hernández-Rey, J. Hisano, A. Höcker, J. Holder, A. Holtkamp, T. Hyodo, K. D. Irwin, K. F. Johnson, M. Kado,

M. Karliner, U. F. Katz, S. R. Klein, E. Klempt, R. V. Kowalewski, F. Krauss, M. Kreps, B. Krusche, Yu. V. Kuyanov, Y. Kwon, O. Lahav, J. Laiho, J. Lesgourgues, A. Liddle, Z. Ligeti, C.-J. Lin, C. Lippmann, T. M. Liss, L. Littenberg, K. S. Lugovsky, S. B. Lugovsky, A. Lusiani, Y. Makida, F. Maltoni, T. Mannel, A. V. Manohar, W. J. Marciano, A. D. Martin, A. Masoni, J. Matthews, U.-G. Meissner, D. Milstead, R. E. Mitchell, K. Mönig, P. Molaro, F. Moortgat, M. Moskovic, H. Murayama, M. Narain, P. Nason, S. Navas, M. Neubert, P. Nevski, Y. Nir, K. A. Olive, S. Pagan Griso, J. Parsons, C. Patrignani, J. A. Peacock, M. Pennington, S. T. Petcov, V. A. Petrov, E. Pianori, A. Piepke, A. Pomarol, A. Quadt, J. Rademacker, G. Raffelt, B. N. Ratcliff, P. Richardson, A. Ringwald, S. Roesler, S. Rolli, A. Romaniouk, L. J. Rosenberg, J. L. Rosner, G. Rybka, R. A. Ryutin, C. T. Sachrajda, Y. Sakai, G. P. Salam, S. Sarkar, F. Sauli, O. Schneider, K. Scholberg, A. J. Schwartz, D. Scott, V. Sharma, S. R. Sharpe, T. Shutt, M. Silari, T. Sjöstrand, P. Skands, T. Skwarnicki, J. G. Smith, G. F. Smoot, S. Spanier, H. Spieler, C. Spiering, A. Stahl, S. L. Stone, T. Sumiyoshi, M. J. Syphers, K. Terashi, J. Terning, U. Thoma, R. S. Thorne, L. Tiator, M. Titov, N. P. Tkachenko, N. A. Törnqvist, D. R. Tovey, G. Valencia, R. Van de Water, N. Varelas, G. Venanzoni, L. Verde, M. G. Vincter, P. Vogel, A. Vogt, S. P. Wakely, W. Walkowiak, C. W. Walter, D. Wands, D. R. Ward, M. O. Wascko, G. Weiglein, D. H. Weinberg, E. J. Weinberg, M. White, L. R. Wiencke, S. Willocq, C. G. Wohl, J. Womersley, C. L. Woody, R. L. Workman, W.-M. Yao, G. P. Zeller, O. V. Zenin, R.-Y. Zhu, S.-L. Zhu, F. Zimmermann, P. A. Zyla, J. Anderson, L. Fuller, V. S. Lugovsky, and P. Schaffner. Review of particle physics. *Phys. Rev. D*, 98:030001, Aug 2018.

 [8] D.H. Davis. 50 years of hypernuclear physics: I. the early experiments. *Nuclear Physics A*, 754:3 – 13, 2005. Proceedings of the Eighth International Conference on Hypernuclear and Strange Particle Physics.

 [9] Makoto Oka, Kiyotaka Shimizu, and Koichi Yazaki. Quark Cluster Model of Baryon-Baryon Interaction. *Progress of Theoretical Physics Supplement*, 137:1–20, 03 2000.

[10] Th.A. Rijken, M.M. Nagels, and Y. Yamamoto. Status of understanding the yn/yy-interactions meson-exchange viewpoint. *Nuclear Physics A*, 835(1):160 – 167, 2010. Proceedings of the 10th International Conference on Hypernuclear and Strange Particle Physics.

[11] Takashi Inoue, HAL QCD Collaboration, Noriyoshi Ishii, HAL QCD Collaboration, Sinya Aoki, HAL QCD Collaboration, Takumi Doi, HAL QCD Collaboration, Tetsuo Hatsuda, HAL QCD Collaboration, Yoichi Ikeda, HAL QCD Collaboration, Keiko Murano, HAL QCD Collaboration, Hidekatsu Nemura, HAL QCD Collaboration, Kenji Sasaki, and HAL QCD Collaboration. Baryon-Baryon Interactions in the Flavor SU(3) Limit from Full QCD Simulations on the Lattice. *Progress of Theoretical Physics*, 124(4):591–603, 10 2010.

[12] F. Eisele, H. Filthuth, W. Föhlisch, V. Hepp, and G. Zech. Elastic $\sigma^{\pm}p$ scattering at low energies. *Physics Letterahns B*, 37(2):204 – 206, 1971.

[13] J.K. Ahn, B. Bassalleck, M.S. Chung, W.M. Chung, H. En'yo, T. Fukuda, H. Funa-hashi, Y. Goto, A. Higashi, M. Ieiri, M. Iinuma, K. Imai, Y. Itow, H. Kanda, Y.D. Kim, J.M. Lee, A. Masaike, Y. Matsuda, I.S. Park, Y.M. Park, N. Saito, S. Mi-hara, Y.M. Shin, K.S. Sim, R. Susukita, R. Takashima, F. Takeutchi, P. Tlustý, S. Yamashita, S. Yokkaichi, and M. Yoshida. $\sigma^+ p$ elastic scattering in the region of $300 \leq p_{\Sigma+} \leq 600$ MeV/c with a scintillating fiber target. *Nuclear Physics A*, 648(3):263 – 279, 1999.

[14] Y. Kondo, J.K. Ahn, H. Akikawa, J. Arvieux, B. Bassalleck, M.S. Chung, H. En'yo, T. Fukuda, H. Funahashi, S.V. Golovkin, A.M. Gorin, Y. Goto, M. Hanabata, T. Hayakawa, A. Ichikawa, M. Ieiri, K. Imai, M. Ishino, H. Kanda, Y.D. Kim, E.N. Kozarenko, I.E. Kreslo, J.M. Lee, A. Masaike, S. Mihara, K. Nakai, K. Nakazawa, K. Ozawa, A. Sato, H.D. Sato, K.S. Sim, T. Tabaru, F. Takeutchi, P. Tlustý, H. Torii, K. Yamamoto, S. Yokkaichi, and M. Yoshida. σ-p elastic-scattering in the region of $400< p_{\Sigma-} <700$ mev/c with a scintillating-fiber active target. *Nuclear Physics A*, 676(1):371 – 387, 2000.

[15] J.K. Ahn, H. Akikawa, J. Arvieux, B. Bassalleck, M.S. Chung, H. En'yo, T. Fukuda, H. Funahashi, S.V. Golovkin, A.M. Gorin, Y. Goto, M. Hanabata, T. Hayakawa, A. Ichikawa, M. Ieiri, K. Imai, M. Ishino, H. Kanda, Y.D. Kim, Y. Kondo, E.N. Kozarenko, I.E. Kreslo, J.M. Lee, A. Masaike, S. Mihara, K. Nakai, K. Nakazawa, K. Ozawa, A. Sato, H.D. Sato, K.S. Sim, T. Tabaru, F. Takeutchi, P. Tlustý, H. Torii, K. Yamamoto, S. Yokkaichi, and M. Yoshida. $\sigma^+ p$ elastic scattering cross sections in the region of $350 \leq p_{\Sigma+} \leq 750$ mev/c with a scintillating fiber active target. *Nuclear Physics A*, 761(1):41 – 66, 2005.

[16] G. Backenstoss, T. Bunaciu, S. Charalambus, J. Egger, H. Koch, A. Bamberger, U. Lynen, H.G. Ritter, and H. Schmitt. Observations of Σ hyperonic atoms. *Physics Letters B*, 33(3):230 – 232, 1970.

[17] G. Backenstoss, T. Bunaciu, J. Egger, H. Koch, A. Schwitter, and L. Tauscher. Intensity measurements on Σ-hyperonic and kaonic atoms. *Zeitschrift für Physik A Atoms and Nuclei*, 273(2):137–156, Jun 1975.

[18] R. J. Powers, M. Eckhause, P. P. Guss, A. D. Hancock, D. W. Hertzog, D. Joyce, J. R. Kane, W. C. Phillips, W. F. Vulcan, R. E. Welsh, R. J. Whyley, R. G. Winter, E. Austin, G. W. Dodson, J. P. Miller, F. O'Brien, B. L. Roberts, D. R. Tieger, R. B. Sutton, and R. Kunselman. Strong-interaction effect measurements in sigma hyperonic atoms of W and Pb. *Phys. Rev. C*, 47:1263–1273, Mar 1993.

[19] C.J. Batty, S.F. Biagi, M. Blecher, S.D. Hoath, R.A.J. Riddle, B.L. Roberts, J.D. Davies, G.J. Pyle, G.T.A. Squier, and D.M. Asbury. Measurement of strong inter-action effects in Σ atoms. *Physics Letters B*, 74(1):27 – 30, 1978.

[20] C.J. Batty, E. Friedman, and A. Gal. Strong interaction physics from hadronic atoms. *Physics Reports*, 287(5):385 – 445, 1997.

[21] R. Bertini, O. Bing, P. Birien, W. Brückner, H. Catz, A. Chaumeaux, J.M. Durand, M.A. Faessler, T.J. Ketel, K. Kilian, B. Mayer, J. Niewisch, B. Pietrzyk, B. Povh, H.G. Ritter, and M. Uhrmacher. Hypernuclei with sigma particles. *Physics Letters B*, 90(4):375 – 378, 1980.

[22] H. Piekarz, S. Bart, R. Hackenburg, A.D. Hancock, E.V. Hungerford, B. Mayes, K. Sekharan, J. Piekarz, M. Deutsch, R.E. Chrien, S. Chen, M. LeVine, D. Maurizio, M. May, H. Palevsky, Y. Xu, P.D. Barnes, B. Basslleck, R. Eisenstein, R. Grace, C. Maher, P. Pile, R. Rieder, W. Wharton, and R.L. Stearns. Experimental observation of the Σ hypernuclei, Σ6h and Σ16c. *Physics Letters B*, 110(6):428 – 432, 1982.

[23] R. Bertini, P. Birien, K. Braune, W. Brückner, G. Bruge, H. Catz, A. Chaumeaux, J. Ciborowski, H. Döbbeling, J.M. Durand, R.W. Frey, D. Garreta, S. Janouin, T.J. Ketel, K. Kilian, H. Kneis, S. Majewski, B. Mayer, J.C. Peng, B. Povh, R.D. Ransome, R. Szwed, T.-A. Shibata, A. Thiessen, M. Treichel, M. Uhrmacher, and Th. Walcher. Σ hypernuclear states in $(k^-, \pi^\pm)$ reactions on ^{1}2c. *Physics Letters B*, 136(1):29 – 32, 1984.

[24] R Bertini, P Birien, K Braune, W Brückner, G Bruge, H Catz, A Chaumeaux, J Ciborowski, H Döbbeling, J.M Durand, R.W Frey, D Garreta, S Janouin, T.J Ketel, K Kilian, H Kneis, S Majewski, B Mayer, J.C Peng, B Povh, R.D Ransome, R Szwed, T.-A Shibata, A Thiessen, M Treichel, M Uhrmacher, and Th Walcher. The (k^-, π^+) strangeness exchange reaction on ^{1}6o. *Physics Letters B*, 158(1):19 – 22, 1985.

[25] R.S. Hayano, T. Ishikawa, M. Iwasaki, H. Outa, E. Takada, H. Tamura, A. Sakaguchi, M. Aoki, and T. Yamazaki. Evidence for a bound state of the $^4_\Sigma$He hypernucleus. *Physics Letters B*, 231(4):355 – 358, 1989.

[26] M. May, R. E. Chrien, H. Palevsky, R. Sutter, S. Dytman, D. Marlow, P. Pile, F. Takeutchi, M. Deutsch, R. Cester, S. Bart, E. Hungerford, T. M. Williams, L. S. Pinsky, B. W. Mayes, and R. L. Stearns. Experimental study of the Σ-nucleon system through the reaction ^{2}H$(k, \pi)\Sigma n$. *Phys. Rev. C*, 25:1079–1081, Feb 1982.

[27] L. Tang, E. Hungerford, T. Kishimoto, B. Mayes, L. Pinsky, S. Bart, R. Chrien, P. Pile, R. Sutter, P. Barnes, G. Diebold, G. Franklin, D. Hertzog, B. Quinn, J. Seydoux, J. Szymanski, T. Fukda, and R. Stearns. Observations of hyperon-nucleus systems produced on ^{12}C and ^{7}Li targets using the (k^-, π^+) reaction at 715 Mev/c. *Phys. Rev. C*, 38:846–853, Aug 1988.

[28] Iwasaki. M. doctoral thesis. *Tokyo University*, 1987.

[29] Reyad Sawafta. Do narrow Σ hypernuclear states exist. *Nuclear Physics*, 585:103– 108, 1995.

[30] Haruhiko Outa, Toshimitsu Yamazaki, Masahiko Iwasaki, and Ryugo S. Hayano. Formation and decay of Σ hypernuclei in (stopped $K^-, \pi^\pm$) reactions. *Progress of Theoretical Physics Supplement*, 117:177–199, 1994.

[31] R.H. Dalitz, D.H. Davis, and A. Deloff. Is there a bound $^4_\Sigma$He? *Physics Letters B*, 236(1):76 – 80, 1990.

[32] T. Nagae, T. Miyachi, T. Fukuda, H. Outa, T. Tamagawa, J. Nakano, R. S. Hayano, H. Tamura, Y. Shimizu, K. Kubota, R. E. Chrien, R. Sutter, A. Rusek, W. J. Briscoe, R. Sawafta, E. V. Hungerford, A. Empl, W. Naing, C. Neerman, K. Johnston, and M. Planinic. Observation of a $^4_\Sigma$He bound state in the ^{4}He(K^-, π^-) reaction at 600 MeV/c. *Phys. Rev. Lett.*, 80:1605–1609, Feb 1998.

[33] O. Morimatsu and K. Yazaki. A study on the formation of σ-hypernuclei by $(\bar{K}, \pi)$ reaction. *Nuclear Physics A*, 483(3):493 – 513, 1988.

[34] H. Noumi, P. K. Saha, D. Abe, S. Ajimura, K. Aoki, H. C. Bhang, T. Endo, Y. Fujii, T. Fukuda, H. C. Guo, K. Imai, O. Hashimoto, H. Hotchi, E. H. Kim, J. H. Kim, T. Kishimoto, A. Krutenkova, K. Maeda, T. Nagae, M. Nakamura, H. Outa, M. Sekimoto, T. Saito, A. Sakaguchi, Y. Sato, R. Sawafta, Y. Shimizu, T. Takahashi, L. Tang, H. Tamura, K. Tanida, T. Watanabe, H. H. Xia, S. H. Zhou, L. H. Zhu, and X. F. Zhu. Sigma-nucleus potential in $A = 28$. *Phys. Rev. Lett.*, 89:072301, Jul 2002.

[35] P. K. Saha, H. Noumi, D. Abe, S. Ajimura, K. Aoki, H. C. Bhang, K. Dobashi, T. Endo, Y. Fujii, T. Fukuda, H. C. Guo, O. Hashimoto, H. Hotchi, K. Imai, E. H. Kim, J. H. Kim, T. Kishimoto, A. Krutenkova, K. Maeda, T. Nagae, M. Nakamura, H. Outa, T. Saito, A. Sakaguchi, Y. Sato, R. Sawafta, M. Sekimoto, Y. Shimizu, T. Takahashi, H. Tamura, L. Tang, K. Tanida, T. Watanabe, H. H. Xia, S. H. Zhou, X. F. Zhu, and L. H. Zhu. Σ-nucleus potential studied with the (π^-, K^+) reaction on medium-to-heavy nuclear targets. *Phys. Rev. C*, 70:044613, Oct 2004.

[36] Toru Harada and Yoshiharu Hirabayashi. Is the Σ–nucleus potential for Σ atoms consistent with the ^{28}Si(π^-, K^+) data? *Nuclear Physics A*, 759(1):143 – 169, 2005.

[37] Toru Harada. Hypernuclear production from K^- capture in liquid helium. *Nuclear Physics A*, 672(1):181 – 219, 2000.

[38] Toru Harada. Calculation of the $^4_\Sigma$He bound state in the ^{4}He (K^-, π^-) reaction at a MeV/c. *Phys. Rev. Lett.*, 81:5287–5290, Dec 1998.

[39] Toru Harada and Yoshiharu Hirabayashi. P-wave resonant state of the $^4_\Sigma$He hypernucleus in the ^{4}He(K^-, π^-) reaction. *Physics Letters B*, 740:312 – 316, 2015.

[40] T. Harada. private communication.

[41] Toshiyuki Takahashi, Satoshi Adachi, Michelangelo Agnello, Kanae Aoki, Osamu Araoka, Bernd Bassalleck, Elena Botta, Stefania Bufalino, Nobuyuki Chiga, Petr Evtoukhovitch, Alessandro Feliciello, Juergen Franz, Hiroyuki Fujioka, Shuhei Hayakawa, Erina Hirose, Ryotaro Honda, Kenji Hosomi, Yudai Ichikawa, Youichi Igarashi, Masahisa Iida, Masahiro Ikeno, Kenta Itahashi, Naoya Ishibashi, Shigeru Ishimoto, Ruri Iwasaki, Yutaka Kakiguchi, Katsuyu Kasami, Sunji Kim, Ryuta Kiuchi, Takeshi Koike, Yusuke Komatsu, Alexandr Kustov, David Mjavia, Yasuhiro Makida, Simonetta Marcello, Tomofumi Maruta, Shinichi Masumoto, Kenji Matsuoka, Koji Miwa, Anatolii Moiseenko, Manabu Moritsu, Tomofumi Nagae, Megumi Naruki, Hiroyuki Noumi, Hirokazu Ohhata, Takahiro Okamura, Ryosuke Ota, Masatoshi Saito, Atsushi Sakaguchi, Valentin Samoilov, Misako Sato, Yoshinori Sato, Michiko Sekimoto, Yoshihisa Shirakabe, Kotaro Shirotori, Hitoshi Sugimura, Shoji Suzuki, Yoshihiro Suzuki, Hitoshi Takahashi, Tomonori N. Takahashi, Hirokazu Tamura, Manobu Tanaka, Kazuya Tauchi, Toshiyuki Tanaka, Kiyoshi Tanida, Atsushi O. Tokiyasu, Kotaro Yoshida, Akihisa Toyoda, Zviadi Tsamalaidze, Tomohisa Uchida, Mifuyu Ukai, Hiroaki Watanabe, Takeshi O. Yamamoto, Yoshio Yonemoto, and Choong-Jae Yoon. Beam and SKS spectrometers at the K1.8 beam line. *Progress of Theoretical and Experimental Physics*, 2012(1):02B010, 2012.

[42] R. Honda, K. Miwa, I. Nakamura, M. Tanaka, K. Yoshimura, T. Uchida, and M. Ikeno. The development of the multi ppd readout electronics with easiroc and sitcp. *PoS PhotoDet2012*, 2012.

[43] Y. Igarashi, H. Fujii, T. Higuchi, M. Ikeno, E. Inoue, T. Murakami, Y. Nagasaka, M. Nakao, K. Nakayoshi, M. Saitoh, S. Shimazaki, S. Y. Suzuki, M. Tanaka, K. Tauchi, T. Uchida, and Y. Yasu. A common data acquisition system for high-intensity beam experiments. *IEEE Transactions on Nuclear Science*, 52(6):2866–2871, Dec 2005.

[44] Y. Igarashi, M. Ikeno, M. Saito, K. Nakayoshi, M. Tanaka, T. Takahashi, M. Moritsu, A. Okamura, K. Hosomi, T. Takahashi, and K. Itahashi. An Integrated Data Acquisition System for J-PARC Hadron Experiments. *IEEE Transactions on Nuclear Science*, 57(2):618–624, April 2010. `https://ieeexplore.ieee.org/document/5446539`.

[45] S. Morinobu. private communication.

[46] Jan Myrheim and Lars Bugge. A fast runge-kutta method for fitting tracks in a magnetic field. *Nuclear Instruments and Methods*, 160(1):43 – 48, 1979.

[47] ANASYS. `https://www.ansys.com/`.

[48] Ryotaro Honda. *Study of ΣN interaction in nuclei using meson beams*. PhD thesis, Tohoku University, 2014.

[49] M. Jurič, G. Bohm, J. Klabuhn, U. Krecker, F. Wysotzki, G. Coremans-Bertrand, J. Sacton, G. Wilquet, T. Cantwell, F. Esmael, A. Montwill, D.H. Davis,

D. Kiełczewska, T. Pniewski, T. Tymieniecka, and J. Zakrzewski. A new determination of the binding-energy values of the light hypernuclei (a < 15). *Nuclear Physics B*, 52(1):1 – 30, 1973.

[50] Daniel F. Kane. Partial-wave analysis of $K^-p \to \pi^\pm\Sigma^\mp$ between 1.73 and 2.11 GeV. *Phys. Rev. D*, 5:1583–1602, Apr 1972.

[51] S.M. Flattě. Coupled-channel analysis of the $\pi\eta$ and $k\bar{K}$ systems near $k\bar{K}$ threshold. *Physics Letters B*, 63(2):224 – 227, 1976.

[52] Ryugo S. Hayano. ^{4}He$(K^-, \pi^\pm)$ experiments at KEK and BNL. *Nuclear Physics A*, 547(1):151 – 156, 1992.

[53] R. Roosen, C. Vander Velde-Wilquet, J. H. Wickens, C. Comber, D. H. Davis, and D. N. Tovee. A study of the $\Lambda\pi^-pd$ final state produced in K^--meson interactions at rest in helium. *Il Nuovo Cimento A (1965-1970)*, 49(2):217–234, Jan 1979.

[54] Toru Harada and Yoshiharu Hirabayashi. ΣNN quasibound states in ^{3}He$(K^-, \pi^\mp)$ reactions at 600 mev/c. *Phys. Rev. C*, 89:054603, May 2014.

[55] Yazaki Koichi. Constituent quark model with strangeness. *Nuclear Physics A*, 479:217 – 226, 1988.